DEVELOPMENT OF A QUANTUM DOT MEDIATED THERMOMETRY FOR MINIMALLY INVASIVE THERMAL THERAPY

by

WILLARD L. HANSON

Presented to the Faculty of the Graduate School of
The University of Texas at Arlington in Partial Fulfillment
of the Requirements
for the Degree of

DOCTOR OF PHILOSOPHY

THE UNIVERSITY OF TEXAS AT ARLINGTON

August 2009

Dedicated to

My Wife

Elizabeth

ACKNOWLEDGEMENTS

I would like to thank my principal advisor, Dr. Bumsoo Han for his patient guidance and support throughout my graduate work. I would also like to thank Dr. Seiichi Nomura, Dr. Seung Mun You, Dr. Choong-Un Kim, and Dr. Digant Davé for their careful critique as part of my dissertation committee.

I acknowledge the support received from my colleagues within the Biotransport Phenomena Laboratory: Ming-Long Wang, Chuo-Li Wang, Jun-Kyu Jung, Jeffrey D. Miller, Najma Abdollahzadeh, Jihyun You, Eric Olson, Lacey Mlcak, Tenok DeHoyos, Ka Yaw Teo and Dr. S. W. Park.

I also graciously acknowledge the staff of Mechanical Engineering department: Tom Leeds, Michael Baker, Barbara Sanderson, Donna Woodhead, Janet Grober, Kermit Beird, Jay Dickey, Louella Carpenter, Debi Barton, Lanie Gordon, Kathy Priester and last, but certainly not least, Sally Thompson for their support, assistance, and patience throughout my graduate studies.

July 10, 2009

ABSTRACT

DEVELOPMENT OF A QUANTUM DOT MEDIATED THERMOMETRY FOR MINIMALLY INVASIVE THERMAL THERAPY

Willard Leo Hanson, PhD.

The University of Texas at Arlington, 2009

Supervising Professor: Bumsoo Han

Thermally-related, minimally invasive therapies are designed to treat tumors while minimizing damage to the surrounding tissues. Adjacent tissues become susceptible to thermal injury to ensure the cancer is completely destroyed. Destroying tumor cells, while minimizing collateral damage to the surrounding tissue, requires the capacity to control and monitor tissue temperatures both spatially and temporally. Current devices measure the tumor’s tissue temperature at a specific location leaving the majority unmonitored. A point-wise application can not substantiate complete tumor destruction. This type of surgery would be more effective if volumetric tissue temperature measurement were available.

On this premise, the feasibility of a quantum dot (QD) assembly to measure the tissue temperature volumetrically was tested in the experiments described in this dissertation. QDs are fluorescence semiconductor nanoparticles having various superior optical properties. This new QD-mediated thermometry is capable of monitoring the thermal features of tissues non-invasively by measuring the aggregate fluorescence intensity of the QDs accumulated at the target tissues prior to and during the surgical procedure. Thus, such a modality would allow evaluation of tissue destruction by measuring the fluorescence intensity of the QD as a function of temperature. The present study also quantified the photoluminescence intensity and attenuation of the QD as a function of depth and wavelength using a tissue phantom. A prototype system was developed to measure the illumination through a tissue phantom as a proof of concept of the feasibility of a noninvasive thermal therapy. This prototype includes experimental hardware, software and working methods to perform image acquisition, and data reduction strategic to quantify the intensity and transport characteristics of the QD.

The significance of this work is that real-time volumetric temperature information will prove a more robust tool for use in thermal surgery. The thermal ablation zone is extremely diffusive and current imaging techniques and/or equipment may not accurately monitor portions of the tumor surviving the ablation process. Used in conjunction with other volumetric measuring systems, i.e., fluorescence or bioluminescence tomography, this platform will have the capacity to produce direct three dimensional intraoperative monitoring of the thermal surgical procedure. Lastely,

realization of system requirements will aid in the automation of imaging to ease data acquisition, maximize exposure, and control test bed temperature.

TABLE OF CONTENTS

Appendix

LIST OF ILLUSTRATIONS

Figure Page

NOMENCLATURE

Latin Symbols

a	coefficient, y-intercept
b	coefficient, slope
c	specific heat, Speed of light
f	frequency
g	anisotropy factor
h	Plank constant
i	intensity
j	$\sqrt{-1}$
l_i	directional cosines, $i = 1, 2, 3$
n	index of refraction, normal vector
p	particle momentum, scattering phase function
$\bar{r}$	position vector
$\hat{s}$	direction vector
t	time
x, y, z	coordinate positions, independent variables

A	pre-exponential factor, coefficient
BRV	black reference value
C	concentration, absorption
D	diffusivity
E	energy
E_a	activation energy
I	intensity
J	energy flux density
K	diffusion
N	shape function
P	instantaneous power
P_{avg}	average power
P_{pk}	peak power
P_1	Legendre polynomial
Q	heat generation
R	residual, universal gas constant, constant
S	directional coordinate
T	temperature, thickness
T_{a}	ambient temperature
T_{ref}	reference temperature
T_{crit}	critical temperature

W_i	weighting function
WRV	white reference value
Y_l^m	normalized spherical harmonic
Z	measured intensity

Greek Symbols

β	load vector
γ	azimuthal angle
δ	azimuthal angle
ε	error
θ	polar angle
κ	optical coordinate
λ	wavelength
μ	coefficient
μ_a	absorption coefficient
μ_{eff}	effective attenuation coefficient
μ_s	scattering coefficient
μ_t	total attenuation coefficient
μ'_s	reduced scattering coefficient
μ'_t	reduced attenuation coefficient
μ_{tr}	transport attenuation coefficient
ρ	density

τ	optical depth, pulse repetition rate
τ'	reduced optical depth
φ	azimuthal angle, dependent variable
ω	solid angle, blood perfusion
Θ	angle
Γ	boundary
Φ	photon density
Ψ	shape function
Ω	solid angle, damage integral, albedo, surface

Subscripts and Superscripts

a	activation, absorption, ambient
bl	blood perfusion
crit	critical
eff	effective
i	coordinate indices
l	degree indices
m	medium, order indices
ref	reference
s	scattering
t	transducer material, total
A	artery

O	initial
τ	elapsed time
‘	reduced, dummy variable
*	complex conjugate

CHAPTER 1

INTRODUCTION

It is estimated that over 200,000 men were diagnosed with prostate cancer in 2007, with an estimated 10% of cases resulting in death [1]. Patient survival is generally in direct proportion to the extent of the tumor development. During the earlier stages of a cancer the cells are relatively contained. After further development the tumor spreads to adjacent tissues, (metastasizes) after which it is generally not curable. Current technology enables detection of over 90% of all early stage prostate cancers ensuring a nearly 100% survival rate [2].

Traditional cancer treatment requires tumor removal often with post-surgical radiation treatment. Because of the associated complications with the surgery this conventional treatment is typically reserved for more healthy patients.

Ablative therapy is an alternative, minimally-invasive treatment to destroy cancerous tissue with minimal impact and associated complications. Nevertheless, the limiting factor in ablative therapy is the ability to monitor and thus control the energy deposition to prevent collateral tissue damage.

The present dissertation focuses on the development of a new noninvasive modality to monitor tissue temperature volumetrically during therapeutic procedures. Such procedure would 1) enable greater control over the resulting temperature profile,

2) allow more accurately placed temperature gradients, and 3) result in optimized energy deposition within the tumor. Various biomedical imaging techniques offer greater detail and thus are capable of providing quantitative information on disease diagnostics. However, these methods are not conducive to the thermal surgical arena. The development of a temperature field image overlaid onto the diagnostic imaging data would increase the potential to facilitate control over a surgical heat transfer application by providing real-time monitoring through volumetric temperature feedback during treatment. The goal of the experiments in this work was to develop the methodology for intraoperative monitoring of the lesion during thermal therapy using the temperature-dependent fluorescence intensity of a QD. Towards this end, the characterization of the tissue-light interaction of a QD mediated thermometry for in vivo application will be addressed. This includes 1) development of a prototype thermometry system to monitor the temperature change relevant to thermal therapies, 2) establishment of the temperature dependence of the QD fluorescence intensity; 3) testing of new nanocomposite particles, QD-embedded nanoparticles, 4) demonstration of the feasibility of QD fluorescence thermometry during a gold nanoshell-mediated thermal application, and 5) characterizing the interaction of QD fluorescence with tissue both experimentally and theoretically. More broadly, this research will facilitate future engineering research toward the development of a clinical tool facilitating real-time, high-resolution imaging feedback of bioheat transfer to be used for surgical applications.

CHAPTER 2

BACKGROUND

2.1 Thermal Injury

The safe application of thermal energy to destroy tumor cells, while minimizing damage to the surrounding healthy tissue, requires the ability to deliver heat with large temperature gradients. Hyperthermia is a surgical technique in which tissue temperature is increased from a normal temperature of 37°C to 43-46°C. Thermal injury usually begins near 42°C and the application of heat to tumors, even at temperatures as low as 45°C, can be cytotoxic if applied over a sufficient period of time. Heating tissues to these temperatures causes necrosis, i.e., molecular changes in tissue by bond destruction and membrane alteration that result in cell death. Hyperthermia requires several minutes to evolve and its damage can be forecasted via the Arrhenius equation, (1). A consequence of hyperthermia is the activation of cellular thermotolerance after an initial exposure to higher temperatures.

$$\Omega(\tau) = \ln[C(0)/C(\tau)] = A\int_0^{\tau} \exp[-E_a/(RT(t))]dt \tag{1}$$

For temperatures slightly above 46-50°C, held for extended periods of time, the cells suffer irreversible damage in less than sixty minutes, while hold temperatures greater than 50°C cell death occurs more quickly. Operating on tissues at temperatures greater than 50°C requires much less time. Thermal therapy is the exposure of tissue to temperatures of 50-52°C and is cytotoxic within 4-6 minutes [3]. Thermal therapy destroys tumor cells through the application of heat, to cause coagulation, using radio frequency, microwave, laser, or ultrasound energy. For temperatures less than boiling the main mechanism for the denaturation of macromolecules is by breaking the van der Waal's bonds which causes a permanent alteration of cellular and vascular tissue [3-6]. At temperatures greater than 50°C there are more severe consequences. The destruction of enzymatic activity, reduction in energy transport, increased cellular immobility, and disabling of cellular repair mechanisms.

Hydrogen bonding assembles atoms into secondary structures creating alpha helices and beta sheets. The outermost levels are responsible for arranging the protein for a particular function. Molecules organize or self-assemble through the formation of hydrogen, ionic, and van derWaals bonds or by non-covalent hydrophobic interactions. The cell itself is housed in an amphiphilic bilayer membrane, mainly composed of phospholipids, positioned with their polar groups facing outwards, toward the surrounding medium, and their lipophilic chains facing each other, on the inside of the bilayer. Generally a polymer can have hydrophobic and hydrophilic regions, possess a charge-carrying capacity and have the ability to self-assemble into a hydrogel [7].

Biological soft tissue behaves much like an elastomeric material. It can have nonlinear elastic behavior with cycling hysteresis, creep, stress relaxation, and can shrink upon heating mainly because of the long-chained polymeric microstructures that contribute entropic behavior [7]. Below 85-90°C, components inside the cell like DNA and RNA will not incur any substantial damage to their functionality or spatial arrangement [4]. From 10-40°C lipid membranes incur a phase transition but the temperature needs to be much higher for it to act as a mechanism for hyperthermic cell destruction [3].

The temperature of the human body is approximately 37°C and the ability of cells to remain in thermal equilibrium can be occur up to a temperature of approximately 40°C [8]. There seems to be minimal measurable effect of any thermal application below 42°C [9]. Thermal denaturation destroys the protein structure within the cell by making it biologically inactive around 42-65°C [3, 4]. Cells become more easily damaged however when exposed to chemotherapy and radiation treatments with accompanied temperatures in the initial hyperthermic region, around 45°C [8]. The temperature effect varies with tissue type, and exposure to these temperatures alone, even for extended periods of time, does not mean that all cells will be destroyed [8]. Above 60°C, protein and collagen denaturization leads to the irreversible coagulation of tissue [8]. Application of thermal therapy in this temperature range does not require assistance by radiation or chemotherapeutic adjuvants.

Exposure of adjacent healthy tissue to these temperatures for an extended period of time increases the risk of unnecessary cell damage and thus requires some modification of the application to improve the thermal ablation to better regulating coagulation. Any volumetric heating effect would naturally require a corresponding increase in energy. There are some limitations to these temperature insults, i.e., not being able to uniformly heat a large or irregular tissue volume or in the situation of adjacent tissues with markedly different heat capacities [8]. According to Kang, saline or iron compounds could be implemented to augment the process. Saline may also be used during ablative therapy as a continuous stream of fluid transporting heat from the affected volume. Controlling the blood flow to the affected area can also reduce collateral heating thus improve ablation [8].

Thermally-mediated events destroy malignant tumors by killing cells and shrinking collagen to influence tissue stability and by modifying protein kinetics. Proteins are composed of amino acids crucial for tissue function. They have a bond strength hierarchy that provides molecular structure - the strongest being the covalent bond [5]. Proteins are bound to lipids and carbohydrates, and any thermal application should recognize how these compounds might affect protein bonding.

Protein in the form of collagen is the primary structural component in the body and excessive heat can alter its structure [7]. As a matter of practice, proteins have the most effect on cell destruction in hyperthermic therapy by changing the mechanical behavior of collagen [3, 7]. Altered viscoelastic behaviors during and following the heating of protein is independent of any previous thermal insult when the temperature range is within the physiological range. When the temperature is increased to the supra-physiological range however, the viscoelastic behavior becomes irreversible [7].

Kinetics may also be used in the denaturation process through mechanical and/or chemical means [5]. Hyperthermia exposes tissue to temperatures less than 60°C where the cell viability is determined by protein denaturation as modeled by the thermal damage function, Ω. This is a first-order irreversible rate process used to model tissue kinetics mathematically [10]. The Arrhenius relationship is used to predict cellular viability from the effects of hyperthermic temperature. The activation energy (E_a) and molecular collision frequency factor (A) are used to quantify tissue damage by duration and temperature profile Eq. 1 [3, 11, 12]. For temperatures less than a critical temperature T_{crit}, there will be no substantive tissue damage [9].

Henriques (1947) used rate coefficients such that complete necrosis of the skin was associated with a solution of Ω = 1. Equation. (2) which is derived from (1), when set equal to one can then determine the critical temperature, T_{crit} of the tissue. For example, using the injury criteria for skin tissue, E_a, 81.33 [kJ/mol], and the A, 6.28e5[1/s], and R the universal gas constant, 8.3143 [kJ/mol], yields a critical temperature of 59.7°C for skin tissue [10] [9].

$$\frac{d\Omega(\tau)}{dt} \equiv A\exp\left[\frac{-E_a}{(RT_{crit})}\right] = 1 \qquad \text{thus} \qquad T_{crit} = \frac{E_a}{(R\ln(A))} \tag{2}$$

Heat denaturation occurs when changes in protein structure are such that the protein can no longer carry out its specific function. This denaturation can be partial, total, reversible or irreversible. It is considered irreversible when the hydrogen bonding of the protein is rearranged to a less-ordered state. The total amount of heat absorbed or released is defined as the enthalpic heat change measured when a phase transition takes place. This can result in an exothermic process that may cause coagulation, aggregation, and/or gelation of the denatured proteins [5]. Experimental data are fitted to the Arrhenius chart to determine the unknown parameters E_a and A. The damage accumulation rate, Eq. 2, relates the critical temperature, T_{crit} to damage accumulation [12].

Latent heat and heat capacity are values used to model the thermal effects in the blood perfusion response during vascular injury [3]. The heat transfer equation used for modeling blood perfused tissue is the Pennes “bioheat” equation. Here the heat transfer is proportional to the volumetric flow temperature difference between arterial blood and local tissue temperatures. It is assumed the heat transport is in regions where the blood vessels are less than one half mm in diameter, (3) [3].

$$Q_{bl} = \omega \rho_{bl} c_{bl} \left(T_a - T \right) \tag{3}$$

There are several essential factors that influence the thermal sensitivity of tissue. They are thermotolerance, pH, pressure and a phenomenon referred to as ‘step down’ heating. The effect of these factors on the thermal sensitivity can be determined using Arrhenius analysis [13].

Thermotolerance, occurs when tissues or cells acquire resistance to thermal cytotoxicity as a transient response after exposure to thermal stress [13]. Biological specimens respond to thermal heat shock in response to denaturation and thermotolerance [3]. Heat shock is the effect of subjecting a cell to a temperature higher than the ideal body temperature of the organism, where 60°C is considered the transition to denaturation [3]. Thermotolerance allows the protein to protect intracellular components during mild thermal insults. The cell can actually heal itself from any excess heat energy through the activation of heat shock proteins [3]. At 80°C, the membrane's mechanical permeability is greatly increased [12]. Above 105°C, thermotropic injury is induced and the tissue experiences mechanical events such as boiling, vaporization, or even carbonization [3, 8]. This suggests that a controllable scheme for ablative therapy would be to apply energy and maintain it within the 50-100°C range [8].

As a transient phenomenon, thermotolerance is a measure of the added cellular resistance to thermal cytotoxicity. The amount of added defense depends on the amount of initial damage and the time elapsed since the initial application. For example, initial thermal treatment of mouse ear skin found the maximum amount of thermotolerance was achieved when it took twice the amount of time to achieve half the necrosis [13]. This elapse time was also dependent on the original exposure. The effect of thermotolerance, as shown by Arrhenius analysis, indicates that the magnitude of the plot shifts to the right as much as 2°C, but that the slope of the curve was not influenced [13].

Thermotolerance has applications for all types of tissue, and also influences vascular reaction to thermal injury. During mild thermal injury, the natural response of biological tissue is to increase the perfusion rate. Conversely, when tissues have experienced previous heat insults the perfusion rate is diminished [13]. The effect of thermotolerance in humans is unknown, however, animal findings show a full burn would occur after nine minutes of continuous heating at 49°C [13]. Yet, if the same energy was segmented and spread over an hour, there was less damage, eventually resulting in only a mild erythema [13, 14]. This is consistent with stimulation by thermotolerance [13]. With a reduction in blood supply, reduced perfusion is sensed and this causes a decrease in the thermoregulatory capacity of the tissue resulting in increasing its thermal sensitivity [13].

Tissue heating rate can also dramatically affect the extent of cytotoxicity. Tissue cultures in a water bath can reach their target temperature within two minutes and clinical treatment of tumors may reach target temperatures within twenty minutes [13]. However, if the same target temperature is achieved over an extended heating period there will be a proportional increase in viability. Thus thermotolerance develops to a greater degree during slow heating rates. The degree of cytotoxicity that occurs from differences between the resting and final temperature depends on the final resting temperature [13].

Other factors may also affect protein stability including pH, a factor which when increased, enhances the heat effect of protein denaturation. Substances, such as methanol, ethanol or butanol, can also be introduced to cause proteins to be more sensitive to hyperthermic activity. Glycerol, deuterium, even other proteins can retard or delay protein denaturation in cells [5].

At 100°C, water within the tissue begins to vaporize and by carrying away large amounts of latent heat from the surrounding tissue. Also, gas bubbles can be generated which can cause mechanical rupture. After the cells have been completely dehydrated carbonization takes place because there is no phase change mechanism left to remove the heat. Finally at about 300°C melting will occur [10].

As mentioned earlier, heat shock proteins (HSP) are a special class of cellular proteins designed to regulate thermotolerance. They are part of the body's natural defense against injury caused by high temperatures. These proteins are responsible for delaying the denaturation of other proteins [5, 13, 15]. HSP are activated during less than lethal heating [5], and it is believed that they can only be activated through application of heat, meaning they may not protect the cell during freezing-induced protein denaturation [5].

The production of most cellular proteins is down-regulated during and after an application of heat stress [13]. HSP however are up-regulated and may participate in the degradation or refolding of other proteins [13, 15]. The presence of HSP directly reflects the degree of initial thermal damage to the cell and the time that has lapsed since the initial injury. When HSP become expressed they reduce the effectiveness of thermal therapy by enhancing tumor cell resistance, thus increasing the cell viability [15]. This occurs in regions where insufficient thermal energy is available to adequately destroy any protein by coagulation. HSP activation also inhibits future chemotherapy or radiation treatment.

During hyperthermic treatment, 42-44°C, HSP molecules can be induced to express themselves [15]. This also enhances cell viability increasing tumor resistance to later treatments. Thus the presence of HSP can both impede thermal treatments of tumors as described above and aid in the protection of healthy tissue. HSP activation may cause the surrounding healthy tissue to survive an otherwise lethal dose of heat, if applied properly. In effect, this allows the increase thermal resistance of the healthy cells to improve the efficacy of target cells. At higher temperatures, around 55°C, the application of ablative thermal treatments can destroy the entire organ [15]. Thermal injury strong enough to cause destruction of the tumor requires denaturation to completely eliminate the functionality of HSP. Healthy tissue can be groomed to survive ablation thus decreasing the unwanted destruction of tissue adjacent to the tumor. HSP can also repair thermally-injured proteins and initiate the production of new proteins [15].

Examples of HSP are the molecule HSP27, a 27 kilodalton molecule, responsible for modulating oxygen, and HSP70, a protein that aids in cell reproduction. HSP27 and HSP70 expression kinetics and injury data from normal and cancerous prostate tumors follow the Arrhenius damage model. The results show a strong correlation confirming the predicted temperature-induced expression of HSP27 and HSP70 [15].

In addition to HSP, two other aspects that influence the extent of thermal injury are pressure points and a phenomenon referred to as step-down heating. Pressure points have been found to cause premature burning with respect to the clinical application of RF thermal therapy. This is owing to reduced perfusion and is found to occur at temperatures lower than what might be predicted by modeling [13]. In clinical applications of hyperthermia, burn injuries have been reported where the skin temperature had not exceeded 43°C, but at sites near pressure points, developed during whole body hyperthermia using water blankets [13].

Step-down heating occurs when the temperature drops across a breakpoint temperature. This breakpoint condition is based upon the amount of heat stress required to initiate thermotolerance at a given temperature [13]. Once thermotolerance has been initiated it will continue to affect the tissue even if the temperature drops back down below the activation temperature [13]. This result has no affect on the slope of the Arrhenius plot but only shifts its magnitude. The skewed results indicate that the actual thermal damage will be less than what is predicted by Arrhenius analysis [13].

Generally all actions of the freeze-thaw cycle are capable of causing tissue injury [16]. As a rule of thumb, staying at the coldest temperature for a prolonged period of time is the primary cause of cell death and for this technique to be efficient, attempts should be made to reach -50°C [16]. The cooling rate is not the most critical factor but should be as fast as possible. On the other hand, a slow thawing rate is considered a major destructive factor [16]. Cycling through the freeze-thaw phase region improves efficacy [16]. At the periphery of the cryosurgical lesion the cells do not reach a temperature low enough to cause sufficient intracellular freezing [16]. However, even though there is not enough stress in this region to destroy the cells immediately, they die by apoptosis, even days after cryosurgery [17].

Glycerol, along with other adjuvents, can be used as a cryoprotectant against freezing injury caused by dehydration. Glycerol is commonly used in many manufacturing processes to maintain hydration because the molecule naturally binds water with a high affinity. Hydration may of proteins protect them through cryoprotectant interactions. Drying increases cross linking and cell damage [5]. Protectants such as ethylene glycol and even mechanical loading can be used during heat denaturation to stabilize collagenous tissues by delaying the denaturation events when higher temperatures have been reached. Chemical additives that change pH help protect protein denaturation by changing the activation energy, activation enthalpy, on frequency factor activation entropy, and reduce the mechanical stress of the protein [5].

Gene-regulated cell death by apoptosis is evident to temperatures as low as -75°C [16, 18]. Evidence exists to support molecular mechanisms that can also contribute to cell survivability. However exposure to low temperature alone is not enough to assume cell destruction [16]. The results can still be well predicted however, but they are strong nonlinear functions of temperature and time, $t_{T_{ref}} = \int_{t=0}^{t=final} R^{\left(T_{ref} - T(t)\right)} dt$ where T_{ref} is the reference temperature, R is empirically defined as 0.5 for $T(t) \geq 43°C$ and 0.25 for $T(t) \leq 43°C$ [19].

2.2 Current Thermal Therapies

2.2.1 High Intensity Focused Ultrasound

2.2.1.1 Theory

An early twentieth century technology, ultrasound employs the characteristic of certain crystalline materials to develop an electric charge. Piezoelectricity is the ability of certain crystals to generate a voltage proportional to applied mechanical stress. The converse is also true; a geometric strain or deformation of certain materials will generate a proportional voltage output. Thus, a pulsed or sinusoidal excitation of a ceramic element can generate sound waves and the primary frequency of resonance is determined by the thickness of the transducer [19]. In general, if the material transducer speed of sound equals c_t, and the resonance frequency equals f_o, then the thickness of the transducer material should be $T_t = \lambda_t/2$ where $\lambda_t = c_t/f_o$ [19].

2.2.1.2 Application

High-intensity focused ultrasound (HIFU) uses mechanical (acoustic) energy as an ablation tool for non-invasive, or minimally-invasive thermal therapy. HIFU can selectively localize and destroy a tumor volume by inducing coagulative necrosis without damaging the intervening and surrounding tissue [20-23]. It does this by using sharply focused mechanical energy accurately placed within a well defined focal volume to cause tissue destruction [22]. The propagating longitudinal pressure waves are mechanical vibrations from sound waves that are converted to heat when absorbed by tissue. This sound wave energy is converted into heat with enough strength to destroy the tissue [20]. HIFU functions hyperthermically to elevate tissue temperature to destroy deceased tissue by necrosis [6, 19, 20, 23-25].

HIFU is similar to its electromagnetic counterpart in that it can be tuned to deliver an output proportional to its aperture geometry, output frequency, and penetration depth [19]. However, compared to heating profiles of other thermal therapies, ultrasound has deeper tissue penetration because of lower attenuation rate [6].

Studies have shown that interstitial ultrasound delivers irradiation-free coagulative necrosis e.g., the localized treatment of prostate therapy [6, 19, 21, 22].

Most HIFU therapies operate in the frequency range of 0.5 to 5.0 MHz [19]. The amount of coagulation depends on many factors; exposure time, applied power, type and density variation of tissue, perfusion rate, presence of major blood vessels, and is difficult to estimate [19, 24]. More energy is required to produce a thermal lesion the deeper into the tissue beam is focused into the tissue. This is accomplished either by increasing the exposure time or ultrasonic intensity. Ultimately, the absorbed energy determines the lesion volume. The lesions form around the focal plane and are biased to the front of it due to the non-linearity of the ultrasound. This is caused by the high frequency components of the beam traveling ahead of the focus [22].

Unlike other forms of focused energy, HIFU does not have cumulative effects and can thus be used in conjunction with other cancer treatment modalities, e.g., radiation therapy for deep localized hyperthermia [23]. HIFU is a repeatable treatment and even allows other treatments after HIFU surgery [20]. Joint application can be applied through hyperthermic heating of tissue to 42 to 46°C for periods extending up to several hours, or by thermal coagulation, where the tissue is heated for several seconds only, but to temperatures from 60 to 100°C where both thermal and mechanical energy combine to cause cavitation of the tissue [19]. One disadvantage of HIFU is that as a localized treatment, a volume limit can be reached, the upper limit of the tissue volume approximately 50 mL [20]. For larger tumors, longer depths probes are required.

A larger blood perfusion rate will result in a smaller thermal lesion size during HIFU [24]. For a focal zone larger than 20mm in diameter, the threshold value of thermal dose heating temperature is only affected by the blood perfusion rate [24]. Blood perfusion rate also greatly affects the thermal dose distribution and the contour of T300 [24]. T300 is a benchmark, defined as the maximum temperature corresponding to a thermal dose after 300 minutes. The thermal lesion is directly proportional to sonication time and heating power. In essence, a higher blood perfusion rate acts as a strong heat sink, taking energy away more quickly, requiring higher temperatures to achieve the thermal dose threshold.

To determine the dimensions of the thermal lesion two target points on the heating volume's boundary are set. One boundary is ahead, and the other behind, the targeted tissue centerline to create a heating pattern that can deliver the same absorbed power density level onto these two target points until T300 [24]. When the target volume is larger than 20mm the thermal conduction effect becomes negligible. T300 is defined on the central z axis and is independent of the system parameters and the heating strategies.

Ultrasonic lesions formed in vitro are structures that reflect high-frequency sound waves. They are formed immediately and can thus show the progress of tissue damage simultaneously and with a clearly-defined edge of necrosis [22]. Diagnostic ultrasound, used in conjunction with HIFU, can show the volume of damaged tissue from HIFU as a highly echogenic region. Damaged tissue is a source of scatter because the lesion becomes acoustically different from its surroundings. By altering focal depth within tissue it has been shown that the lesion is formed largely in front of the focal plane [22]. When using HIFU a spectrum of echo changes occur - from no changes, to what is called hyperechogenicity, most probably caused by intracellular water content [21]. The increased water content enables micro-cavitation during HIFU, thus changing the echo pattern without altering the size, location, or quality of necrosis. The final lesion volume depends on the energy and thus a focal lesion is formed primarily in front of the focal plane due to the nonlinear distortion of the sound waves towards the higher frequencies [21]. The duration of HIFU treatment is dependant only on the volume of the HIFU lesion. A treatment time of 4 hours has yielded a 40ml prostate necrosis [21]. A more versatile application of HIFU uses a phased array of transducers. This arrangement offers added capabilities such as high-speed electronic scanning, aberration correction, and relative motion compensation [23].

2.2.2 LASER

2.2.2.1 Theory

The optical properties of tissue are a function of wavelength. Thermal denaturation is a rate process where injury and inflammation of tissue occurs after a temperature increase of 10°C [4]. Further temperature increases cause coagulation necrosis [4]. Optical scattering caused by coagulation requires real-time monitoring to compensate for the variability caused by charring and other tissue optical property changes. The induced plasma breakdown of biological material may occur with the application of picosecond length pulses. This technique can even produce acoustic events if the pulsewidth is synchronized to a chromaphore's thermal diffusion time [4]. Temperatures greater than 100°C, initiates boiling and vaporization of tissue begins generating steam and a dramatic increase in volume expansion [4]. Further increases in temperature vaporize water content and result in carbonization. Laser-induced heating may change macromolecule membranes, viscosity, and tissue optical and thermal properties [4]. Short pulse irradiation can result in a rapid temperature rise and mechanical damage that may alter membrane function both physically and biologically [4]. The photophysical effects of laser use may lead to changes in physical and chemical properties of molecules, blood flow and permeability of injured cells. The laser greatly increases the spatial control of the extent of tissue injury due to the concentration of light, a small focal volume of tissue may be selected [4].

Skin is the initial boundary against electromagnetic radiation. How light is redistributed throughout tissue during laser irradiation is dependent on its optical properties [26]. Only 4-8 % of the laser light is directly reflected from the surface. The remaining reflectance is due to light being reemitted from within the tissue [27, 28]. Light reflected from the skin includes a regular portion reflected at the angle of incidence and a diffuse portion. Light entering the tissue is then either absorbed or scattered. The light may also be transmitted out of the tissue depending upon the optical density [29]. Most radiation in the UV does not pass through the skin because of interaction with biomolecules and cutaneous blood vessels [4]. The laser's scattering coefficient decreases with increasing wavelength implying that longer wavelengths penetrate deeper into tissue.

Photon energies less than the strengths of molecular bonds allow heating by absorption. Photon energy absorbed in the NIR region affect the vibrational and rotational bands in molecule, and therefore acts to thermalize the absorbed energy. The energy in this spectrum is less than four electron-volts. Any higher energy would result in an electronic transition causing some of the absorbed energy to be reradiated [4]. For example, at a wavelength of 800 nm there would be an energy increase of 1.55eV (2.48e-19 J).

Light must scatter multiple times before it can be considered isotropic, thus it is not appropriate to employ a general model to cover thin sections. The distribution of light can be modeled as steady state if the duration of the pulse is long enough and can be considered to have constant optical properties if the tissue is homogeneous and does not bleach or char. The anisotropy of the skin allows light to be scattered within the tissue with some directional dependence, i.e., either forwardly or backwardly scattered. Anisotropy increases with wavelength indicating that light scattering increases in the forward direction [26]. Scattered light through tissue depends upon internal tissue reflecting and absorbing. Light reflected from the surface of the tissue should include direct surface reflectance and the back scattered light [30].

The radiative transport theorem requires analysis of tissue optical properties to measure the scattering of light in random media. This basic theory called the “Equation of Transfer,” is equivalent to Boltzmann’s kinetic theory of gases [29] [31]. Illumination power, focal diameter and irradiation time, based on mathematical and empirical data, have several general operational parameters. The optical properties of the tissue are determined first, then the light distribution in the tissue is resolved. This is done by carefully setting the boundary conditions and scattering functions characteristic of those tissues.

For highly scattering media the diffusion approximation (DA) of the radiative transfer equation (RTE) may be used to adequately describe light distribution in tissue. Light is strongly forward scattering near the epidermis requiring several scattering events to be considered uniform. Beyond this distance, approximately one millimeter, it is considered isotropic [29]. To illustrate, a thin, 2 mm, tissue was irradiated in vitro. The back surface showed an area four times larger than the incident beam spot size while the backscattered area on the front surface had an area twice that of the incident beam [30].

Analysis of the reflected signal from the skin can give information about tissue, and blood concentration, even about drug content [4]. The skin is normally rough and acts to diffuse incident radiation. The epidermis contains a melaninless epidermal layer composed of keratinocytes that produce a fibrous protective protein that loses its nucleus, becomes flattened as it is dehydrated and is pushed toward the surface to become a densely-packed layer of keratin and lipids. Basal cells called melanocytes, also in the epidermis, contain a protein that absorbs visible and ultraviolet light that protects the skin against damage by producing melanin [4, 11]. Across the spectrum, melanin is the most important chromophore, absorbing less toward longer wavelengths. Without melanin only a small percentage of the 320 nm light will reach the blood vessels in the dermis [4]. Blood absorbs strongly in the blue and green and thus light affected by blood remitted has these colors removed from the spectrum. Sunburn or predisposition to certain skin cancers is inversely related to melanin content in the skin and tanning increases the production of melanin [4]. The dermis is a mixture of fibers, collagen, reticulum, and elastin, which gives the skin a high tensile strength while still allowing pliability. Collagen is a long molecule woven into fibrils which is made in cells called fibroblasts. Fibroblasts are responsible for producing the proteins and viscous materials of the dermis. The depth of light penetration in connective tissue is largely due to the scattering by collagen fibers [4].

Thermal destruction of tissue by lasers occurs by heat deposition and depends on tissue absorption and on the thermal tissue properties that usually vary with temperature and water content [29]. Only the absorbed light can heat tissue radiatively. For a nonscattering medium the heat deposition is given by $Q(r, z) = u_a I(z)$, where $I(z)$ is modeled from Beer's Law [29]. The absorption coefficient may be replaced by the attenuation coefficient because any decrease in available light is due to scattering as well as absorption. The primary absorbing materials in tissue are melanin and hemoglobin [29, 30].

A laser's insults on tissue are highly selective - constraining thermal effects to targets smaller than organelles [4]. Laser photomedicine is used for diagnosis and surgery employing nonionizing electromagnetic radiation. This includes the use of pulsed radiation to confine the heating effects on selective target biomolecules and chromophores [4]. NIR light is less absorbed by the epidermal melanin and is thus able to penetrate deeper into the dermis than visible light. This allows laser irradiation in the

NIR to improve the quality of thermal therapy [11]. The Arrhenius relationship damage integral was used to quantify the tissue damage of human skin to near-infrared and visible laser irradiation [11].

This implies that a 940 nm light is more effective than a shorter 580 nm light for the treatment of tissue with large-sized blood vessels and moderately to heavily pigmented skin. The contrary was true for optimal efficacy when treating small-sized blood vessels. It has been also shown that tissue blood content affects the threshold dosage for tissue damage even more than blood vessel diameter.

A pulsed application results in higher peak temperature of the skin tissue compared to a continuous wave profile [11]. Common wavelengths for the treatment of cutaneous skin tissue are between 585 and 595 nm using pulsed dye lasers. Some patients require multiple treatments and even others do not respond because of either limited light penetration depth due to large diameter blood vessels or due to high melanin concentration in skin that competes with subsurface-targeted blood vessels in the absorption of laser light [11].

2.2.2.2 Application

NIR Laser

The choice of irradiation wavelength can change the depth of penetration of the light [4]. Near-infrared (NIR) wavelengths penetrate deeper into skin and blood than visible wavelengths because of reduced absorption [11]. Thus, improved therapies using near-infrared wavelengths may help those applications requiring deeper tissue penetration since the blood absorption coefficients of near-infrared wavelengths are lower than those of visible wavelengths [11].

Longer laser pulse durations, actually composed of a chain of micro pulses, are used for treating the large-sized blood vessels because they match the thermal relaxation time of the blood vessels more effectively [11]. As long as the interval between the pulses is less than the thermal relaxation time of the blood vessel the light profile will still approximate a long single pulse. This allows the heat to be confined to the blood vessel diameter [11].

Near-infrared (NIR) lasers also have safety challenges. Even in the invisible part of the EM spectrum application to corneal, lenticular, retinal can result in lesion injuries. These measurements results follow heat transfer and rate process equations [33].

Lasers offer unique properties for medical application and their thermal effects on tissue heating can be consistent across different tissues [4]. Laser ablation for clinical use includes applications for dermatology, dentistry, neurosurgery, and urology [32]. Laser thermal therapy is a minimally-invasive technique that directly induces a thermal lesion. Laser-tissue ablation techniques have instrument parameters of wavelength, pulse duration, and exposure time, and are influenced by the optical, thermal, mechanical, and chemical properties of the sample tissue [32]. The spectral coherence of the laser beam allows focusing on the order of its optical wavelength. This would allow a tunable dye laser, say, to match its wavelength to the absorption bands of a chromophore [4]. Microsurgery can be performed on living cells making it possible to alter metabolism by thermally affecting organelles, macromolecules in submicron cell areas [4]. The power spectrum of a laser can span the UV to the NIR and provide a spatially-localized heating capability not possible with conventional light sources [4].

UV Laser

The ultraviolet (UV) part of the electromagnetic spectrum is broken up into bandwidths, similar to NIR. Vacuum UV is the spectrum from 100-200 nm, UV-C 200 to 280 nm, UV-B 280-315 nm, and UV-A 315-400 nm. At these higher energies, tissues are affected by indiscriminate ionization causing any ionized molecule to become more susceptible to having its bonding energies altered. In the UV spectrum molecules in tissue become more absorbing [4]. They can sustain UV photochemical events and thus a cell's DNA can be altered. Cell regulation and replication can also be affected by UV thru alterations in RNA, protein, and cell membrane structure. Sunburn is a UV-induced erythema and a typical inflaming response as the skins attempts to remove injurious phototoxins formed within the tissue [4].

Within the UV and visible range, the longer wavelengths scatter less and penetrate deeper into tissue [4]. UV excimer lasers can deliver photochemical and thermal reactions in the 193 - 351 nm region [4]. Most in vivo ultraviolet photochemistry is harmful [4]. Photon energy in the ultraviolet (200-400 nm) and visible (400-700 nm) wavelengths is sufficient to cause electronic excitation of specific chromophore molecules in cells [4]. Wavelengths outside of this bandwidth may be less effective in altering biological reactions because of lower photon energies. Light in the IR and UHF microwave range excites specific vibrational or rotational modes of a molecule. It does not have the energy, or frequency $E = hf$, strong enough to cause electronic transition.

DNA may also be damaged leading to abnormal differentiation of skin cells. Erythema is not the only indicator of phototoxicity. Radiation in the 250-290 nm range portion of erythema depends on the exposure time and is the most erythemogenic waveband. Erythemal efficacy decreases by a factor of 1000 for wavelengths from 290 to 320 nm [4].

Interaction Mechanisms

Photochemical interaction entails light affecting tissue structure thus creating a chemical effect, e.g., photosynthesis. Photodynamic therapy (PDT) is a photochemical interaction with relatively long exposure times and low power densities 1[W/cm^2]. It is implemented using special dyes injected into the bloodstream and accumulated in the tumor to induce photosensitizing effects. For example, a hematoporphyrin derivative (HpD) becomes toxic when radiated. HpD clears the healthy part of the body after 48-72 hours. In the tumor region where the vasculature is high but blood flow low, it remains at high lethal concentrations for up to 10 days. Initially, tumor cells have as much HpD as the rest of the body. However, because the tumor cells have much less clearance, they have a longer storage affinity for HpD. After a few days HpD in the tumor is about 30 times that of any residue left in the rest of the body. Laser treatment usually occurs a few days after initial dye injection. The aggregated HpD in the tumor becomes cytotoxic when light activated [9].

The governing parameter to measure hyperthermic activity is usually temperature. Thermal interactions occur as bulk absorption in molecular vibrational-rotation and nonradiative decay. First, a photon excites the molecule to a higher energy state. Its kinetic energy is shared inelastically with adjacent molecules and results in a temperature rise. When temperatures reach approximately 60°C the tissue becomes necrotic and darker than the surrounding tissue [9]. Staining, with hematoxlyin and eosin can be used to visually show the effects of tissue coagulation when heat is applied. As the temperature approachs 100°C, vaporization begins leading to higher pressures due to water confinement within the tissues. Thus the second phase the therapeutic laser processe causes water in the tissue to vaporize [29]. Eventually thermo mechanical effects occur which ablate the tissue by thermal decomposition [9]. Third, after a period of time carbonization begins. The tissue begins to darken on its own, without the aid of staining and this condition should be avoided because the darkening simply obscures the visibility. Finally, tissue melting occurs at near 300°C.

NIR energy is principally absorbed by water and protein and the tissue heating is due to absorption caused by water, protein, pigments and macromolecules. This process is strongly dependent on the incoming radiation wavelength [32]. A peak at 3μm is due to the symmetric and antisymmetric vibrational modes of water molecules [9]. Water absorbs light by resonance of symmetric and asymmetric stretching modes of the molecular bonds has strong absorption peaks from 0.96 to 6.1 μm [32]. The peptide bonds of protein spread across the infrared spectrum of the NIR [32], while both water and protein have a common absorption peak at 610 nm suitable for a laser-based ablation process [32].

Because ablation is initiated by the absorption of laser energy, the fluence of a laser beam represents the energy distribution as a function of depth. Fluence is determined by the surface radiant exposure and the absorption coefficient (μ_a), assuming non-scattering medium [32]. The higher the absorption coefficient, the more absorbed laser energy is concentrated at the surface of the target [32]. From Beer's law the fluence is an exponentially decaying function of tissue depth [32].

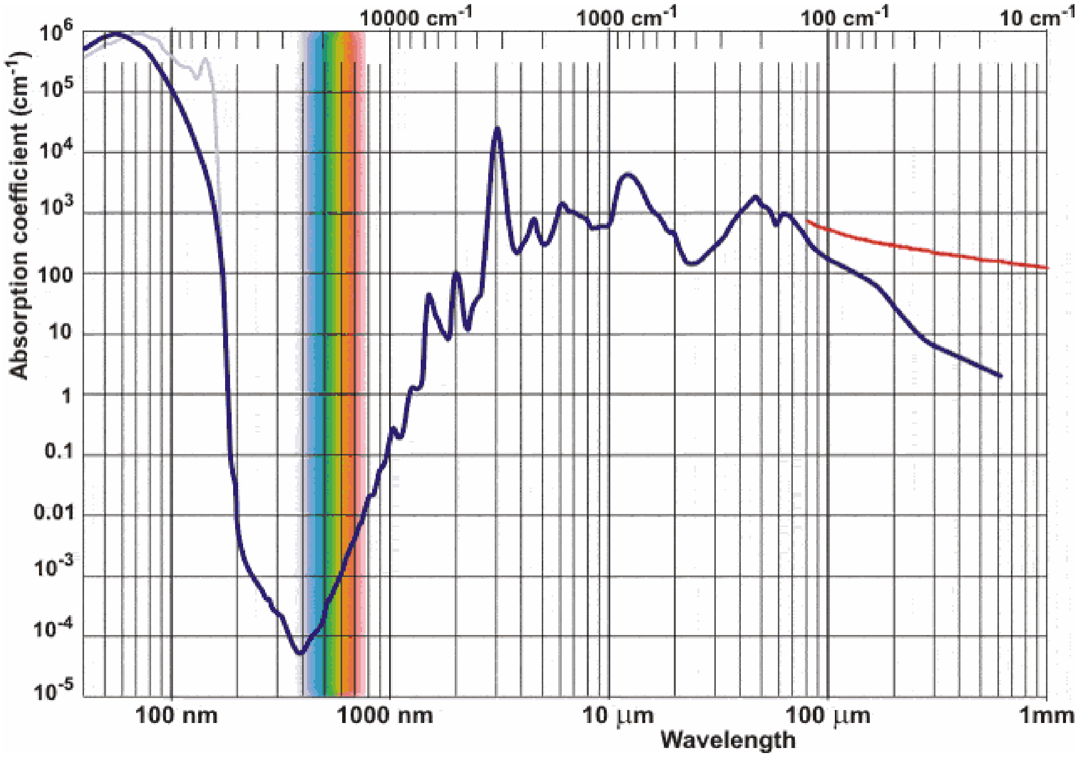

Figure 2.1. Water absorption profile, http://www.lsbu.ac.uk/water/vibrat.html

Heat generation is determined by the laser parameters, irradiance, exposure time and tissue absorption coefficient (a function of wavelength), Figure 2.1. Heat transport is a property of the tissue's heat capacity and heat conductivity, with loss of heat mainly through conduction and convection process [9].

Laser-induced interstitial thermometry (LITT) is a minimally-invasive surgery, e.g., irradiation treatment of malignant tumors. This method uses volume or surface scattering probes inserted into the tumor. The tumors are highly vascularized and this treatment also coagulates the blood vessels. The usual application of LITT is in the NIR where the light penetrates deepest [9].

Organic polymers are primarily covalently bonded. Two molecules bound by a common electron will either transit to a higher energy state or dissociate themselves when encountered by a photon with enough energy, say in the UV. The principle of photoablation employs photon energies which promote repulsive excited states of molecules thus causing mechanical action by fragmentation without necrosis, i.e., ablation for use in corneal surgery for correction myopia, or astigmatism [9]. Photoablation, or ablative photodecomposition, uses high intensity laser irradiation to make precision cuts while minimizing damage to the surrounding tissue.

UV laser ablation of tissue occurring at 193 and 248 nm produces better ablation than at the longer wavelengths of the visual or NIR. However, blood absorption at 193 nm hinders treatment [4]. Cytotoxicity of UV radiation is accomplished by DNA absorption in the 240-320 nm wavelength range which causes mutagenic alteration of cells through photochemical reactions with chromophores. A possible side effect of UV alteration of DNA is an increased possibility of passing on erroneous information to induce cancer by initiating an uncontrolled proliferation of cells. Excimer lasers were found to be less mutagenic than the UV light from mercury lamps [9].

Plasma-induced ablation occurs after too much power generates an ionized plasma causing an optical breakdown. Power densities of 10^{11} [W/cm^2] for solids and fluids or 10^{14} [W/cm^2] for air, in time durations of 100fs to 500ps, results in a cleanly-defined cut free of mechanical or thermal damage [9]. Plasma-induced ablation differs from photodisruption in that the electric field strength exceeds the dielectric or optical breakdown, depending on the frequency, Figure 2.2.

Photodisruption is a possible side effect of the ablative process where tissue fragmentation occurs due to mechanical effects. This technique is used for lens fragmentation and lithotripsy applications [9]. Other secondary effects include plasma formation and shock wave generation. In soft tissue, this implies mechanical side effect, of cavitation and jet formation. Cavitation occurs when the focal point resides within the tissue rather than on the surface and too much energy is applied.

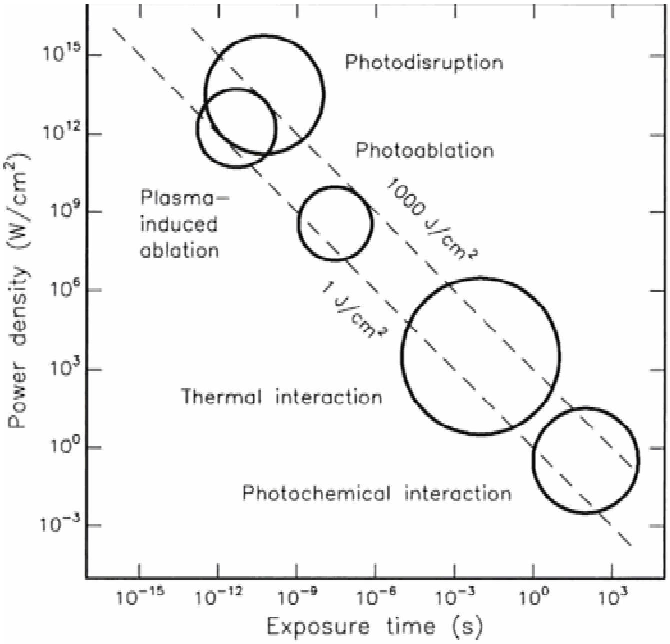

Figure 2.2. Power densities versus exposure time for various tissue interactions

Mathematical modeling tools used to predict the extent of skin injury use the heat conduction equation and rate process damage integral. These models predict damage due to multiple absorbing layers, reflection, blood perfusion, and steam formation [33]. The tissue absorption coefficient is combined with the incoming beam profile and power data to determine the amount of available energy deposition. This information is used to determine a source term for the heat transfer equation along with other thermal parameters to output is the temperature. Finally, this information is input, along with the rate coefficients, to results in a damage model, based on the work of Henriques et.al. [34]. This model is used to determine complete necrosis of the skin using rate coefficients, and predicts the damage associated with surgery done by laser irradiation in the visible spectrum. Little data on biological effects of thermal surgery using lasers exists for work done in the near-infrared wavelengths [33].

Photothermal and photomechanical are the two main categories of laser ablation and are categorized by pulse duration [32]. Absorption of laser light by a photothermal event transforms the optical energy into heat, and as described above results in vaporization, carbonization and eventually melting [32]. The thermal diffusion time is the time required for the initial laser energy to move beyond the target tissue resulting in thermal damage to the surrounding healthy tissue. There is minimal diffusion of heat when laser pulses are short because the thermal diffusion time is much longer than the pulse duration. The thermal energy resides locally in the target tissue without any significant effects of heat diffusion [32]. In this way, collateral damage can be reduced by optimizing wavelength and pulse duration [32]. The energy absorbed by the target tissue to accumulate in the focal volume determined by the laser spot size and its effective penetration depth, diameter, and length [32].

The pulse width of the laser inside the affected region results in a rise of temperature proportional to the absorption coefficient [32]. Temperatures greater than the boiling point of water are required to induce vaporization or ablation [32]. Tissue carbonization occurs when extra energy is absorbed because the laser pulse duration is greater than the thermal diffusion time [32].

Photomechanical exchange is the result of sub-microsecond laser pulses where the target tissue experiences a mechanical shock [32]. This occurs when the laser pulse time is shorter than the acoustic diffusion time. The acoustic diffusion time is the time required for the mechanical stress travel from the target tissue [32]. Mechanical stresses caused by thermoelastic expansion, shock waves and cavitation all trigger tissue ablation.

Lasers with pulse durations in the nanosecond range induce optical breakdown by thermal avalanche ionization generating electrons at the skin surface [32]. These electrons readily absorb incoming photons. Which increases their energy and causes more collisions generating even more electrons [32]. The effect generates plasmas with temperatures and pressures as high as ten thousand Kelvin and one Giga Pascal, respectively [32]. In turn, the heated material generates a mechanical shock that initiates tissue ablation by photodistruption [32].

2.2.3 Microwave Ablation

2.2.3.1 Theory

Microwaves are electromagnetic radiation, with wavelengths from 1mm – 1m, which can stimulate dipole oscillation generating heat by dielectric hysteresis [35]. An electric dipole may be viewed simply as two charges, equal in magnitude and opposite in polarity, separated by some distance. A neutral atom placed in an electric field induces a dipole moment. An example of this is water which has a permanent dipole moment because it is a polar molecule. Electronegativity in some molecular combinations allows an unbalanced sharing of bonding electrons, and in the case of water, two of the negative p-orbitals of its oxygen atom each have a positively charged hydrogen atom covalently bonded to it giving the molecule its natural polarity. The repulsive nature of the two hydrogen nuclei cause the σ bond axes to widened to 104.5°.

When water, or any polar molecule, is placed in an electric field there is an induced torque on the already present permanent dipole moment which causes the polar molecule to reorient itself to the field. A phase dependence exist during heating which is caused by electron cloud mobility [36]. The lag between the electric field and polarization of the material is affected by frequency and relative permittivity [36]. If the driving frequency oscillates too rapidly the dipole will lag behind the field leading to energy loss through heating.

Thus, any substance with an electromotive force impressed across it will generate a current which in turn causes some amount of heat energy to be dissipated. Additionally an AC potential dissipates energy via dielectric hysteresis. The dielectric constant of a material is a complex argument whose terms consider the total current as the vector sum of charge and loss currents [36]. The relative permittivity of a substance is a function of wavelength and is used as a measure of how easily a material is polarized [36]. The decrease in hydrogen bond strength with temperature lowers the dielectric permittivity allowing the water molecule to oscillate at higher frequencies.

Because the dipole can switch faster there is a reduction in drag and dielectric losses. This allows energy to penetrate further into the substance and, as a consequence, heat more uniformly because the radiation is not totally adsorbed by the first layer of water [36].

Microwaves are a nonionizing radiation source because there is insufficient energy to directly change a substance chemically. However, exposure from high intensity microwaves can still cause burns as a result of dielectric heating. For example, exposing the eye to microwaves can produce cataracts through protein denaturation because the lens and cornea contain no blood vessels to carry away the heat.

2.2.3.2 Application

Microwave ablation (MWA) is a thermal therapy that induces the water molecule to rotate causing thermal coagulation of the target tissue. The alternating polarity of the electric field causes the water molecules to be realigned which results in frictional heating with the surrounding molecules and increases in the kinetic energy of the atom/molecule and excess heat [27, 37]. Organ tissues are lossy dielectrics meaning they can absorb large amounts of energy [35].

The current causes resistance heating which destroys the affected tissue while minimizing damage to the adjacent normal tissue. These waves cause secondary heating due to the electrical resistance within the tissue [6]. A dipole antenna requires some means to focus or restrict energy to a specific area by using different antenna geometries [6].

Microwave thermal therapy incorporates a tiny dipole antenna inserted into the tissue. Electromagnetic waves in the 0.3-2.5 GHz range generate electric currents with power settings of up to 60W [6, 38]. MWA antennas are concentric electrode needle assemblies approximately 25cm in length [6]. The inside needle is a monopolar 18-gauge [1.024 mm] needle thin enough to pass through 14-gauge [1.628 mm] styleted sheath. Microwaves are emitted from the distal segment of the inner monopolar probe. An array of these antennas increases thermal conduction enabling destruction of tumors up to 3 cm in diameter [6].

The various antenna configurations for microwave applications have a dramatic effect on the shape of the electromagnetic field and power deposition throughout the affected tissue [38]. The lower the frequency, the deeper the lesion, which reduces extraneous heating of equipment [38]. However the electrical properties of tissues in the microwave frequency range change as they are heated [6]. To destroy an entire tumor several antennas are usually required. This can be accomplished with either of two strategies [6]. One would be to use the coherent nature of electromagnetic energy to generate interference patterns to match the shape of the tumor. The other is to drive the signal randomly, producing incoherent interference patterns. This can be accomplished by the use of a number of antennas independently to create a geometric power configuration that conforms to the tissue volume [6]. Thermal conduction is the mode of heat transfer outside the volume affected by the electromagnetic field [6]. The induced heating minimizes the need for a surgical procedure by reducing the amount of tissue affected [39, 40].

Salt operates as a eutectic by suppressing the dielectric constant. This is accomplished by decreasing the water structure, thus lowering static dielectric permittivity [36]. Without salt, water alone becomes a poorer absorber of microwave energy. With the increase in temperature, the phase lag decreases allowing the ions to react faster at lower frequencies and so produce frictional heating [36].

MWA, like radiofrequency ablation (RFA), applies heat energy interstitially using dielectric hysteresis [35]. Both techniques require the placement of an electrode into the target tissue which requires some type of guidance. A small laparoscopic incision is made and this antenna is place in the tissue. With visualization by US or CT scan, places a thin antenna in the tumor. Microwaves from the antenna propagate and impart energy that causes water molecules within the tumor to spin producing heat from friction. Unlike RFA there is no current flow with MWA and thus no need for grounding pads or retractable pads. However, similar to RFA, MWA produces a hyperechoic region around the needle which results in an ablated tissue region that tends to be more elliptical, a prolate spheroid.

MWA has the advantage of heating a larger volume of tissue and at a rate that is faster than RFA. There is no need for an electrical conduction path and property changes of the affected tissues are less critical to MWA than with RFA [35]. The application of RFA induces a rapid rise in the impedance which stifles the progress of current into the tumor thereby decreasing the efficiency of the application [35]. However with MWA no conduction path is required. Thus temperatures as high as 150°C have been measured using MWA [35]. MWA may be operated simultaneously employing multiple antennas which can operate without mutual interference [35]. With RFA, the use of multiple electrodes requires a switching algorithm to enable only one electrode to run at a time. The superposition of EM fields from MWA increases the potential for transcutaneous ablation from selective heating thus avoidance of target areas is possible [35]. The skin surface can experience excessive heating because of the large electrical impedance difference between the tissue and air [6]. MWA does not require grounding pads thus superficial skin burns are not going to happen. MWA unlike RFA is not contact dependent [38].

Lazebnik et al. investigated study the ultra-wide band microwave dielectric properties of normal, malignant, and benign breast tissues [41]. An open-ended coaxial probe was used to measure microwaves from one half to twenty gigahertz each tissue sample. A one-pole Cole–Cole model was used to analyze the complex permittivity data set, Figure 2.3. Dielectric property shifts with temperature allowed the temperatures local maxima at constant frequency to be calculated [36].

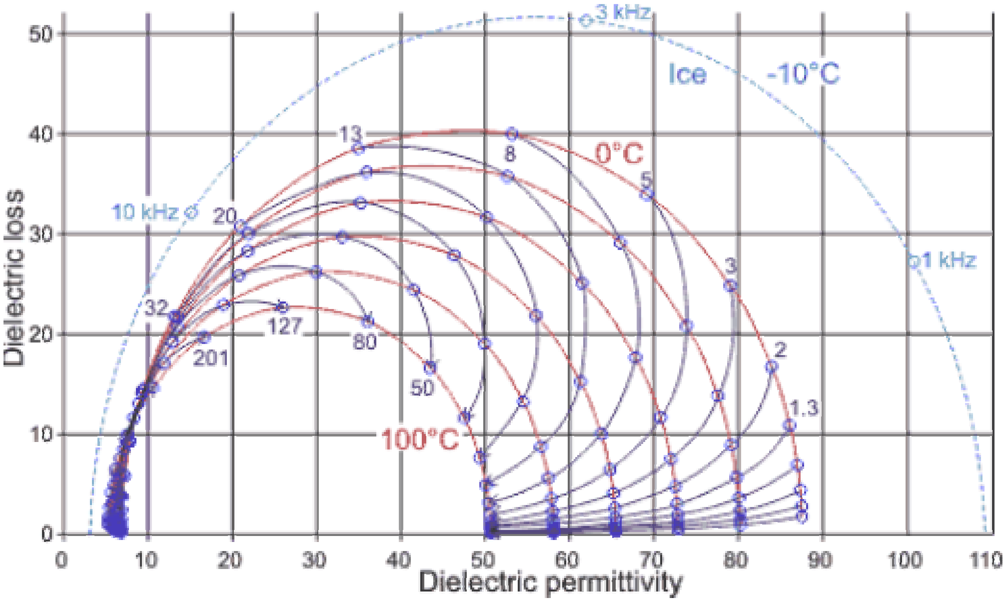

Figure 2.3. The Cole-Cole plot shows the variation of temperature with wavelength

The dielectric property contrast within the microwave range between breast malignant and normal adipose-dominated tissues was as large as 10:1 [41]. The contrast in the microwave-frequency dielectric properties of breast tissue was no more than about 10% [41]. Breast cancer detection uses non-ionizing energy in the microwave frequency range because this range allows a balance between penetration depth and spatial resolution, image detection and focusing. Thus, it was established that dielectric properties using microwave radiation of normal, benign and malignant human breast tissues is from 0.5 to 20 GHz [41], and that the dielectric properties of normal tissue span a wider range and are determined primarily by adipose tissue [41].

Simon et al. used three microwave generators connected to an antenna using coaxial cable to produce up to 60 W of power at a frequency of 915 MHz [42]. The antennas were then arranged in a three-probe triangular configuration and spaced at 1.5, 2.0, and 2.5 cm using 13-gauge, 15-cm long wire with a 3.6 cm active tip. All MWA were performed under US guidance with tumor logistics identified with CT or MRI. The microwave generators were run simultaneously to synchronize the ablation with 45 W of power for 10 min and the ablated coagulation was estimated based on the appearance of the transient hyperechoic zone. For RFA the hyperechoic echo was found to be roughly 8 mm of the ablation margin.

2.2.4 Radiofrequency Ablation

2.2.4.1 Theory

Radiofrequency Ablation (RFA) energy is delivered through a 14–21 gauge electrode extended in a radial arched fashion to increase its effective area. The RF energy vibrates the atoms within the cell with a varying 8-30 MHz signal and generates cellular heating via ion agitation which is proportional to current density. Tissues close in proximity to the active electrode receive the most energy and this characteristic limits any necrosis to tissue, 2-5 cm in diameter, in the immediate vicinity of the electrode [43]. The heat treatment inherent to RFA slows bleeding therefore reduces blood loss.

2.2.4.2 Application

RFA is an effective minimally invasive treatment of tumor growth and has been FDA approved since 1997 for patients with tumors not suitable for conventional surgery. RFA is used to treat tumor growth in the liver, brain, musculoskeletal system, thyroid and parathyroid glands, pancreas, kidney, lung, and breast [43]. RFA is a percutaneous technique for the treatment of tumors without their removal, and therefore it is less invasive and less expensive [43]. It is a non-ionizing in situ technique used with minimal sedation which reduces pain and soreness for the patient. An RFA procedure may last up to 30 minutes depending on tissue characteristics and temperature requirements [44]. Various imaging techniques can all be used for probe guidance and treatment monitoring. These include computed tomography, magnetic resonance imaging, positron emission tomography, and ultrasound.

RFA is performed using either a monopolar or bipolar technique. Either approach utilizes current passing from the noninsulated tip of the electrode through tissue to generate ion agitation, which in turn, generates heat by means of friction [43]. The monopolar technique is a more common tumor ablation application using a large grounding pad as a dispersive electrode. The bipolar technique uses a smaller passive electrode placed within five centimeters of the source electrode as a means to complete an electrical circuit [43].

Conventional RFA produces a maximum limited lesion diameter of approximately 1.6 cm [45]. Goldberg et al. used a conventional monopolar set-up to test both ex vivo an in vivo effects on liver and muscle tissue. Lesion diameters correlated with the exposed electrode tip length. A non-uniformity of electrode surface temperatures was found, as was temperature variation along the electrode. The temperature variation increased with tip temperature and electrode tip length, the highest being near the electrode endpoints. For temperatures less than 50°C a strong correlation of coagulation was observed between diameter with the local mean temperature. Electrode surface temperature increased with coagulation necrosis diameter at 80°C, and tissue charring and cavitation increased circuit impedance (limiting current flow) which resulted in inconsistent results for temperatures higher than 110°C [45]. Generally the relationship of coagulation diameter to electrode surface temperature was similar to ex vivo experiments. The length of coagulation necrosis achieved in vivo was comparable to that observed ex vivo, but with in vivo tests the diameter was considerably smaller than ex vivo [45-47]. The minimum temperature was 8.5°C higher along with a corresponding greater variation in electrode temperature for in vivo ablation [46, 47]. It is thought that perfusion-mediated tissue cooling via blood flow is largely responsible for decreased in vivo necrosis [46, 47] and these results imply that a larger volume of tissue necrosis per treatment can be obtained by increasing electrode tip length [46, 47].

The volume of coagulation necrosis by RFA can be increased by several techniques. The physical design of the probe may be altered as a multiprobe, hooked, bipolar array or intercooled assembly [43]. Saline can be injected intraparenchymally prior to and during RF application [43]. RF current can be programmed to maximize the energy deposition which reduces the side effects of tissue boiling, charring, or cavitation [43].

Improvements in the technique have included the use of an array of electrodes, each with 3-cm tip exposure, to increase the effective diameter of coagulation necrosis [46, 47]. Increasing the volume of coagulation necrosis from that of a single probe affords a measure of flexibility in probe configuration and spacing to match a given tumor geometry. One constraint of this method is that the probe spacing needs to be no more that 1.5 cm apart [46, 47]. A hooked needle has been tried but it was only able to deliver a maximum output of 50W for an initial treatment due to boiling and charring [48]. This system is more reactive to blood flow and heat sink than a cooled-tip system.

Another multiprobe array uses an array of stiff wires in the shape of an umbrella branching from a single cannula [48, 49]. This arrangement was able to produce a spherical region of coagulation necrosis 3.5 cm in diameter [49]. Bipolar arrays utilize a second ground electrode within 4 cm of the active electrode. This configuration causes heat to be generated both at the active electrode and the grounding probe and results in a coagulation region larger than with a conventional monopolar device [49].

Saline solution injection is another technique used before and during RFA to increase the volume of coagulation necrosis. Saline injection increases conductivity while decreasing electrode temperature and increases the lesion diameter to as much as 5.5 cm [50]. Saline administered prior to RFA has resulted in a larger volume of coagulation necrosis in both ex vivo and in vivo experiments. According to Scudamore et al., one possible explanation is that the effective surface area of the electrode is augmented by the tissues' increased local osmotic pressure. Tissue cooling and decreased tissue impedance increases the tolerance of the tissue to sustained high power settings. This allows the heated saline to diffuse heat throughout the tissue more uniformly [51]. However, the resulting coagulation necrosis when using saline injection becomes more irregular in shape with an overall volume of tissue harder to predict [50].

Another innovation that has resulted in greater energy deposition and coagulation necrosis is the use of internally cooled 14 - 18 gauge electrodes which have been designed to increase output and prevent tissue boiling [52]. A cooled-tip needle clearly affects a much larger lesion than an expandable needle because of increased power delivery capacity up to 200 W [53]. Cooled-tip lesions were larger than those induced with the expandable needle. However, the expandable needle lesions were much more reproducible in vitro. The cooled-tip needle cluster was constructed of three active electrodes 0.5 cm apart. This arrangement produced a more uniform oval shape than a 3-cm umbrella probe mentioned above, and was shown to be more stable [53].

Clustered electrodes have also been investigated to test whether a densely-packed arrangement of electrodes would act as a single large electrode [54]. Three 2-cm, internally cooled probes, spaced 0.5–1.0 cm apart, produced better results than electrodes spaced 1.5–2.5 cm apart [54]. The former could produce a 4.1 cm spherical focus of coagulation whereas the latter could only create smaller more irregular zones of coagulation [54]. Thus electrodes placed less than 1 cm apart generate spherical regions of coagulation necrosis that would otherwise require similar electrodes assemblies spaced 1.5–2.0 cm apart [54].

Applying a RFA duty cycle of pulsed RF energy enables more heat dissipation to prevent charring and cavitation [55]. RFA has been applied ex vivo to liver tissue using internally-cooled probes using peak currents as high as two amps. One duty cycle was 15 seconds full power then 15 with current lowered to one half amp for 15 seconds, cycled over a period of 15 minutes. This generated a coagulation diameter approximately 3.8 cm when a 4-cm probe was used [55]. When compared to a continuous energy input, without increases in impedance, and current applied to the same probe arrangement, the average coagulation diameter was 3.3 cm. Pulsed RF energy generates a more rapid increase and higher overall tissue temperature than can be achieved using a single treatment session [55].

In summary, successful tumor ablation using RFA as a minimally-invasive thermal energy source is achieved when the tumor is completely destroyed in one session a surgical margin of up to one extra cm [53]. Generally, tumors less than 2 cm can be treated with one RFA application. Those tumors 2 to 3 cm in diameter require six overlapping ablations and those greater than 3 cm in diameter require at least 12 overlapping ablations [56].

A certain amount of ability is required to accurately place the electrodes, thus some variability in the success of the technique can be due to placement errors [53]. As a consequence, optimizing the affected volume of tissue to be destroyed in a single treatment is important, because it determines the resulting maximal applied volume, number of applications, and probability of complete tumor treatment. Blood flow within the blood vessel removes enough heat to allow the tissue to be preserved [51]. The effects of heat sink are more evident when the generator power is lowered [53].

2.3 Quantum Dots

QDs are direct band gap semiconductor nanoparticles with strong fluorescent properties and unique optical properties. Their fluorescence emission can be tuned by adjusting the QD diameter. The quantum confinement effect decreases with increased diameter. A core/shell configuration overcomes this limitation and extends the emission into the near infrared (NIR), without changing the size of QDs [57-59].

Given similar material and assembly, larger QDs will fluoresce at longer wavelengths. The photoluminescence from a CdSe QD can be tuned to cover the visible spectrum (465 nm – 640 nm) from green (517 nm/2.4 eV) to deep red (730 nm/1.7 eV) simply by colloidally adjusting the QD diameter from 2 to 20 nm [60, 61]. This fluorescence dependence on band gap energy may be adjusted by simply varying the diameter and shell thickness. Thus, quantum confinement effects determine an emission signature which may be 'tuned' by simply varying the size of the QD assembly. This makes QDs applicable for medical application, where cell or tissue visualization can reveal important transport behavior [62].

The emission of a QD assembly is determined by band alignment and charge carrier spatial distribution at the core/shell interface. The spatial charge distribution determines the magnitude of the surrounding electron-hole Coulomb attraction of the electron hole pair [63]. For a Type I QD configuration both electron and hole are confined to the core structure. A Type II QD has either charge carrier confined to the core, the other in a shell whose valence band energy is lower than the core carrier. This physical separation results in light emission with reduced energy resulting in a longer emitted wavelength, i.e., a Stokes shift.

Semiconductors are typically made from compounds containing elements in groups II and IV, III and V, or IV and VI. QDs can be grown using colloidal chemistry, epitaxy, or lithography [64]. Colloidal chemistry typically manipulates elements composed in the II and VI periodic column, i.e., CdS, CdSe. Lithography is a pattern masking process and epitaxy involves growing QD substrates. Unlike bulk semiconducting materials, QDs are relatively easy to tune. Colloidal QDs are afflicted with bleaching and blinking and therefore do not provide enough coherence for quantum information purposes [64]. Epitaxial QDs are assembled within a crystalline matrix having a larger band gap which can operate for extended periods of time [64]. Epitaxial QDs can be grown using molecular beam epitaxy or metal organic chemical vapor deposition [64]. A gelatin may be introduced to slow the chemical reaction providing regulation of growth rate and provide a biocompatible coating for *in-vivo* applications [62].

Persistent luminescence QDs are a relatively new nanoparticle application [65]. These QDs are activated before administration to the patient. The only instrumentation is a passive, noninvasive device necessary to measure the emission of the nanoparticle after it is in the body. Other noninvasive means available measure the nanoparticle after it has been dispersed to the target location. The major advantage of these systems is to avoid the need for an excitation source. As a result, no signal diluting autofluorescence is present.

2.3.1 Tumor Transport of Quantum Dots

Diffusion is the main driving mechanism for small molecules in normal tissue while convection is responsible for transport of larger macromolecules. The heart generates a hydrostatic pressure responsible for pushing water from the capillaries into tissues. The interstitial fluid that surrounds cells contains nutrients made available by blood vessels and waste products to be removed by either blood or lymph flow. However, the tumor has no active lymphatic vessel structure [66]. In this environment the movement of macromolecules is driven by interstitial and microvascular pressures alone [67].

Deep within the tumors' interior the interstitial fluid has a high, uniform pressure with a steep gradient near its surface. As a result, larger molecules have difficulty being transported because they rely on convection, which only occurs near the tumor surface [66, 68]. Smaller molecules are more effectively transported across tumors and more readily cleared to the bloodstream [27, 28]. Generally, in solid tumors the increased interstitial fluid pressure reduces blood supply resulting in a corresponding decrease in the delivery of any cancer drug therapy.

2.3.2 Near Infrared QD Imaging

Blood hemoglobin and water have low absorption rates in the NIR. Though most visible light is absorbed by hemoglobin, water, and lipid, these same tissues are relatively transparent to radiation in the NIR range (700~900 nm) and can travel through tissue a few centimeters, further than that achieved by visible light [69, 70]. A critical indicator of tissue function is hemoglobin concentration and oxygen saturation. Near infrared spectroscopy (NIRS) can measure these concurrently [71].

NIR is able to penetrate further into tissue than visual light because scattering events are generally more forward biased and occur more than absorption events [72]. Thus, fluorochromes designed to emit in the NIR allow tissue penetration of a few centimeters. Similar imaging techniques in the visible spectrum would be limited to penetration depths of only a few millimeters.

Biomedical imaging has been feasible in the NIR because increased detector sensitivity and use of monochomatic illumination enables the use of higher power densities [117]. Fluorophores in the visual and NIR can be introduced into tissue simultaneously thus allowing both signals to be measured independently. Also, restricting two or more signals to the NIR region allows measurement of deoxygenated and oxygenated hemoglobin, and total hemoglobin concentrations in deep tissues [70].

Tissue scatters light through membrane interfaces of cells, collagen and extracellular matrix [72]. Tissues also have significant autofluorescence in the visible spectrum and maximum transparency in the NIR because living tissue doesn't have chromophores that absorb in this bandwidth [69, 73].

Some molecules become fluorescent when excited by specific wavelength radiation, usually in the UV/VIS part of the spectrum. NIR fluorescence imaging reduces tissue autofluorescence. Consequently there is less background signal, or noise, associated with the use of NIR because the surrounding media is not participating in the illumination. NIR QDs are superior in brightness and photostability over fluorophores for diagnostic imaging [74]. A working example for the use of a VIS/NIR camera system is from used in veterinary surgery [75].

2.4 Tissue Phantom

Tissue phantoms replicate the optical properties of biological tissue. They are useful for calibrating, validating accuracy and repeatability for newly developed optical imaging and spectroscopy experiments. The important imaging parameters are the absorption and scattering characteristics of the representative specimen. Tissue phantoms can be used to replicate optical properties of tissue requiring scattering, μ_s, and absorption, μ_a, coefficients at specific wavelengths and to cover a wider bandwidth. This also includes biocompatibity to accept hemoglobin, melanin, or fluorophores and to measure transient behavior [76]. Tissue phantoms are also used for quality control to calculate dosage delivery for diagnostic and therapy applications, for x-ray focal spot size determination, and to detect contrast limits for ultrasonic and MRI applications.

The basic criterion of any tissue phantom is to match the light influencing characteristics of the replicated media. The optical properties of gelatin phantoms are close to human tissue optical properties [70]. Depending on the media thickness, some parameters are more important than others. For thicknesses less than 1 mm the absorption, μ_a, and scattering coefficients, μ_s, and anisotropy factor, g, should all be matched to the original tissue [76]. Intermediate thickness scattering lengths can be well-approximated using the reduced scattering coefficient, $\mu'_s=(1-g)\mu_s$, and bulk tissue transmission requires the use of an effective attenuation coefficient, $\mu_{eff}=(3\ \mu_a\ \mu'_s)^{-1/2}$ [76]. For measuring tissue transmission, matching u_{eff} is adequate, but tissue spectroscopy requires both u_a and u_s to be properly defined as they are considered to be wavelength dependent [76].

Tissue phantoms designed to mimic human tissue for diagnostics can be adapted to distinguish between newborn, child and adult, and soft, lung or bone tissue. Hybrid phantoms for multimodal application include biochemical, electrical, magnetic and thermal properties [76].

Water and hydrogel materials like gelatin or agar provide a biological medium which can accept organic molecules for laboratory work [76]. Gelatin is made by denaturing the molecular structures of collagen through hydrolysis [77]. Collagen gives structure to connective tissue because the protein contains helical regions that trap water molecules [78]. There are three main structures in a collagen [77]. The primary structure consists of amino acids in peptide chains [77]. The secondary structure describes the function of the alpha helix and beta sheets formed from the primary structures. The tertiary structure refers to the ordering of the amino acids at a distance, the folding and other noncovalent interactions of hydrogen and disulfide bonding and other ionic exchanges [77].

Denaturation of a hydrogel material destroys the ordering of the hydrogen bonds making random length chains of smaller molecular residues [77]. Above 40°C these smaller molecules are in a random coiled state [77]. A reversible transition in this structure takes place when the temperature drops below 30°C [77]. This transition can be detected optically and with large temperature gradients the partial denaturation process results in the formation of a malleable gel [77].

A collagen gel has a high content of glycine, proline and hydroxyproline amino acids derived by controlled hydrolysis [78]. Gelatin tissue phantoms consist of solids dissolved in boiling distilled water, scattering and absorbing agents and possibly cross linking agents to keep the gelatin from melting at higher temperatures [70, 79-81].

Agar is a polysaccharide made of agarose and agaropectin [77]. Native agarose is hydrophobic and thus requires a detergent to cause it to hydrogen bond with a water molecule [77]. Agarose chains are in a randomly coiled state above 60°C [77]. As the temperature is decreased, intramolecular hydrogen bonding causes the molecular agarose chain to become more rigid [77]. Finally gelation of agar occurs at 40°C and intermolecular activity takes place in microcrystalline junctions with further decrease in temperature [77].

Unlike gelatin, agar can be used over a wide range of temperatures without melting or having its optical properties altered. Generally an agar mixture is dissolved in distilled water, heated to 60°C and formed at 40°C [79]. Agar alone has low absorption and turbidity but can oxidize when heated causing an increase in the absorption coefficient [79].

Common scattering agent are Intralipid (an emulsion of soy bean oil and egg phospholipids), other lipid-based emulsions, titanium or aluminum oxide powders, and polymer microspheres [79, 80]. The scattering coefficients of tissue phantoms using larger polystyrene microspheres is determined by use of the total attenuation coefficients and calculated by Mie Theory [81]. The total attenuation coefficient, the scattering coefficient of a pure scattering sample, is then obtained from the unscattered transmittance via the Beer–Lambert law [81]. The three most used scattering agents are lipid and polymer microparticles, and white metal oxide [76]. Lipid microparticles are similar to the bilipid membrane. Polymer microspheres can be manufactured with a high degree of control [76]. White metal oxide is composed of titanium dioxide or aluminum oxide powders and can also be produced with a high degree of control [76]. Recently, gold nanoparticles have been used because they exhibit a large scattering cross section and are considered biocompatible [76].

Absorbers used in tissue phantoms can also vary depending on application [76]. For biological use, tests performed with hemoglobin and cells commonly use dyes or inks as more stable absorbers [76, 79, 80].

Synthetic phantoms are made of materials like polyester epoxy, polyurethane resin and RTV silicone. These are more permanent assemblies and better suited for equipment calibration [76]. Polystyrene microspheres are used as tissue phantom material with fractal size distribution enabling reproduction of the phase function, absorption and scattering coefficients for a specific wavelength [82]. Polyvinyl alcohol (PVA) is an optically-clear, viscoelastic non-Newtonian fluid [83]. Scattering can be simulated with the addition of titanium dioxide or polystyrene microspheres, and absorption varied with the use of water-soluble dye or ink [83]. Borax is added to PVA solutions to cause cross-linking to occur [83].

A HIFU tissue phantom material made of polyacrylamide gel and bovine serum albumin has been developed to closely match the acoustic attenuation, velocity and tissue material properties [84]. It was initially formed into a uniform optically transparent medium which turned opaque whenever heated to temperatures greater than 70°C [84]. This material provided a quantitative tool for the development of HIFU systems and to test the validity of software simulations. During HIFU treatment, a steady temperature increase within the target zone was observed resulting in a maximum mean temperature of 75°C. A site intensity of 1680 W/cm2 was chosen based on previous canine studies [21]. Higher site power induced tissue cavitation which caused uncontrollable tissue destruction and was evident as cavities.

CHAPTER 3

QUANTUM DOT MEDIATED THERMOMETRY

3.1 Introduction

Advances in cancer diagnostic technology are shifting the surgical management of cancer treatment towards more minimally invasive techniques as the detectable tumor size becomes smaller. Thermal therapy is a technique where localized heating is used to destroy the tumor while minimizing the damage to adjacent tissue. Accurate intraoperative monitoring of the thermal lesion is critical to this technique. Current intraoperative monitoring capabilities are significantly impaired by limited accuracy and difficulty of intervention. An intraoperative imaging modality to provide accurate temporal and spatial information in real-time would greatly increase surgical efficacy.

Recent developments in nanotechnology show great promise for non-invasive tumor imaging using nanometer size particles, QDs. The QD has strong fluorescence emission characteristics within a very narrow spectral range [61]. Recent studies have shown near infrared (NIR) emission spectra QDs as successful in vivo imaging probes for cancer detection and imaging [37, 69]. Recent studies indicate that the fluorescence emission intensity of QDs varies considerably with temperature [85-87].

In this chapter, a QD-mediated thermometry is developed and its hardware, software, and feasibility as an optics platform are characterized and demonstrated. The developed system is designed to monitor the thermal features of tissue non-invasively by measuring the fluorescence intensity of fluorescent material, i.e. QDs, accumulated in the tumor prior to surgery. If such a therapy can be adopted in clinical medicine, it will significantly improve the efficacy of minimally invasive surgery by providing accurate information of thermal lesion and minimizing unnecessary healthy tissue damage.

3.2 Background: Fluorescence of Quantum Dots

The QD is a nanoparticle made of synthetic semiconductor material 1 to 100 nm in diameter. Typically made of direct band gap materials, QDs fluoresce with a narrow bandwidth, have greater quantum yield, and a higher photobleaching threshold than organic fluorophores. This fluorescence can be red shifted by simply increasing the QDs' diameter. However, this approach can only be exploited within a narrow bandwidth because the band gap energy diminishes with increased diameter. This limitation is overcome with the introduction of the core/shell QD. This QD assembly has the same dimensions as a conventional QD but is coerced to fluoresce beyond the red spectrum and even into the NIR where it has application for tissue imaging [57-59]. This characteristic is accomplished by passivating the crystal with a shell material having wider band gap energy which increases the quantum yield of the assembly by decreasing its lattice vibrations.

An electron may absorb a photon causing it to transit from valence to conduction band leaving a positively charged hole. Together they form an electron-hole pair, the exciton. Within a bulk semiconductor, the conduction and valence band energy levels are continuous allowing electrons to move in all directions [61]. QDs however, have a large transition dipole moment when compared to similar bulk semiconductor material and thus fully localize the exciton.

Oscillator strength is a dimensionless quantity used to express the energy of transition from one quantum state to another [61]. Inter-band optical transitions shift toward the shorter wavelengths as the diameter of the QD is decreased thus increasing the energy of the confined state [61]. This leads to incremental density of states like those present in atoms. Optical transitions occur between these discrete states in the nanometer range [88]. Alterations in the physical confinement cause a large change in the density of states because of the surface to volume ratio of the QD. At these length scales, the diameter of the QD is smaller than the de Broglie wavelength of thermal electron transition, $\lambda = h/p$, where h is the Plank constant and p, particle momentum. Thus, the inter-band transition energy approaches that of the bulk material when the QD diameter increases towards λ [62]. The band gap energy can be influenced at these length scales because their physical diameter is less the exciton Bohr radius (EBR). EBR restricts of the size of the exciton through quantum confinement which greatly increases the probability that the crystal will fluoresce when it absorbs a photon with enough energy. When the semiconductor length scale approaches its EBR quantum confinement rules are enforced and the electronic behavior becomes discrete [61]. A QD has a geometric constriction confining the exciton in all three dimensions [61].

Quantum confinement energy increases exciton generation resulting in narrow bandwidth fluorescence. Thus, absorption and emission spectra occur in a narrow energy range whose quantum confinement is best described as a delta function [61]. Because the characteristic length of a QD is less than the EBR, the emission spectra are more intense [61] [85]. QDs exhibit this by fluorescing with a narrow symmetric emission and a relatively long lifetime. Also, unlike conventional fluorophores, QDs have an exceptionally wide excitation profile allowing for a much higher probability of absorbing excitation energy.

Quantum yield (QY) is a statistical measure of the average number of photons needed to cause one to be reemitted. The chemistry of the QD core can affect the QY. QDs with free electrons and material defects in the lattice will reduce the QY through nonradiative transitions. These nonradiative events in the bandgap (e.g., phonon activity) decrease the electromagnetic output of the QD. Electrons within semiconductors cannot transit by thermal energy alone because the energy band gap is too large. To control these electrical properties, impurities are inserted to decrease the interband gap distance, reducing the transition energy.

The defining feature of the QD is the energy (band) gap separating the conduction and the valence energy level bands. For a bulk semiconductor material the band gap is a fixed parameter of the material. The QY of a QD may be increased by incorporating a semiconducting coating having larger band gap energy [89]. For instance, CdS may be applied to a CdSe kernel to generate a core/shell structure. This enhances photoluminescence because the higher band gap material in the shell forces the exciton to remain in the CdSe core [37]. A shell with only several molecular layers can reduce nonradiative transitions; and thus minimize surface irregularities increasing the likelihood that an electron will relax to the valence band. The shell can also be modified to incorporate a biological surface layer. This allows binding of specific molecules, ligands, or peptides, giving the QD a chemical flexibility which would increase solubility into nearly any solvent.

3.3 Materials and Methods

3.3.1 Quantum Dots

The QD evaluated in the present study was a Type II CdSe/ZnS (core/shell) structure with a peak emission wavelength at 620 ± 10 nm (Evident Technologies, Troy, NY). These QDs were embedded in 60 μm thick polymer with a standard concentration of 0.5% by unit weight of QDs (15.2 nM of core QDs). The sample arrived as a composite assembly, sandwiched between two microscope slides, having a 15 mm diameter viewing area.

3.3.2 Thermal Imaging System

A thermal imaging system was developed within our group to characterize the temperature-dependent fluorescent intensity of QDs [90], Figure 3.1. The fluorescence intensity of the commercial QD slide was imaged at various temperatures during heat cycling, between 5°C and 70°C, to quantify the fluorescence emission intensity change as a function of temperature. The QD slide temperature was controlled by a thermoelectric cooler (TEC) (Melcor, Trenton, NJ or SP5517-00L, Marlow, Dallas, TX). The TEC was sandwiched between an aluminum plate and a copper heat sink with dielectric paste (Arctic Silver, Visalia, CA) placed on both sides of the TEC to assist heat transfer, Figure 3.2. Heat generated by the TEC was removed through the copper heat sink by circulating cold N_2 vapor venting to atmosphere or through a recirculation bath (FP50-MC. Julabo, Vista, CA) using propylene glycol as the working fluid. Communication between the temperature controller and devices was through a T-type thermocouple (Omega, USA). Power to the TEC was controlled by a temperature controller (MTTC-1410, Melcor, Trenton, NJ).

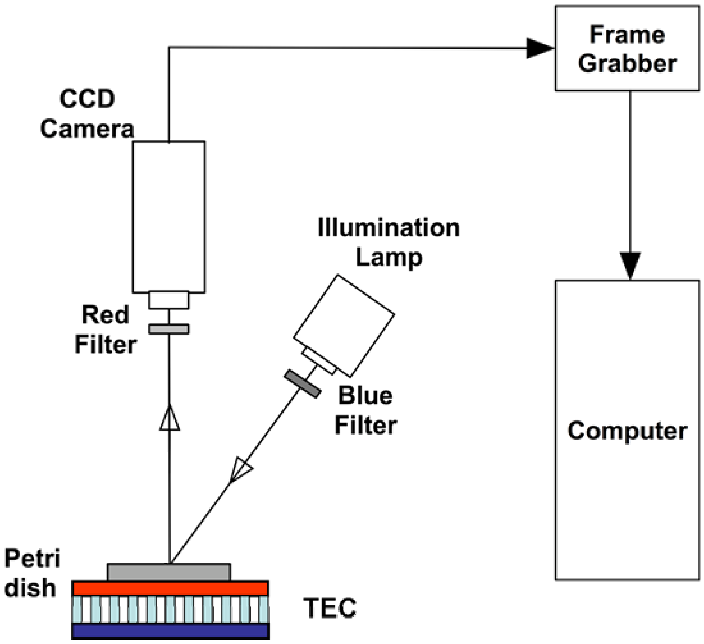

Figure 3.1. Block diagram for the thermometry system used for measuring the intensity response of a sample

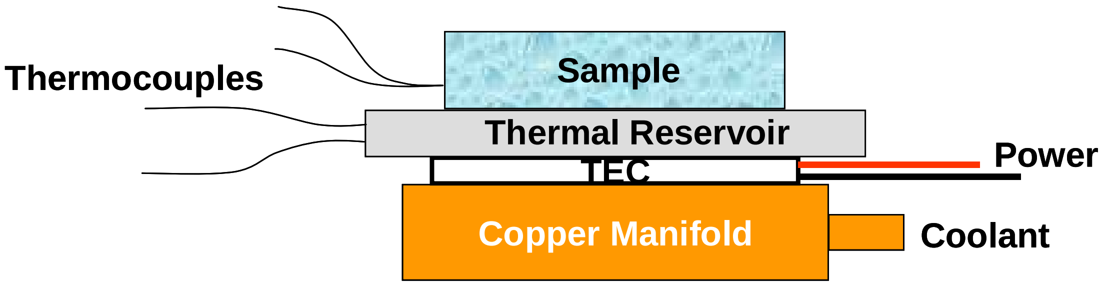

Figure 3.2. Heat transfer assembly including TEC for heat transfer from or to the sample through the thermal reservoir and copper manifold used to remove heat from the experiment

At a given set point temperature the sample dwelt for at least five minutes before subsequent imaging. Prior to imaging, the QD slide was illuminated for two minutes with a 150W quartz halogen lamp excitation light source which delivered approximately 40,000 foot candles of cold illumination (MI-150, Fiber-Lite). A blue additive filter, 500 nm short-pass excitation filter (C47-288, Edmund Optics, Barrington, NJ) was used with the light source to block the longer wavelengths. The fluorescence emission of the QD slides was recorded with a CCD camera (KP-F2A, Hitachi) equipped with 600 nm long-pass filter (Hoya R-600, Edmund Optics), to cut off the shorter wavelengths, Figure 3.3. In effect, this optical arrangement segregates the emission light whose wavelengths are longer than the excitation light and shorter than the camera filter-set. At each set point temperature, three to six images were taken, as well as an autofluoresced image. The recorded images were stored on a PC (Dell) with a Windows XP operating system (Microsoft, 2002) through a frame grabber card (PCI-1410, National Instrument, Austin, TX) for further analysis [100]. Acquisition software (NI-IMAQ, LabVIEW) capable of sampling 30 frames per second was used to acquire data. The program code is shown in Figures A.2-A.4.

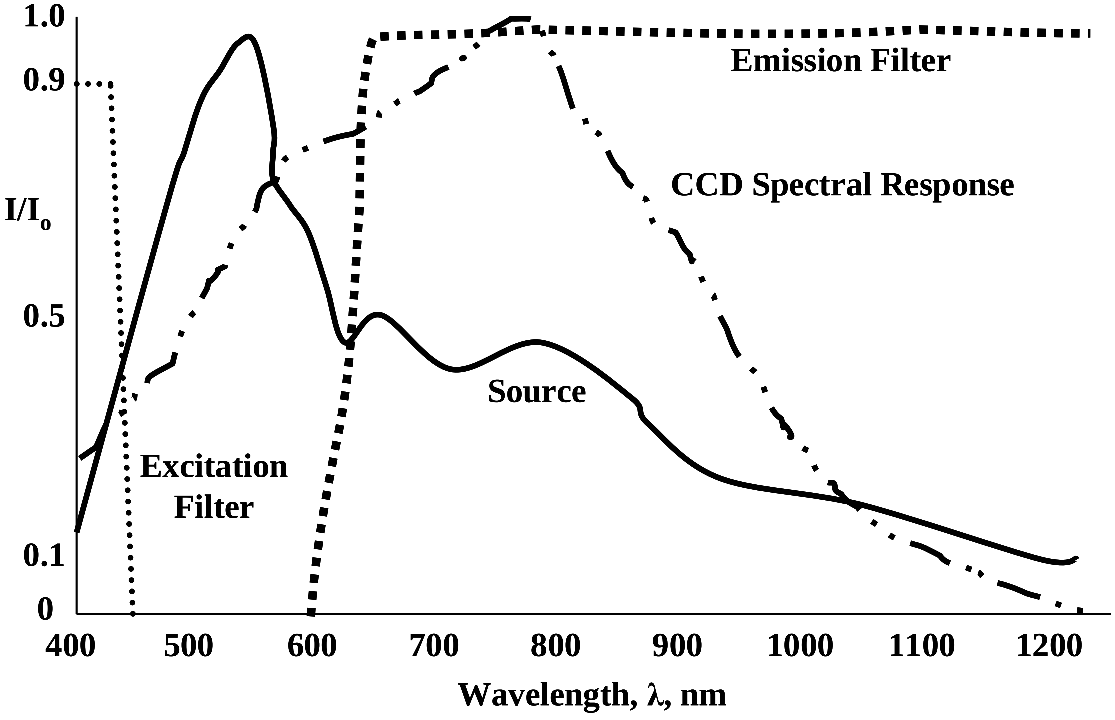

Figure 3.3. Spectral sensitivity of halogen excitation source, CCD and filter sets

3.3.3 Intensity Quantification

Fluorescent measurements were performed without room illumination to reduce noise. The acquired images were processed using image-processing programs (ImageJ, NIH and MATLAB, MathWorks) to quantify the fluorescence intensity, Figure A.5. The acquiring software was manually adjusted to capture the maximum range of intensity from the QD area. The height of the camera was recorded to determine the pixel density for later data reduction, Figure A.1. The intensity of each image was area-averaged to get a representative value of the intensity, and to smooth out the noise. The intensities of three images are averaged again to determine the value of intensity for a given temperature. The final intensity values, I(T), were normalized at a reference intensity, $I(T_{ref})$ of 40°C, the approximate human physiological temperature. The intensity temperature relationship was scaled by linear interpolation (4). The data reduction scheme to scale the output voltage is shown in (5) for an intensity of an 8-bit resolution camera.

$$T = \frac{I(T)}{I(T_{ref})} * \frac{(a + bT_{ref}) - a}{b} \tag{4}$$

$$\text{output voltage} = \frac{(\text{WRV} - \text{BRV}) * \text{intensity}}{255} + \text{BRV} \tag{5}$$

3.4 Results and Discussion

The thermometry system was designed to provide temperature control for both cryosurgical and hyperthermic environments. The TEC device was employed because it provides a robust and highly responsive temperature control mechanism for the sample size currently measured. The heat transfer capacity provided by the circulating system was initially designed to follow the set-point temperature used to drive the TEC. However is was found to be fully capable of removing heat for all work done between

20 and 70°C when it was set to dwell at 20°C throughout an experiment. The circulator needed only the pump to be operating, e.g. the heat exchanger portion of the circulator was not running. This was because of the low thermal mass of the sample, the relatively large reservoir capacity, and runtime of the experiment.

Imaging was adequately provided for by a NIR camera system which could output a frame rate capable of capturing images individually or continuously at frame rates that would capture the overall intensity variation with temperature for our work. The post-processing was aided by a dedicated frame-grabber board that seamlessly interfaced with the data acquisition software.

Temperature control of the TEC was performed manually through the temperature controller. The minimal amount of mass inertia in these experiments allowed the PID setup to be run with PI control only. The circulator was also run manually. Future programming can readily be automated by driving the temperature controller and circulator through RS-232 connectors available on both machines.

The data acquisition software program was developed in house using the LabVIEW programming language. The front end image of this control panel is shown in Figure A.5. This image acquisition program enabled the user to adjust light and dark threshold voltages using an 8-bit bandwidth. The single image mode allowed the user to set the frequency and number of images to be taken as a PNG file. Multiple frame sequences were saved as an AVI file with the frame rate and total run time set by the user. LabVIEW was chosen because this programming approach uses architecture that allows multiple queues. For our purposes this enabled temperature control and image acquisition commands to be handled concurrently. Also, functions made available from third-party hardware vendors allow LabVIEW to be easily incorporated into an existing file.

Image files were post-processed with ImageJ (NIH) and LabVIEW routines. An ImageJ macro was programmed to query different sections of an image and buffer the data until the total the number of images were processed. The buffer was then manually copied onto a spreadsheet program for further analyses. LabVIEW data reduction programs were used to process intensity variation with temperature over a period of time from AVI files. The operating panels are shown in Figure A.6 and Figure A.7. The program in Figure A.6 interrogates a line of pixels whose endpoints are chosen by the operator. Figure A.7 shows the operating panel of a program to measure the variation in intensity over time of an area whose dimensions and location are again selected by the operator.

Changes in the QD fluorescence emission intensity are presented in Figure 3.4. At 5°C, the lowest temperature imaged in this study, the QDs are shown to have strongest fluorescence emission, i.e. highest quantum yield. As the temperature is increased the emission intensity decreases, 41% by 70°C. This implies the plausiblity of detecting in vivo thermal features non-invasively using QDs. This method can be optimized by fine-tuning the peak emission to the NIR regime, 800-900 nm, where absorption and scattering by biological tissues are a minimum [91].

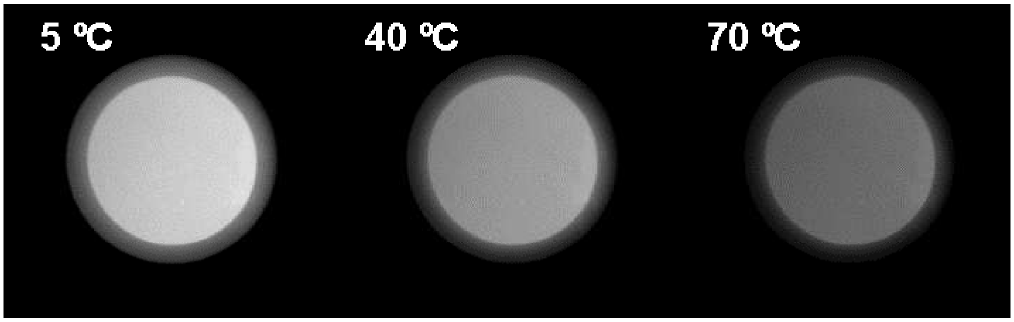

Figure 3.4. Illustration of the variation of QD fluorescence intensity with temperature for the reference film from Evident Technolgy

The intensity, normalized at 40°C, is plotted versus temperature and linearly curve-fitted in Figure 3.5. Hysteresis of fluorescence intensity during heat cycling of a fluorescent material is known, but no noticeable hysteresis of these QD's fluorescence emission was observed throughout the present characterization [92]. Further research is warranted to confirm this.

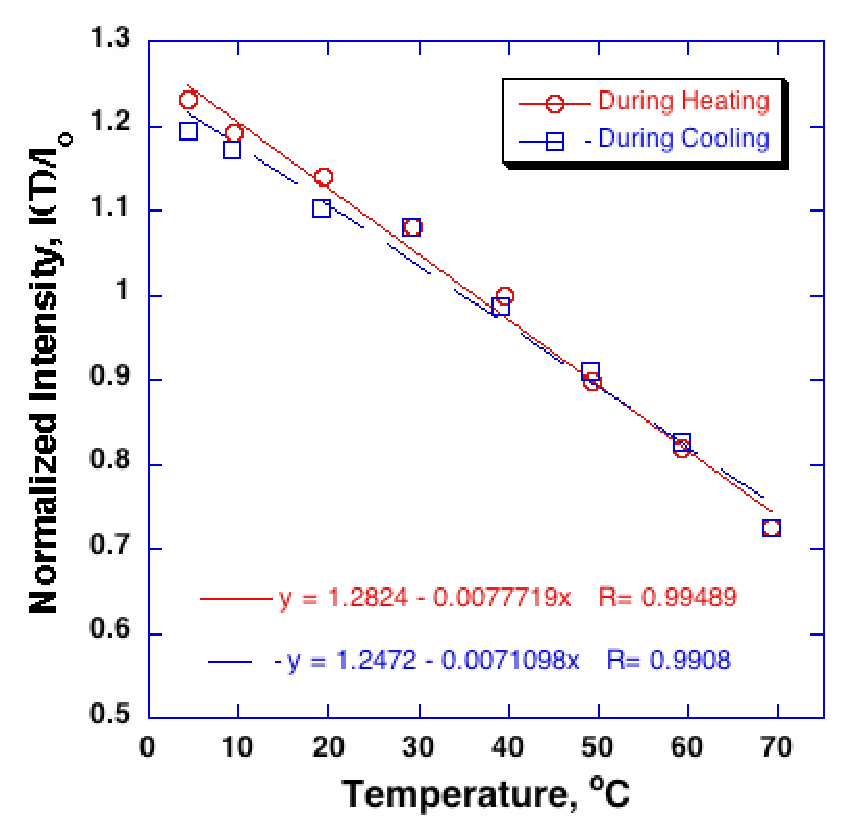

Figure 3.5. Linear interpolation of the intensity temperature curve during heating and cooling

3.5 Summary

The fluorescence emission intensity of the CdSe/ZnS core/shell QDs was measured using a thermal imaging system developed in-house. The emission intensity was linearly correlated to temperature between 5 and 70°C. These results imply great potential for a non-invasive imaging modality for both hyperthermic and cryogenic minimally invasive thermal surgery. This method can also be extended outside the medical imaging field, to measure temperature features in a wide variety of scientific and engineering applications given the proper application/introduction of QD.

CHAPTER 4

QUANTUM DOT EMBEDDED NANOPARTICLES

4.1 Introduction

The use of minimally invasive surgical techniques for the surgical management of tumors is increasing because of improved diagnostics. These surgical procedures include thermal therapy where localized heating is employed to destroy cancerous tissue. Yet, lack of real-time temperature information of the target tissue volume significantly hampers the efficacy of thermal therapies. Increased diagnostic capabilities now allow tumors to be detected at stages where the tumors are small at the time of therapy. Accurate intra-operative monitoring of the thermal lesion in these cases is critical because there is a greater surface to volume ratio, and thus, there is a greater proportion of healthy tissue at risk of collateral damage. Also, minimizing damage to adjacent tissue is imperative when major blood vessels, nerve bundles, or surrounding organs may be susceptible to thermal damage.

Recently the feasibility of QD used as a temperature transducer has been demonstrated [90]. Even given that the optical properties of QDs are superior to organic fluorophores, there are still limitations in their application to deep tissue imaging. Deep tissue imaging using QDs for volumetric temperature measurement requires a significant improvement in their quantum yield to be effective. The present study addresses this challenge by reporting on the development and characterization of nano-composite particles that exhibit temperature dependent fluorescence. These particles are called quantum dot-embedded, nano-composite particles (QDeNP). Our goal was to determine the functionality of these particles in deep tissue temperature monitoring.

The QD is a semiconductor material with high quantum yield, high photo-bleaching threshold, and narrow bandwidth fluorescence. This fluorescence can be red shifted by simply increasing the QDs' diameter. However, this approach can only be exploited within a narrow bandwidth because the band gap energy diminishes with increased diameter. This limitation is overcome with the introduction of the core/shell QD. The core/shell assembly allows fluorescence beyond the visual spectrum into the near infrared (NIR) which is more advantageous for tissue imaging [57-59]. QDs tailored for in vivo imaging fluoresce in the near infrared (NIR) where the absorption of biological tissues is the least [91, 93, 94]. Feasibility for in vivo imaging and cancer detection using NIR QDs has been successfully shown for QDs with core/shell structures containing a biocompatible polymer coating [37, 69, 95]. Aggregated QDs were fluoresced in the NIR to non-invasively show the location and scale of the target tissue.

A major limitation associated with QDs is that, because of their size only a small fraction of excitation light interacts with the crystal. Thus, a large molar concentration of QDs is required to cause enough fluorescence to be quantitatively measured. Also, the practical limit of penetration depth employing QD fluorescence is approximately one centimeter [74]. The quantum yield of core/shell QDs will require further development to operate as a fluorescent marker in thermal therapy for it to be effective beyond this one centimeter limit.

The present chapter will describe the temperature-dependent fluorescence characterization of a QDeNP. These particles were developed to extend the parameters of commercial QDs to enable deeper tissue imaging. Collaboration was undertaken with Dr. Choong-Un Kim's group in the Department of Material Science and Engineering at UT-Arlington to address this need. A custom assembly was designed to address the fluorescent intensity limitation of currently available QDs by synthesizing a nanocomposite particle with diffusively aggregated QDs embedded in it, as shown in Figure 4.1.

If successful, this design will overcome the penetration limit of current QD-based imaging technologies, result in higher quantum yield, longer in vivo fluorescence lifetime, and possibly do so with lower molar concentrations. Also, typical core/shell QDs have a red-shift in wavelength and lose photoluminescence as their size increases. The proposed QDeNPs particles are innovatively designed to overcome this barrier. Thus, a proposed nanocomposite particle, QDeNP, was developed which employed a novel manufacturing technique by aggregating QDs through a controlled precipitation process to increase fluorescence [96]. These nanocomposite particles were designed to have stronger emission in the NIR where biological tissues have the lowest absorbance [91].

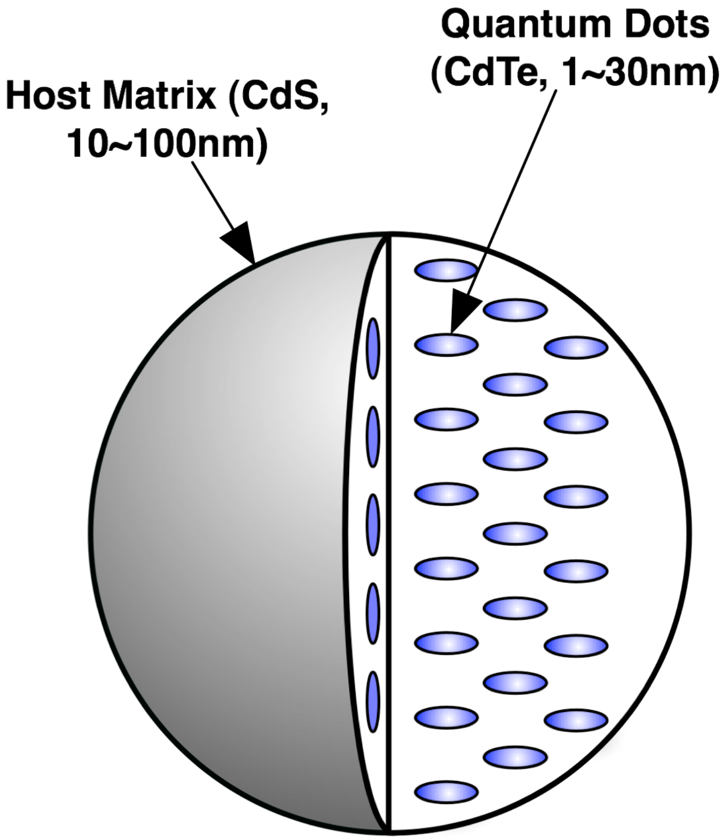

Figure 4.1. Schematic of QD-embedded nanoparticles

4.2 Materials and Methods

4.2.1 Fluorescence Characterization of Quantum Dot Embedded Nanoparticles

The fluorescence of QDeNP was visualized using a fluorescence microscope (BX51, Olympus) with a TexasRed filter cube (emission wavelength = 645 ± 75 nm), and imaged with a high resolution/sensitivity CCD camera (DP70, Olympus). The temperature-dependent fluorescent intensity was characterized by a thermal imaging system developed within our group, Figure 4.2.

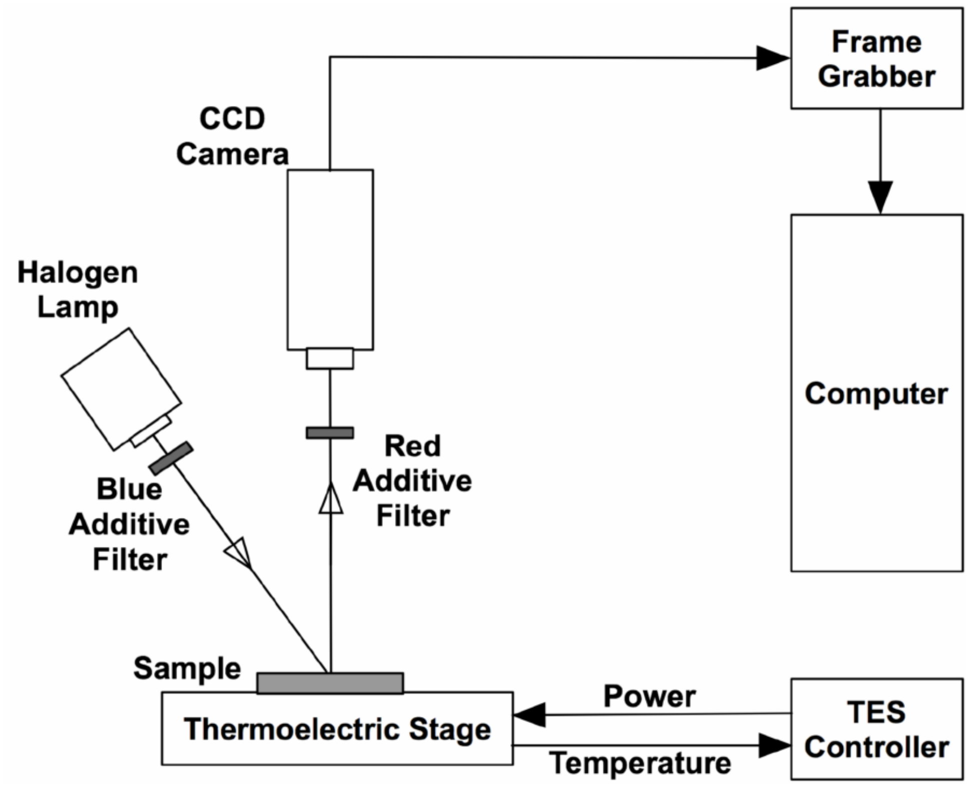

Figure 4.2. Schematic of the thermal imaging system

Temperature control of either sample, QD (CdSe/ZnS) or QDeNP, was provided by a single stage thermoelectric cooler (TEC) and temperature controller (SP5517-00L and SE5010 respectively, Marlow Ind.). The TEC was sandwiched between an aluminum plate and copper plenum with a dielectric paste (Arctic Silver, Visalia, CA) used to increase heat transfer between surfaces. A circulator bath (FP50-MC, Julabo) with propylene glycol as the working fluid through the copper plenum was used to provide heat removal. The thermal imaging system was initially set to 20°C and allowed to run for at least 30 minutes prior to imaging. A three-minute dwell at each set-point temperature allowed the sample to acclimate to the new temperature.

The sample baseline evaluation was of a Type II CdSe/ZnS, QD structure, embedded in a 60 µm thick clear polymer with a peak emission 620 ± 10 nm (Evident Technologies, Troy, NY). The composite was laminated in a microslide with a 15 mm diameter viewing area. The QDeNP sample was suspended in a solvent of either alcohol or water. It was evaporated onto a pre-cleaned microscope slide. Care was taken to ensure the slurry was evenly deposited and opaque against the background. Fluorescent measurements were performed without room illumination to reduce background noise.

The QDeNPs were fluoresced for two minutes with a 150 W quartz halogen lamp which delivered approximately 40,000 foot candles of cold illumination (MI-150, Fiber-Lite) via a 500 nm short-pass excitation filter (C47-288, Edmund Optics, Barrington, NJ). The sample was imaged with a near-infrared (NIR) 1/3” CCD (KP-F2A, Hitachi) equipped with a longpass filter with a cut-off wavelength of 583 nm (Hoya R-600, Edmund Optics). The fluorescence intensity of either sample was imaged at 10°C intervals from 20° to 70°C. The acquisition software was run on a PC (Dell) with a Windows XP operating system (Microsoft, 2002). A LabVIEW software program (NI-IMAQ) capable of sampling 30 frames per second was used to acquire data for image analysis. The software was manually adjusted to capture the maximum range of intensity from the QD area.

At each set-point temperature three images were captured as either PNG or AVI files using a frame grabber image acquisition board (PCI-1410, National Instrument, Austin, TX). The acquired images were processed using image-processing programs

(ImageJ, NIH and MATLAB, MathWorks) to quantify the fluorescence intensity where each image was interrogated with six 20×20 pixel windows, Figures 4.3 & 4.4. Each image was area-averaged to better represent the mean value of intensity. The intensities of the three averaged images were averaged again to determine the final value of intensity for a given temperature.

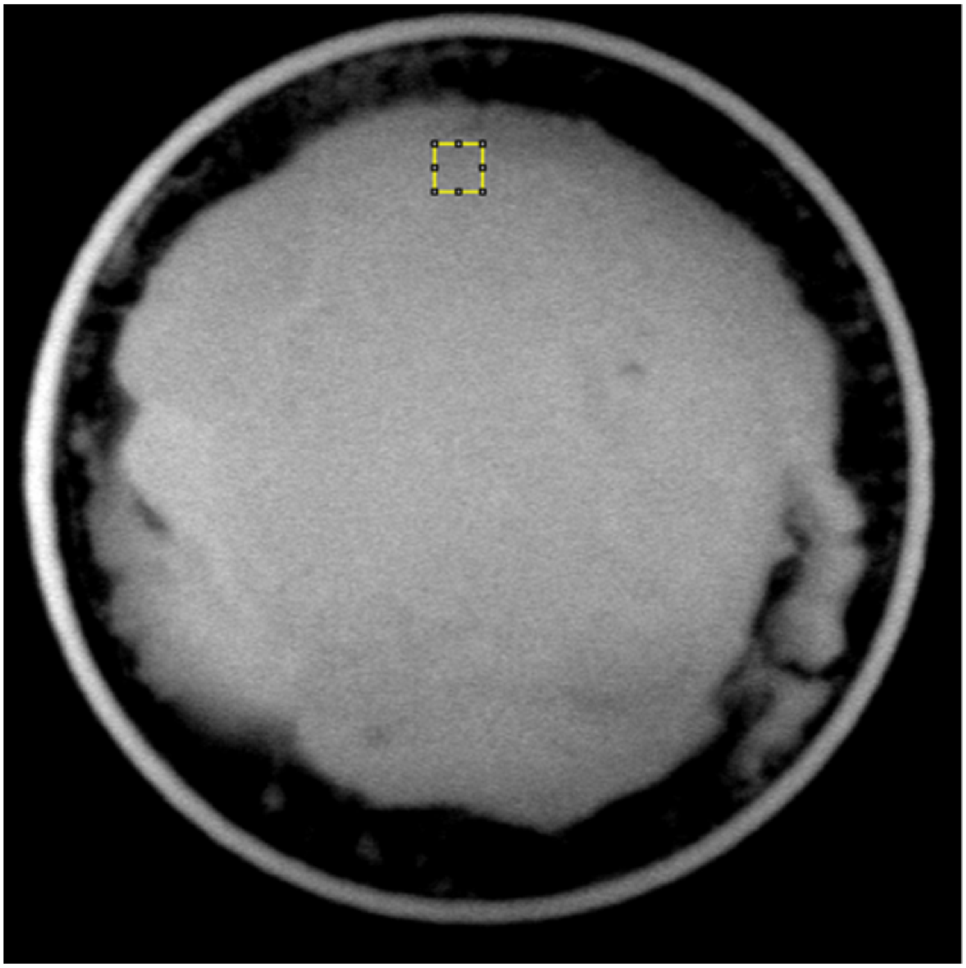

Figure 4.3. Illustration of a query area from ImageJ (NIH)

```
macro "Windowquery [115]" {
// BTPL @ UTA by Willard Hanson
// This macro will lay down numLoops of areas
// Each area will be query_width by query_height in dimension
// numTemps images will be made for each execution
var query_width = 20;
var query_height = 20;
var numTemps = 6;
var numLoops = 6;
totalArea = 0;

for (var j=0; j<numTemps; j++) {
    var xloc = 280;
    var yloc = 100;
    var yinc = 50;
    open();

    for (var i=0; i<numLoops; i++) {
        makeRectangle(xloc, yloc, query_width, query_height);
        run("Measure");
        yloc = yloc + yinc; }
        close();
}
}
```

Figure 4.4. Query area macro from ImageJ (NIH)

4.2.2 Synthesis of Quantum Dot Embedded Nano Particles

Our experiments measuring the fluorescent behavior of CdTe/CdS QD was facilitated by the QDeNPs development within the College of Engineering at The University of Texas at Arlington. These nanoparticles were synthesized by a controlled precipitation diffusion process developed by Dr. Choong-Un Kim at the Department of Material Science and Engineering [96]. For the present system, a CdS-rich alloy containing 16 mol% CdTe was prepared. The chosen amount of CdTe was within the maximum solid solubility limit in CdS, and thus formed a complete solid solution within the CdS. This proposed QDeNP will overcome the limitations of commercial QDs by incorporating a larger absorption area. Disk-shaped CdTe QDs, diameter approximately 6 nm, with a density of about 105 QD/μm^3 gave an appreciably higher QD density than that currently achievable with core/shell QDs. Scanning electron microscopy indicated the average NPs diameter to be approximately 100 nm.

4.3 Results and Discussion

Currently, deep tissue imaging requires either abundance of commercial QDs applied locally to cause measurable illumination above the background noise. Because of this limitation in the current state of the art, investigation of a stronger fluorescent probes was sought. A nanocomposite particle, QDeNP was developed for this purpose using a novel manufacturing technique where numerous QDs were aggregated through a controlled precipitation process increasing its local fluorescence [96]. Theoretically, the QDeNPs were designed to have considerably stronger emission in the NIR (650-900 nm) where biological tissues have the lowest absorbance [91]. Initial results showed a linear response similar to commercially available QDs. A nanocomposite particle was developed using a novel manufacturing technique which caused QDs to diffusively aggregate through a controlled precipitation process [96]. The fluorescence characteristics of a QDeNP with temperature are shown in Figure 4.6. Typical core/shell QDs incur decreased photoluminescence as their diameter is increased because the bandgap energy threshold is lowered due to lower quantum confinement. The QDeNPs however, did not lose photoluminescence when aggregated through their diffusion process and were seen to visibly fluoresce, Figure 4.5. Additionally, the fluorescence intensity of the QDeNPs was shown to decrease linearly with temperature similar to CdSe/ZnS core/shell QDs. The change in fluorescence intensity was measurable within the physiologic temperature range relevant to thermal therapy.

4.4 Summary

A new type of nanocomposite particle, QDeNP, was developed and characterized as a thermometry system. The developed particles have a temperature dependent fluorescence, but its dependency is not currently as strong as commercial core-shell QDs, 3% versus 41%, over 50°C. Further refinements should be performed to increase the temperature sensitivity. These would include increased QD density within the particle, the use of different QD and matrix materials, and increased production to yield a higher concentration QDeNP solution.

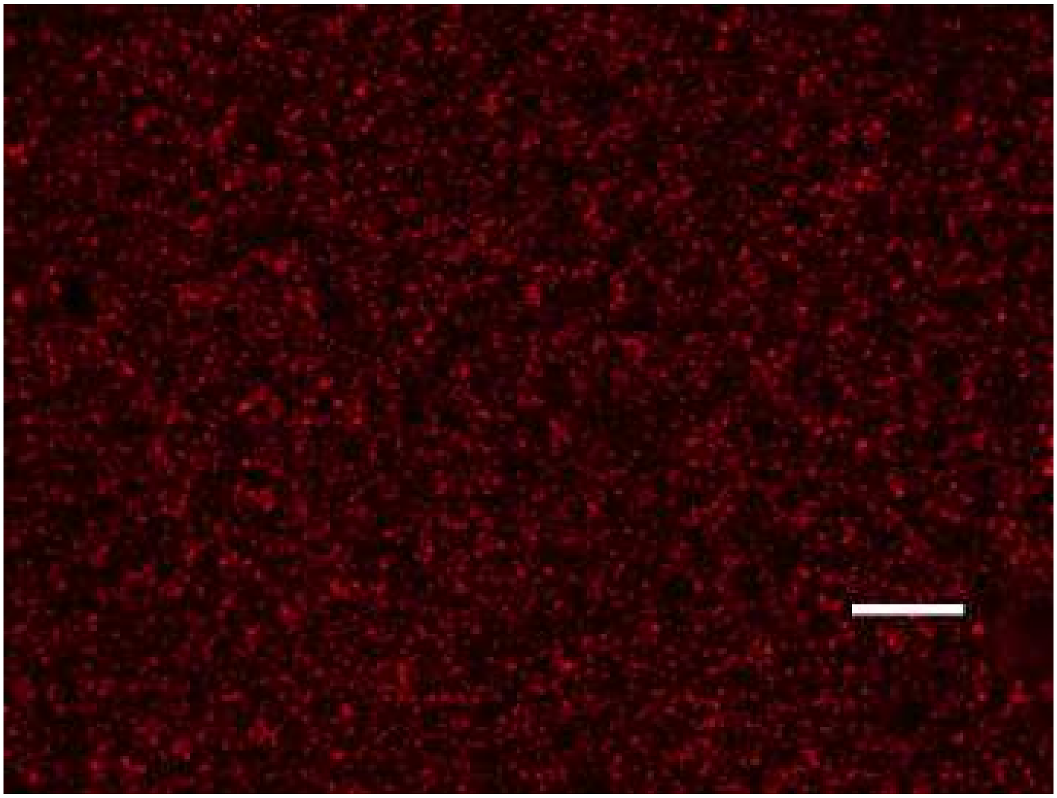

Figure 4.5. The fluorescence characteristics of QD-embedded NPs are shown as a fluorescence micrograph (scale bar = 50µm)

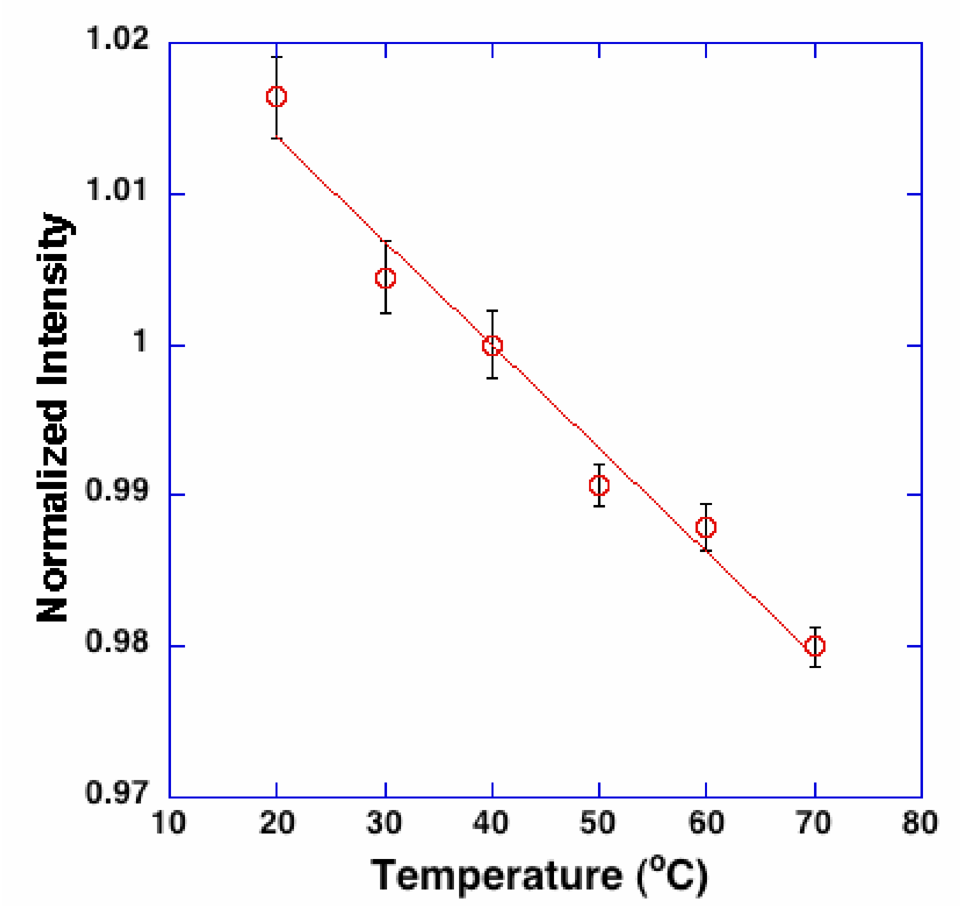

Figure 4.6. Temperature-dependent fluorescence intensity of QDeNP, n>3 for all points

CHAPTER 5

QUANTUM DOT WITH GOLD NANOSHELL MEDIATED THERAPY

5.1 Introduction

Advances in medical diagnostics are enabling tumors to be detected in their development where employing nonintrusive surgical techniques for tumor management is warranted. The limitations of open surgery to treat tumors at these dimensions have led to the growth of alternative therapies. Thermal therapy is one technique where thermal energy is applied to the malignant tissue to destroy it in situ by exposing the tissue to temperatures great enough to desiccate or otherwise cause necrosis. The inability to provide reliable intraoperative monitoring of the thermal lesion has always been the major impediment of any thermal application.

Current thermal monitoring methods include contact sensors, i.e. thermocouples, resistance temperature devices, thermistors or fiber optic probes. These point sensors are established applications but are only capable of providing information at a fixed location. Volumetric temperature sensors like diagnostic ultrasound, computational tomography, or magnetic resonance imaging require sophisticated algorithms for image reconstruction making them ineffective for monitoring the development of the thermal lesion during therapy. Thus, a thermometry system that could intraoperatively monitor the thermal lesion would support current thermal therapy and facilitate new innovation.

The gold nanoshell (GNS) is an example of nanoscale technology to allow thermal therapy to treat malignant tissue on the micrometer scale [97-99]. Still, the limiting step in thermal therapy is some means to provide dependable volumetric temperature information intraoperatively.

The feasibility of clinical application of QD-mediated intraoperative thermometry system is tested here. In this experiment the spatiotemporal temperature variation during gold nanoshell mediated heating will be estimated by measuring the fluorescent intensity of QDs. GNS are nanoparticles with a dielectric core of silicone and a gold shell. QNS can be used with low power heating applications, say a laser, when the applied frequency causes plasmon resonance [101]. This enables the GNSs to transfer heat to the target tissue. Cell death achieved by the indirect heating of GNS using NIR laser as has been demonstrated previously [97, 100]. Prior to heating, QDs were added to a petri dish containing human prostate cancer cells (PC-3) cultured to confluence. QDs in the culture medium fluoresce proportional to fluid temperature. Measuring local and temporal change of QD intensity will provide temperature change information during the GNS-mediated heating. After the experiments, the viability of the PC-3 was assessed to confirm the thermal injury.

5.2 Materials and Methods

35mm Petri dishes populated with human prostate cancer cells (PC-3) were incubated in 5% fetal bovine serum (FBS) supplemented growth media (Gibco) at 37°C and 5% CO2 and maintained using standard growth protocol to confluence. The control cells were removed from the incubator and exposed to ambient air for 5 minutes without GNS.

750 µL GNS, $3x10^9$ gold nanoshells/mL, and constructed of 110 ± 11 nm silica core with 10 nm gold shell, (Auroshell™ microparticles, Nanospectra Biosciences, Inc., Houston, TX) were used to transfer coherent NIR energy to the solution. 20µL CdSe/ZnS, 2µM, and constructed of 2.8 ± 2 nm CdSe core with 0.6 ± 0.3 nm ZnS shell (Qtracker® 655 non-targeted quantum dots, Invitrogen, Carlsbad, CA) were used to measure temperature [102]. These two constituents were mixed with 1230µL full growth media (Gibco) with 5% FBS supplements, vortexed at room temperature, and replaced the fluid maintaining the PC-3 cells.

The PC-3 laidened Petri dishes were then irradiated with a GaAlAs, NIR (805 nm ± 25 nm) laser with a power output of 0.5–15 W ± 10% (Diomed, Andover, MA) in the pulsed/interval mode with one second intervals and 90% duty cycle, i.e., 0.9 second pulse and 0.1 second interval, Figure A.8. The laser power density was set to 0.88 W/mm^2 using a power meter (Ophir, Logan, UT) and manually focused to an approximate 1.6mm diameter spot size to reproduce the results of earlier work [103] [104].

During irradiation the Petri dishes were illuminated with a 150 W quartz halogen lamp with 40,000 foot candles of cold illumination (MI-150, Fiber-Lite) using a 500 nm short-pass excitation filter (C47-288, Edmund Optics, Barrington, NJ). A NIR CCD camera (KP-F2A, Hitachi) equipped with a 600 nm long-pass filter (Hoya R-600, Edmund Optics) was used for imaging, Figure 5.1 and Figure A.9. Additionally, a hot mirror (Tiffen, Hauppauge, NY) was placed outside the emission filter to remove the longer wavelengths. This extra filter was used to provide shielding from long wavelength noise interference by forced imaging only in the visual spectrum, Figure 5.2. Images were captured as an AVI file at 30 fps using a frame grabber (PCI-1410, National Instruments) for further analysis [90]. The acquisition software was run on a PC (Dell) with a Windows XP operating system (Microsoft, 2002). A LabVIEW software program (NI-IMAQ) capable of sampling 30 frames per second was used to acquire data. The software was manually adjusted to capture the maximum range of intensity from the QD area.

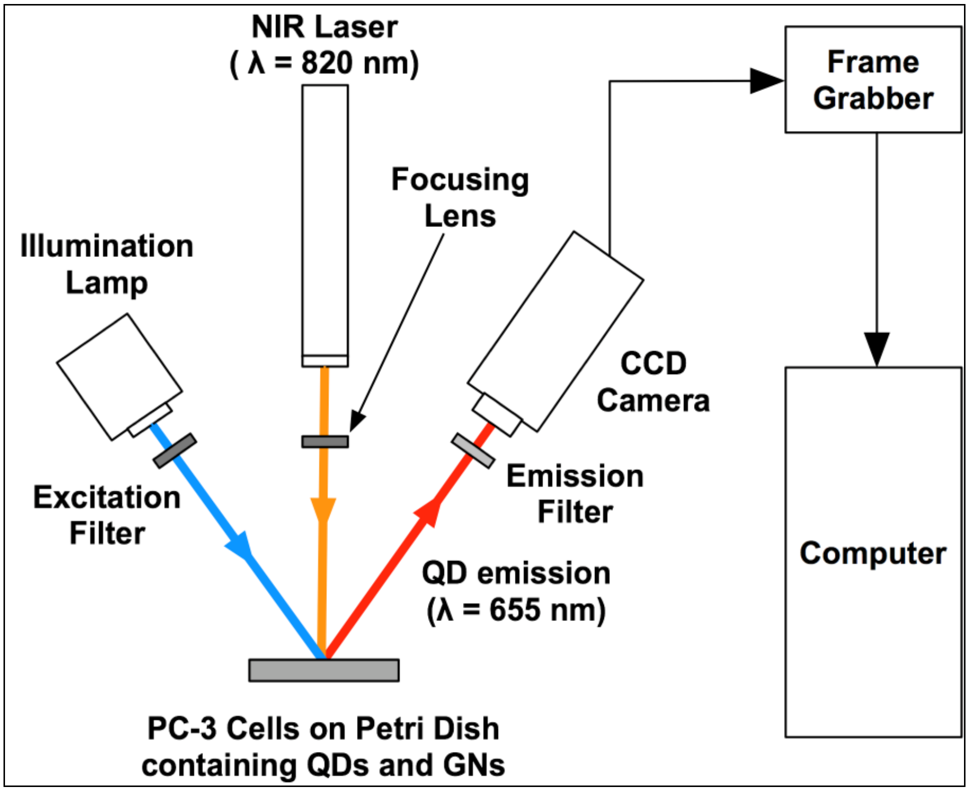

Figure 5.1. Schematic of experimental setup for QD-mediated thermal imaging during GNS-mediated thermal therapy

After the experiment, the dishes were washed with PBS and placed at 37°C and 5% CO_2 environment until the cell viability assay was to be performed. Because only viable cells can take up the fluorescent green dye the control and experimental groups were prepared with 2ml PBS and 1µL Calcein-AM fluorescence stain. The new solution was vortexed, and pipetted onto the Petri dishes, incubated for 15 minutes and imaged under bright field and FITC with a phase-contrast fluorescence microscope (Nikon, Melville, NY).

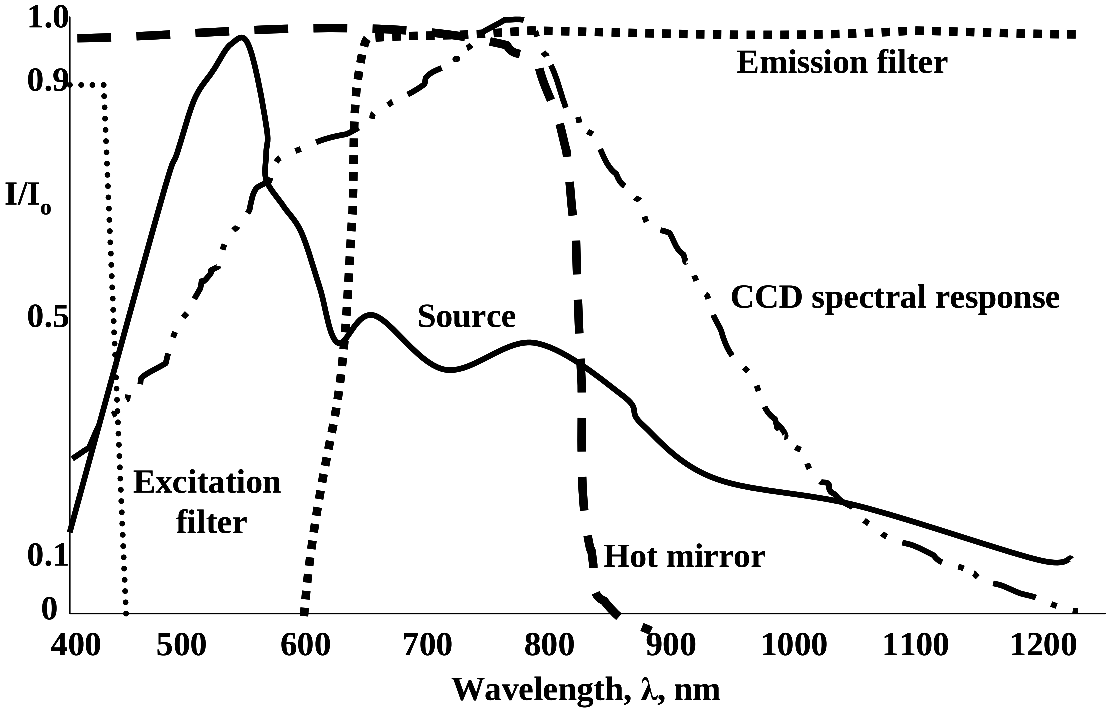

Figure 5.2. Spectral sensitivity response for fluorescence imaging

5.3 Results and Discussion

Figure 5.3 shows the radial progression of temperature change within the media, noted by the fluorescence intensity change. Frame one shows the QD fluorescence intensity of the media prior to NIR laser irradiation. In frame two, the dark region in the center at the focus shows evidence of NIR radiation being transferred from the laser to the QNS which in turn transfers its energy through the media by conduction. This media also contains QDs which absorb the energy and as a consequence fluoresce with less intensity, as shown. The third frame show the effects of the heated focus region undergoing a dramatic change in fluid density because of heat transfer to the fluid. Initially a large amount of fluid in the focal region is being heated but will remain motionless because its inertia will have to be overcome. The density change eventually causes the more buoyant media rise thus inducing toroidal bulk motion. The ring is a consequence of the initial perturbation of a large amount of heat at the focus causing the fluid to travel outward. Thus the ring is simply a large amount of the initial heated mass, including the QDs, of media now on the outside of the toroid. It shows up darker because of the viewing angle, which we see a section of, as the outside circumference of the expanding toriod. The last frame shows the media being heated further and spreading through the same toriodal bulk motion. But now, because of shearing between the heated media into the as yet still fluid, there is mixing occurring.

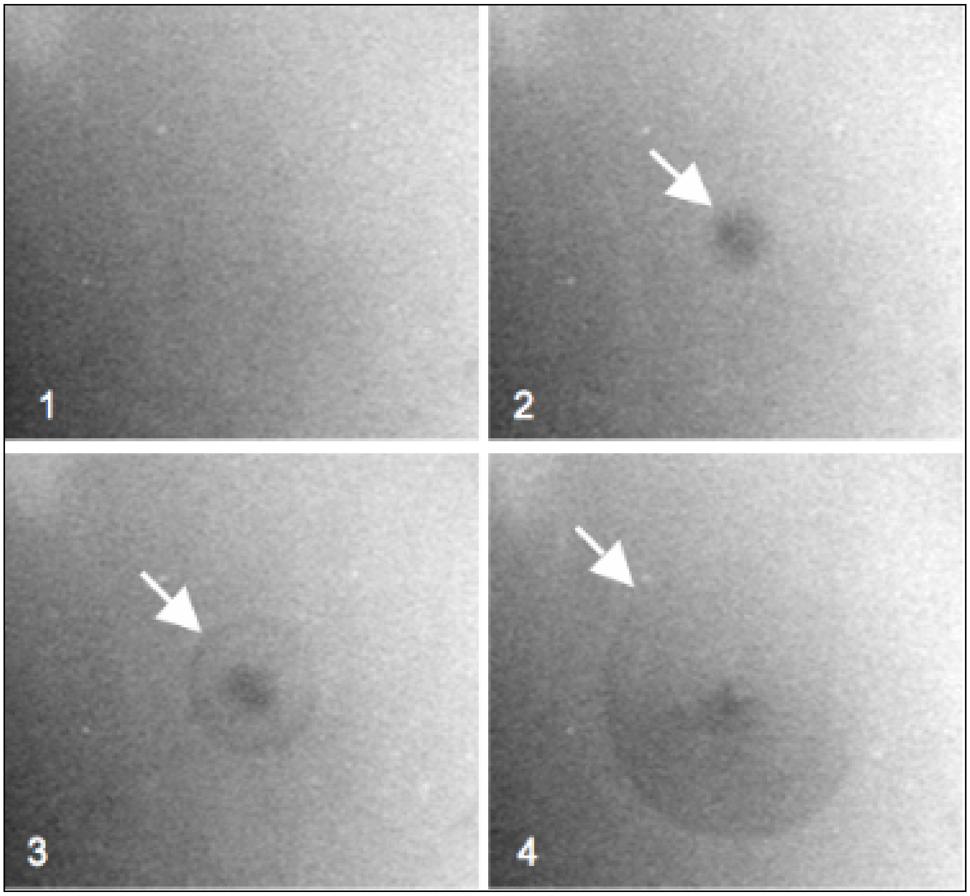

Figure 5.3. A sequence of QD fluorescence images during GNS-mediated thermal therapy. QD fluorescence at the spot where laser was focused decreases, and the dark spot grows in radial direction with time. This sequence of images show the intensity of the heating spot significantly decreases (image 2), and this region of decreased intensity grows in the radial direction with time (images 3 & 4), From [104]

Figure 5.4 shows the spatiotemporal temperature change along the centerline. The progression of temperature profiles over time shows the focus spot initially rising rapidly and reaching a maximum temperature well ahead of the media further out, radially. These temperature profiles also show a steep temperature gradient considered to be within the focal diameter of the laser beam. Generally the laser beam has a Gaussian profile which resembles the temperature profile shown. The heat transfer in the radial direction is shown to grow more gradually over time as might be expected because the volume being affected is growing nonlinearly because of the radial nature of problem.

Figure 5.5 shows micrographs of PC-3 cells after the GNS-mediated thermal treatment. The darkfield micrograph on the left shows the cells still morphologically intact after treatment. The fluorescence micrograph on the right show the surviving Calcien-AM stained cells. The demarcation of the ablation zone is well defined and estimated to be 653 ± 42 um (n = 9). This was approximately one third of the laser spot size (1.6 mm). This difference in thermal dose with increased radial distance is consistent with the general effects of a Gaussian laser profile where the treatment efficacy also decreases radially, as illustrated in the temperature profiles in Figure 5.4.

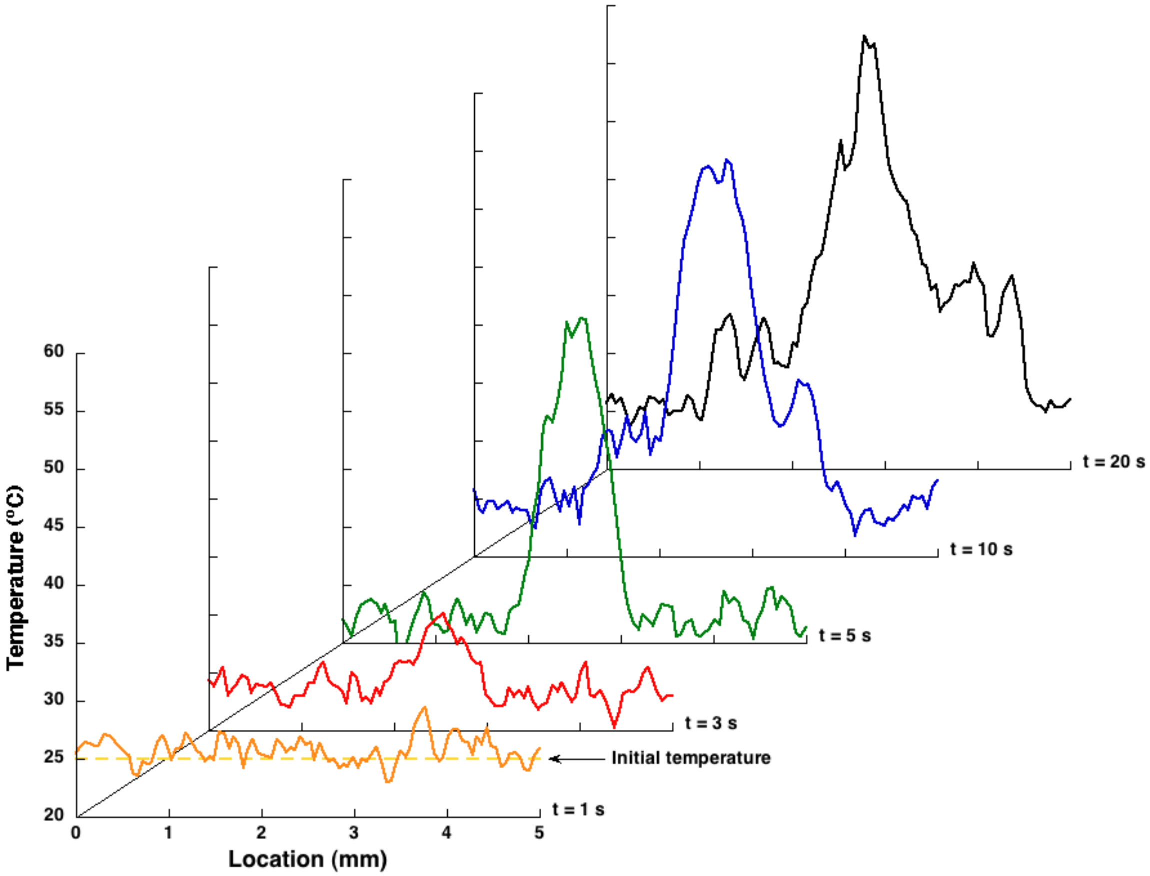

Figure 5.4. Spatiotemporal temperature during GNS-mediated heating. Temperature distributions measured with QD-mediated thermal imaging system during GNS-mediated thermal therapy. These profiles indicate that temperature rapidly reaches the maximum at the center of the irradiation zone. The temperature was evaluated with 15x15 interrogation windows

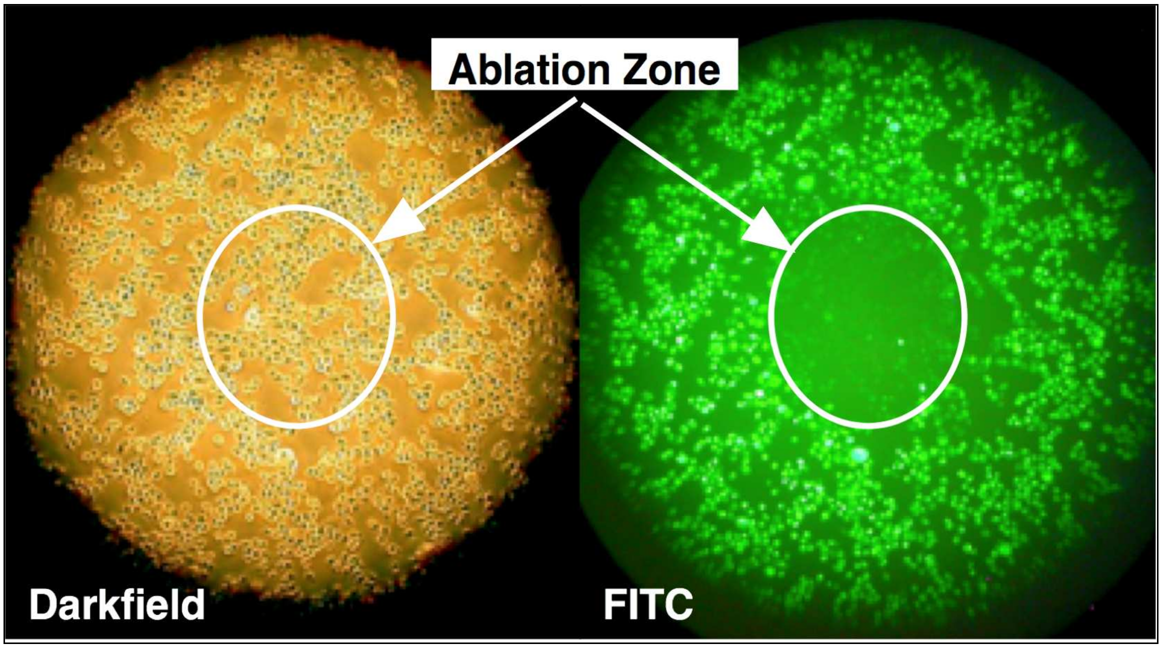

Figure 5.5. Darkfield and fluorescent micrographs of PC-3 cells after GNS-mediated heating. Darkfield micrograph shows cells still attached to the Petri dish. The fluorescence micrograph shows viable Calcien-AM stained cells around a destruction zone of 653 ± 42 μm (n=9) in diameter. The demarcation line of the ablation zone is well defined

Tumors applicable for thermal therapy are typically 1-2 cm in diameter with a surgical margin of at least 5 mm. Thus, the spatial resolution of a thermometry system should be capable of a few millimeters. QDs show great promise as an imaging probe for biological applications because of their strong narrow emission, wide absorption spectrum and long fluorescence lifetime. These results show that QDs will offer the temporal response and spatial resolution to adequately monitor the thermal lesion in an intraoperative thermometry system. Fluorescence emission measurements provide a rapid assessment of the temperature change of a heated volume in-vitro.

CHAPTER 6

TISSUE LIGHT INTERACTION

6.1 Introduction

As cancer diagnostics advance the tumor is often detected early enough to be destroyed *in situ* by localized heating. This heating can be performed using several means including laser, radio frequency, microwave or ultrasound. In spite of these many advancements in thermal therapy a major obstacle that still remains is the need for reliable intraoperative monitoring of the thermal lesion. Current monitoring techniques cannot provide reliable real-time information of the entire thermal lesion because of limited accuracy or accessibility.

The current technology for thermal lesion monitoring include point temperature sensors, i.e, thermocouples, RTDs, thermistors of fiber optics. A few imaging methods are currently used to monitor the thermal lesion, but their measurands are not thermal quantities nor temperatures. These include ultrasound, computerized and electrical impedance tomographies and magnetic resonance. These offer non-invasive volumetric measurements but have limited accuracy to monitor thermal lesion, require sophisticated algorithms for post image reconstruction and/or are generally not conducive for application in the surgical arena.

To tackle this problem, an intraoperative thermometry method is proposed which implements the natural behavior of the QD to fluorescence with intensity a strong function of temperature [90]. This process of QD-mediated fluorescence thermometry (QDFT) images the QDs through the target tissue where its fluorescence intensity is converted into temperature to assess the extent of tissue destruction. The efficacy of QDFT has been demonstrated by monitoring the spatiotemporal temperature of cellular destruction *in vitro* using gold nanoshell-mediated heating [104]. However, in vivo application of this technique requires quantitative understanding of the interaction between QD fluorescence and tissue.

In this chapter, it is hypothesized that the temperature dependency of QD fluorescence is measurable through tissue. This hypothesis was tested by experiment using tissue phantoms and by theoretical analysis considering tissue-light interaction. The results from this chapter will lay the groundwork for the application and development of the QDFT to in vivo and ultimately clinical settings.

6.2 Materials and Methods

6.2.1 Experimental Setup

An experiment implementing QDFT *in vitro* using a tissue phantom is shown in Figure 6.1. The details of the QDFT equipment and experimental setup, Figure 6.2, have been described previously in the chapter on QDMT [90]. In this study CdTe/ZnS (core/shell) wavelength, 614 ± 10 nm, 50% quantum yield (S- NB36-P34A; Evident Technologies, Troy NY) QD film was used. The QD film was sandwiched between two microscope slides with a 15 mm diameter viewing area. The QD film was placed on a heating manifold with a tissue phantom placed directly on top of the QD film. The temperature was controlled manually with a single stage thermoelectric cooler and each set-point dwelt for five minutes for heat soaking before imaging. After heat soaking the area was illuminated with a 150W halogen lamp equipped with a short pass filter, 500 nm cut-off wavelength, to cause the QDs to fluoresce. A black and white CCD camera with a long pass filter, 600 nm cut off wavelength, was used to image the attenuated fluorescence signal through the tissue sample. For each set-point temperature six images were taken at 10^{o}C intervals from 20^{o}C to 70^{o}C and stored on a PC for later analysis.

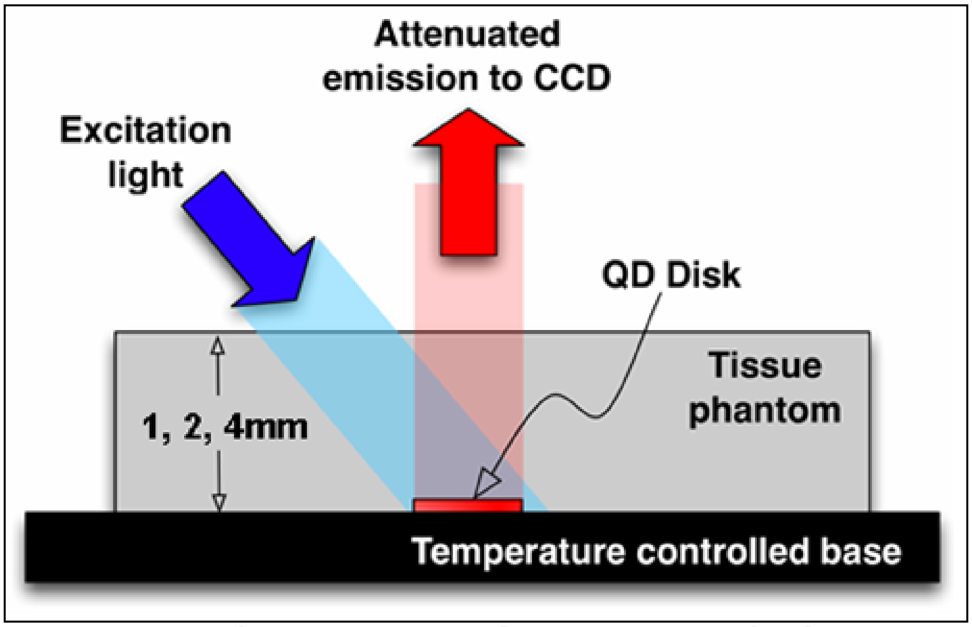

Figure 6.1. Tissue phantom experimental setup experimental and computational geometry of QDFT

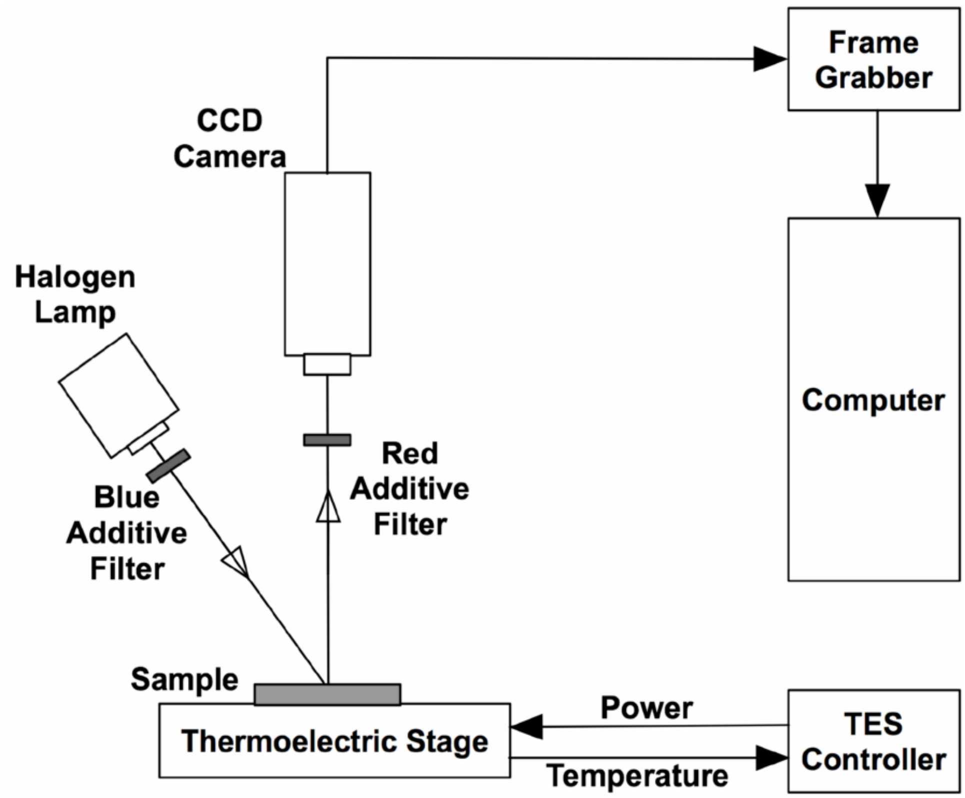

Figure 6.2. Tissue phantom experimental setup schematic

A tissue phantom was used to mimick the light scattering of human skin tissue. A gelatin based recipe was prepared by mixing gelatin powder (Sigma, Gelatin Type A, St. Louis, MO) with boiling water. The scattering agent was over the counter 1% milk added to the solution when it had cooled to 50°C. Formaldehyde was used to cause the gelatin to remain intact at higher temperatures by increasing the cross-linking within the gelatin. The mixture was poured into a mold and refrigerated at 4°C for approximately 10 minutes. The detailed recipe of tissue phantom is presented in Table B.1. The optical properties of this particular tissue phantom recipe were analyzed by Dr. Jae Kim at the University of California at Irvine. The resulting absorption and scattering coefficients were 0.4 and 0.004mm^{-1} respectively [121] [122], shown in Figure 6.3.

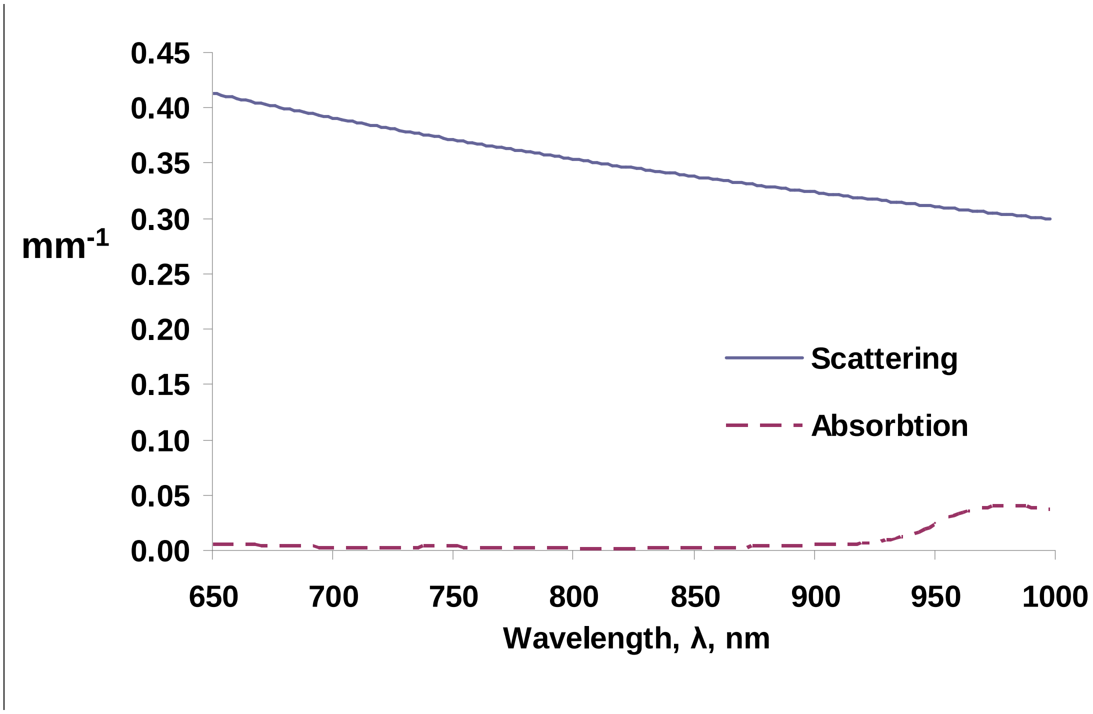

Figure 6.3. Optical properties of the gelatin-based tissue phantom

6.2.2 Computational Setup

Based on the optical properties of the gelatin tissue phantom, Figure 6.3, it was assumed the media could be properly modeled as a homogeneous translucent gray field. This meant, as a first order approximation, the absorption, μ_a, and scattering, μ_s, coefficients could be considered independent of wavelength [73]. Acknowledging the scattering dominant field and that it decreased monotonically with wavelength, it was also assumed the light interactions to be elastic and the phase function to be isotropic, e.g., independent of direction. Thus it was proposed to approximate the RTE with a DA.

The RTE describes the interaction of light transport through turbid media which incurs scattering and absorption. As a first order approximation, the attenuated fluorescence intensity by tissue phantom during QDFT, Figure 6.1, can be modeled as a steady state tissue light interaction with constant optical properties. The RTE can be written as (6), where I is directional spectral intensity, μ_a and μ_s are the absorption and scattering coefficients respectively and p is the scattering phase function [105]. Skin tissue is considered turbid media thus is scattering dominant. Thus the RTE can be reduced from six degrees of freedom to four in (7) by removing the dependence on the direction vector, $\bar{s}$ [106]. The resulting DA is the modified Helmholtz equation, Appendix C1. Where, Φ is photon density (W/mm^2), D is the diffusivity, $D = 1/3[\mu_a + (1-g)\mu_s]$, and g is the anisotropy parameter. Thus, the QD intensity at the modeled thermal lesion may be determined by solving (7) with the measured QD fluorescence intensity as a boundary condition.

$$\bar{s} \cdot \nabla I = -(\mu_a + \mu_s)I + \frac{(\mu_a + \mu_s)}{4\pi} \int_{4\pi} p(\bar{s}, \bar{s}')I(\bar{r}, \bar{s}', t)d\Omega' \qquad (6)$$

$$-\nabla \cdot (D\nabla\Phi) + \mu_a\Phi = 0 \qquad (7)$$

This DA is applied to a computational geometry shown in Figure 6.4, which is simulating the tissue phantom experiments. Figure 6.4 shows the side view of the computational domain with boundary conditions. At the side (x = +/- L), prescribed boundary conditions of zero intensity are imposed. A function, f(x), is imposed as a step function along the base centerline to represent the QD as the source of fluorescence intensity. The mixed boundary condition at the surface considers the diffusivity of the turbid media and mixed indices of refraction including the consequences of reflectivity between the two media [107].

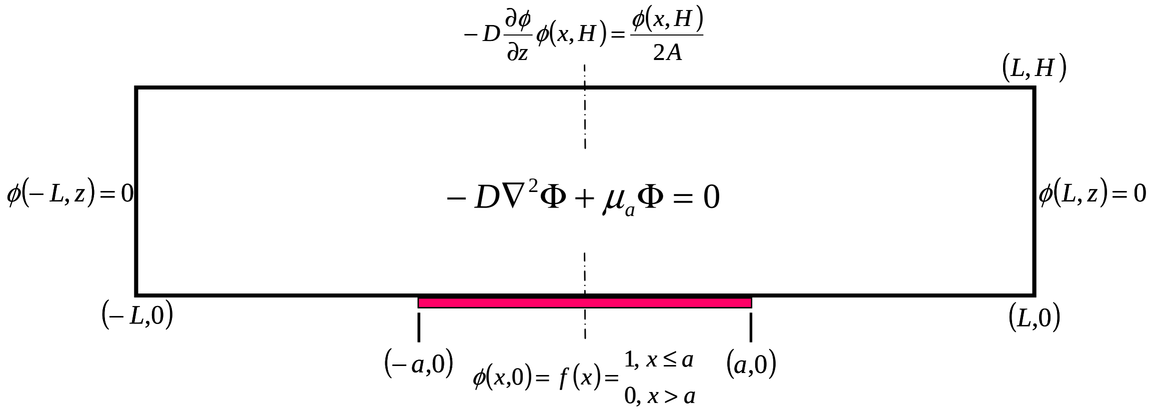

Figure 6.4. 2-D boundary value problem of tissue phantom fluorescence intensity attenuation with QD source imposed as a step boundary condition

The solution to this problem was obtained implementing numerical methods, Appendix C2. Critical to this approach was the transformation of the second order operator, $\int\nabla^2$, in the DA in Equation 2 from a strong to a weak form, Appendix C3.

A commercial finite element analysis package (COMSOL Multiphysics 3.5, Burlington, MA) was used to generate a numerical solution. The 3-D isometric finite element model (FEM) domain is shown in Figure 6.5.

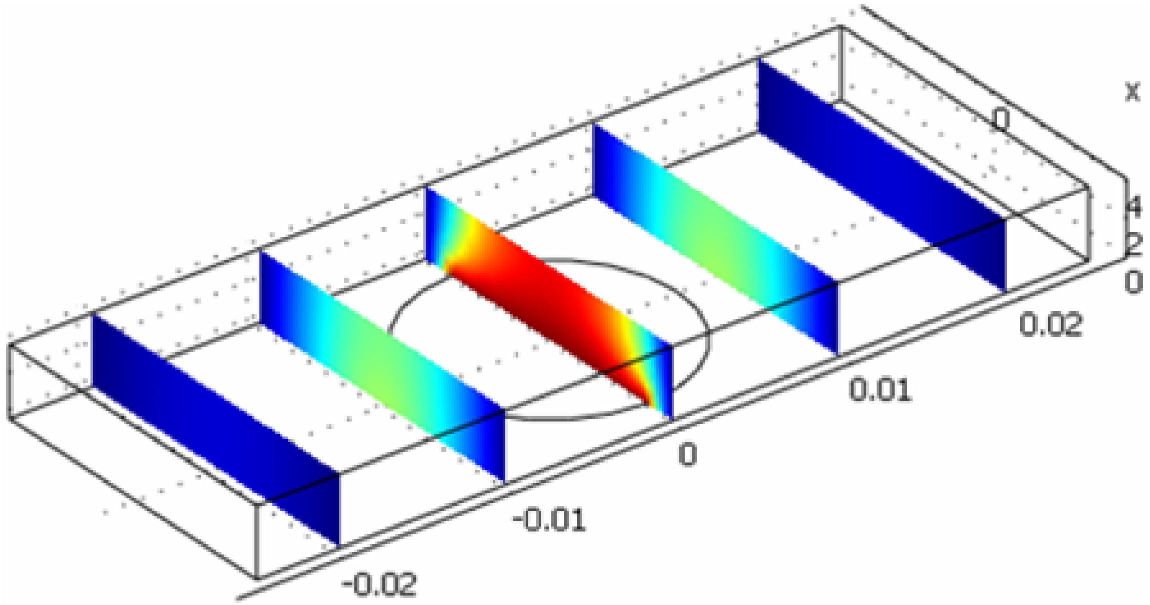

Figure 6.5. Tissue phantom model domain

Constructing a FEM model with Comsol the problem can be modeled with either with set of pre-defined governing equations used for most applicable physics applications or the user can write their own set of mathematical rules. For this model the modified Helmholtz problem was used as the governing equation. The working domain was drawn using CAD software available with the FEM package. For our work 2-D and 3-D geometries were modeled using triangular meshing and optimized by the software for the particular domain. The work was performed on a PC with the meshing density high enough for the program to take approximately 20 seconds to complete.

Once the meshing was finished a particular solver would be employed depending on the problem statement. COMSOL has several solvers suited for different applications. Our models were steady-state boundary value problems and were solved with the linear system solver, UMFPACK. Once the solution converged post-processing of the fluorescence intensity due to the QD source was modeled, by sectioning the volume to show a contour or by inputting coordinates to output a line plot. Post-processing to other modeling programs such as Matlab (MathWorks), Microsoft Excel or TECPLOT (Bellevue, WA) was also possible.

For the 3-D model a Matlab program was used to fit an appropriate order polynomial curve to the radial intensity profile obtained from experiment, Figure 6.6. The source profile, i.e., f(x), was imposed as a boundary condition in Figure 6.4.

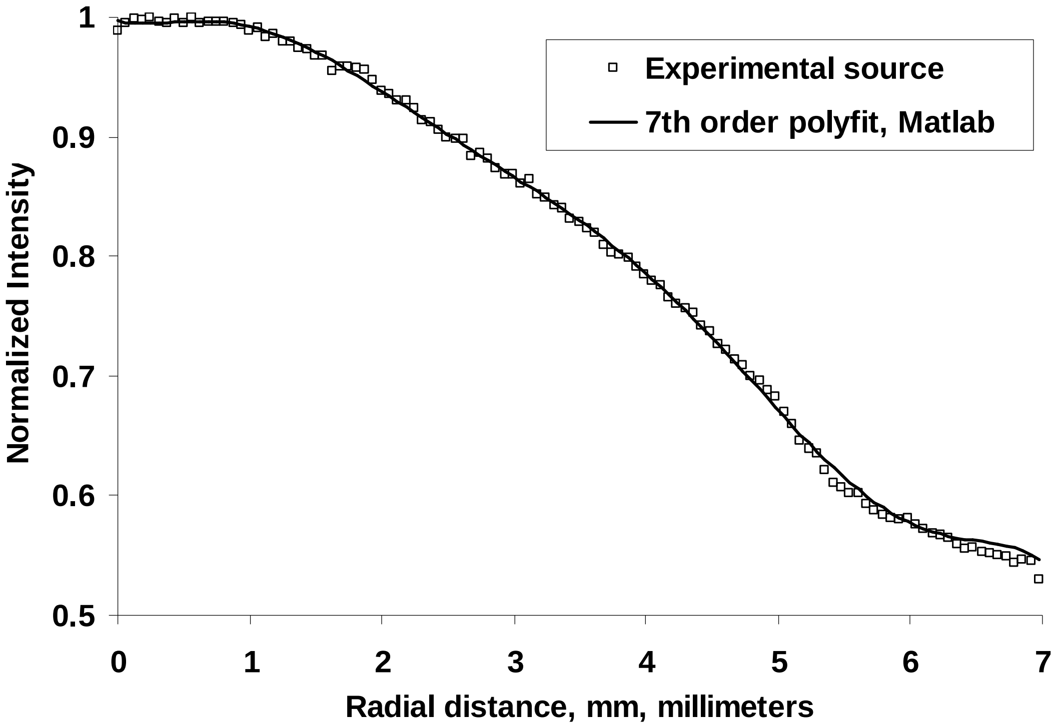

Figure 6.6. Polynomial fit of QD source profile in the radial direction

6.3 Results and Discussion

6.3.1 Experimental Results

Tissue phantoms were constructed of different thicknesses for several rounds of experiments. The images were analyzed to quantify the attenuated fluorescent intensity as a function of temperature and tissue thickness using NIH ImageJ. Each image was interrogated in six 10x10 pixel windows. Fluorescence photographs of the sample with varying tissue phantom thickness and temperature are illustrated in Figure 6.7. In any column, the increased temperature clearly shows a decrease in fluorescence intensity as reported in [90]. In any row, the presence or increase in thickness of a tissue phantom attenuates and diffuses the fluorescence intensity.

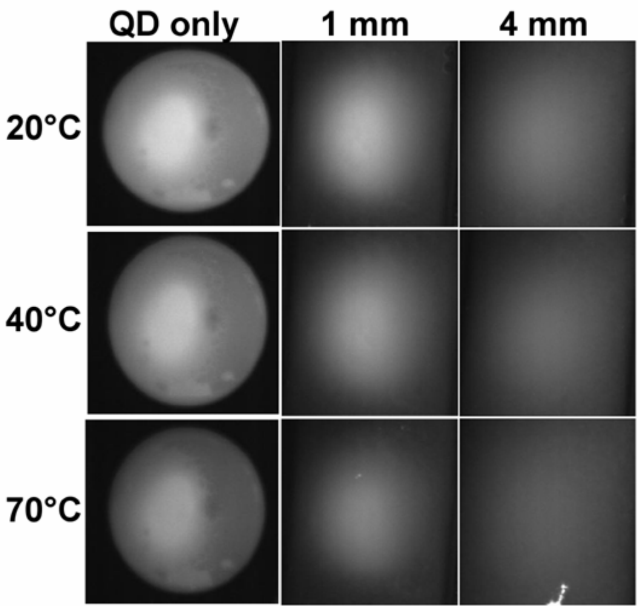

Figure 6.7. Photographs attenuated fluorescence with temperature and tissue phantom thicknesses of QD only group as a baseline, 1 and 4mm respectively [114]

The variation in spatial fluorescence intensity distributions at 20°C with tissue phantom thickness is shown in Figure 6.8. The fluorescence intensity is shown to decrease with the increase in tissue phantom thickness near its centerline. From Figure 6.3 this attenuation can be safely assumed to be caused by scattering within the tissue phantom. In the radial direction the intensity is augmented directly with the increase in tissue phantom thickness. This is attributed to scattered fluorescence from the surroundings as noted by the phase function evaluated by the term, $[(\mu_a + \mu_s)/4\pi]\int_{4\pi} p(\bar{s},\bar{s}')I(\bar{r},\bar{s}',t)d\Omega'$, in equation (1). These results are consistent with all tissue thickness variations and at all temperatures studied.

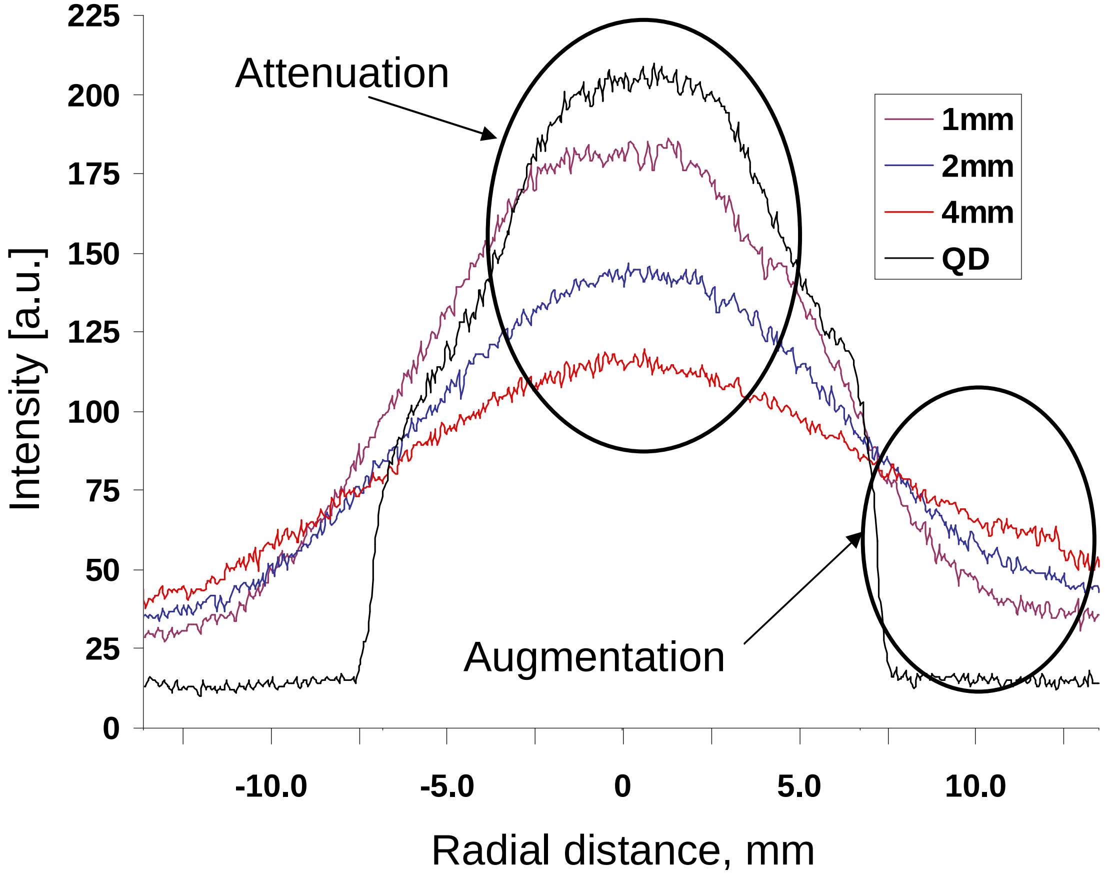

Figure 6.8. Radial QD fluorescence intensity distributions at 20°C [114]

Tissue-light interaction effects on QD intensity with several tissue thicknesses are correlated against temperature in Figure 6.9. The intensity was quantified by averaging a 10×10 pixel interrogated area near the center of the QD fluorescent image. Across the narrow bandwidth of hyperthermia surgical application the intensity-temperature relationship is nearly linear. Although the rate of change of intensity decreases inversely with tissue phantom thickness there is implication that QDFT is feasible, even with scattering and absorption, if the tissue thickness is known. It is typical to usually know the approximate depth of tumor from diagnostic imaging. Additionally, within the time frame between diagnosis and thermal surgery there should be a relatively minimal change in tumor growth. Thus, the application of QDF in vivo may provide spatiotemporal feedback of the extent of thermal destruction during treatment.

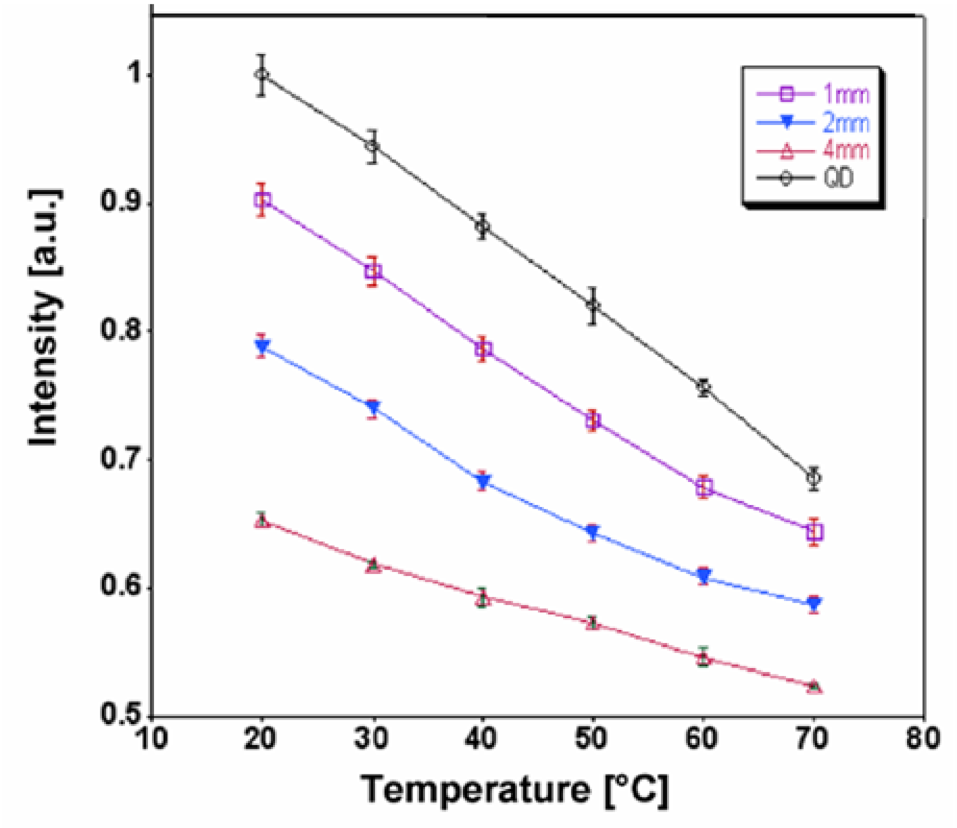

Figure 6.9. Tissue-light interaction on QD fluorescence intensity attenuation with temperature [114]

6.3.2 Computational Results

The theoretical characterization on the effects of tissue light interaction using QD thermometry was also studied. Tissue thickness effects were examined using the DA to describe the phenomenon within a scattering dominant gelatin tissue phantom.

Contour plots showing the fluorescence intensity at 4mm thickness and with prescribed zero fluorescence and constant fluorescence boundary conditions on the base are shown in Figures 6.10 and 6.11, respectively. These contours show the fluorescence intensity under steady-state conditions and with the influence of surface reflectivity caused by mixed indices of refraction. The contour plot with a zero temperature imposed, Figure 6.10, illustrates the surface intensity profile when none of the QD fluorescence back scattered onto the base is allowed to further interact with the tissue phantom. Figure 6.11 shows how a constant fluorescence boundary condition on the base causes all of light interacting with it to be reflected back into the tissue where it can further interact with the media. In either case, light reaching the side walls was lost to the prescribed zero fluorescence boundary condition imposed there.

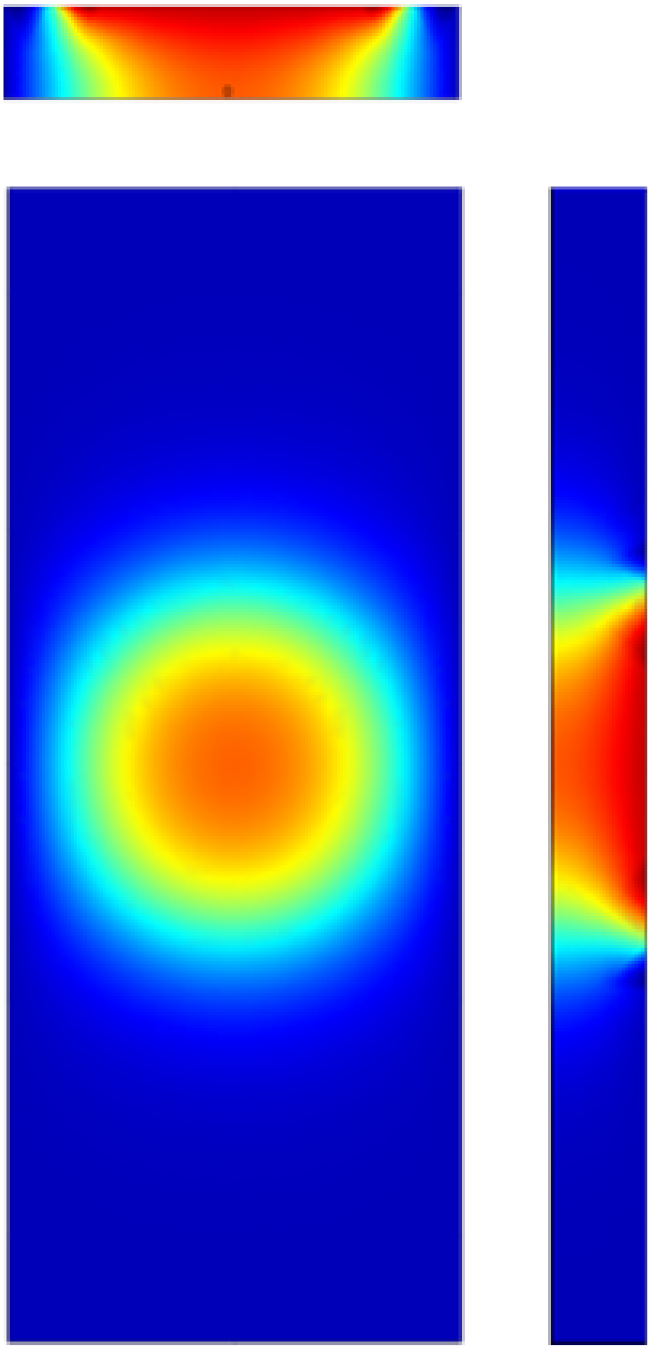

Figure 6.10. Simulated tissue-light interaction from QD fluorescence intensity through a 4mm-thick gelatin tissue phantom. A zero intensity, $\Phi = 0$, was imposed on the base outside of the circular source

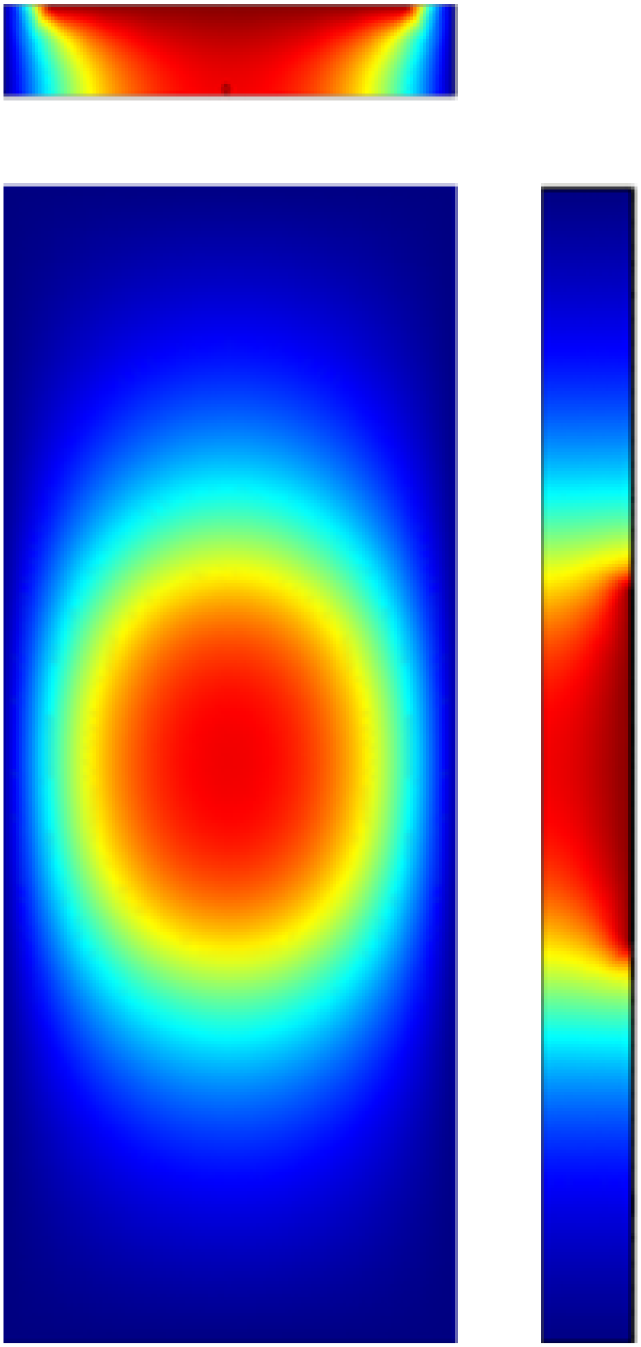

Figure 6.11. Simulated tissue-light interaction from QD fluorescence intensity through a 4mm-thick, gelatin tissue phantom. An imposed constant fluorescence condition, dΦ/dz = 0, was imposed on the base outside of the circular source

Line plots comparing the experimental and numerical fluorescence intensity attenuation at 2.5mm and 4mm thicknesses, respectively, are shown in Figures 6.12 and 6.13. In either plot the experimental result is shown as a solid line, the dashed line is the zero fluorescence and the dotted line is the constant fluorescence condition. These plots show the fluorescence intensity under steady-state conditions and similar domain constraints as the previous contour plots. Although the experiment has been normalized to the maximum value along the centerline, its shape better follows the profile exhibited by the prescribed zero intensity boundary condition.

There are several possibilities for these differences. The first may be in the inaccuracy of optical property measurements and the variation of optical properties with temperature. The total mean free path characterizing the optics for the computational tissue model was 2.5mm. This is at or near the limit of application for these tissue phantom experiments. Also, near the source the DA will give erroneous results [123] [108]. A possible cause for this may be that the term accounting for the divergence from source in the RTE is not present in the DA [109].

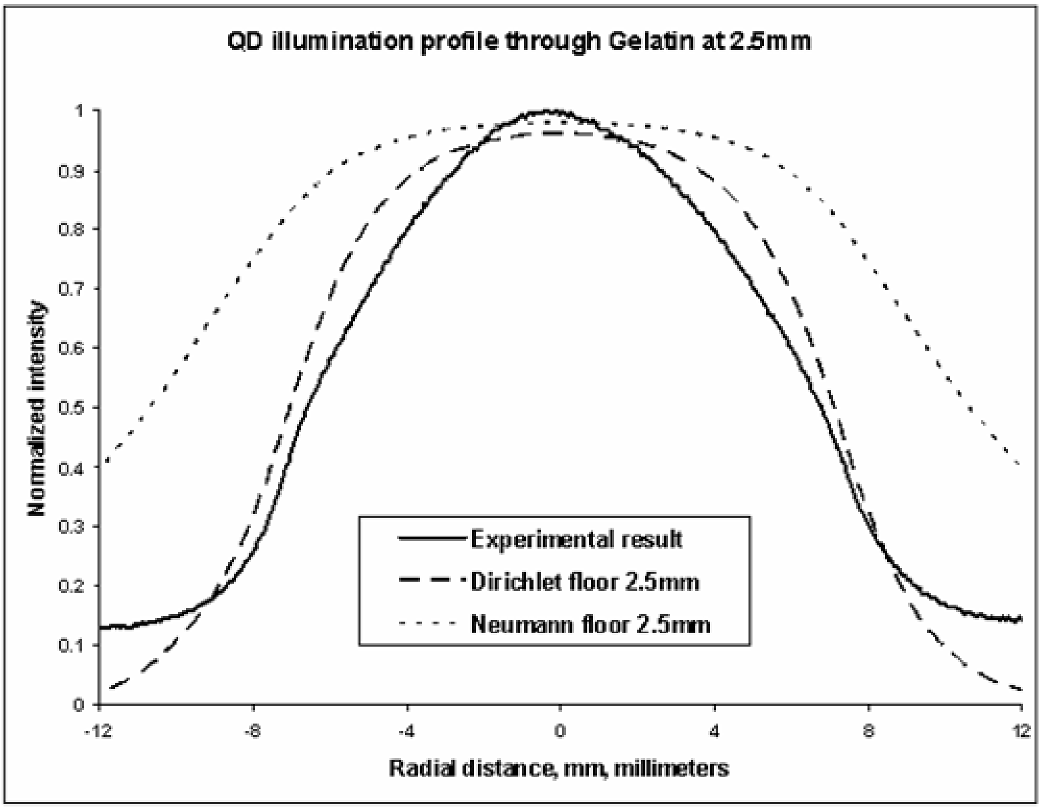

Figure 6.12. Comparison of experimental and numerical tissue-light interactions on QD fluorescence intensity attenuation with tissue phantom thickness at 2.5 mm

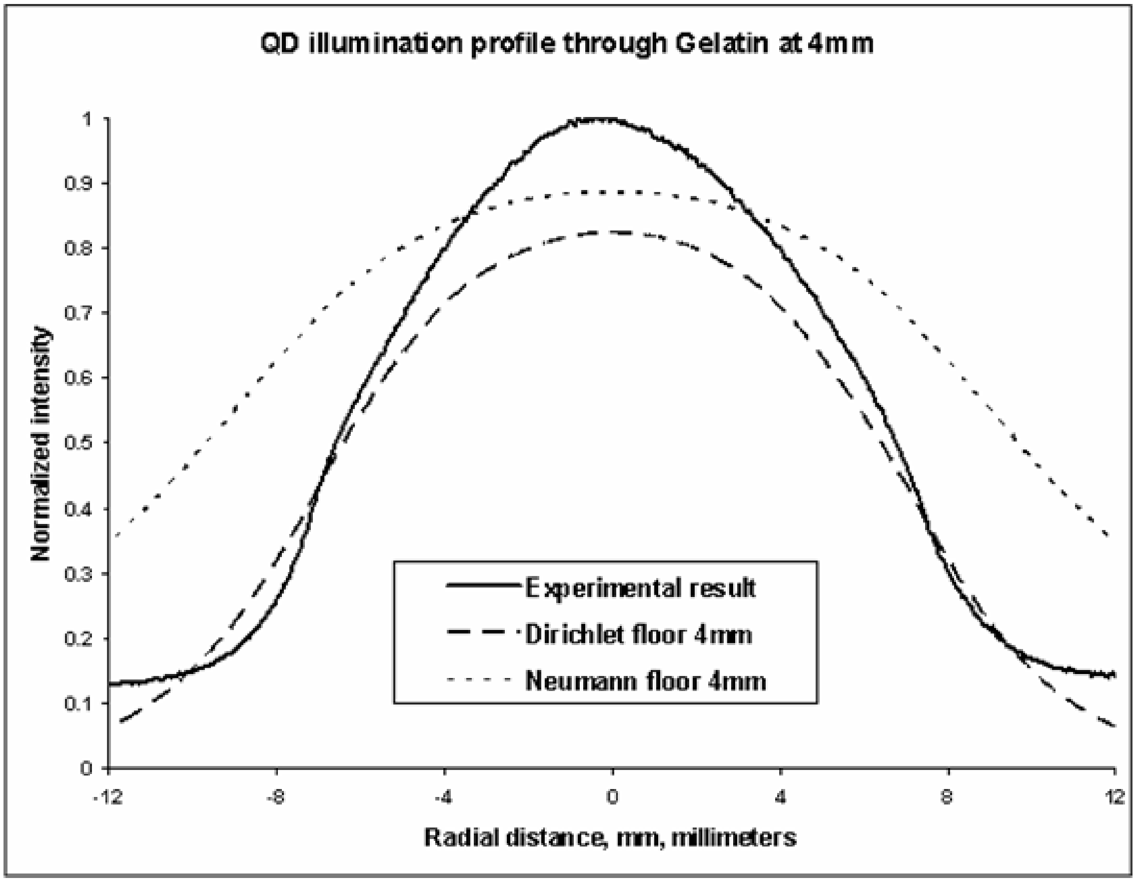

Figure 6.13. Comparison of experimental and numerical tissue-light interactions on QD fluorescence intensity attenuation with tissue phantom thickness at 4.0 mm

6.4 Conclusion and Future Work

The effects of tissue-light interaction on QDFT were characterized both experimentally and theoretically by testing a hypothesis that the temperature dependency of QD fluorescence was still measurable through tissue. The results confirmed the hypothesis and suggested that the DA of the tissue-light interaction describe the interaction reasonably well. Further refinement of the model and accurate tissue optical properties needs to be performed for more improved predictions.

Future studies to move this work forward will seek development of an algorithm to inversely solve to this DA problem. This inverse diffusion algorithm will be integrated into the imaging system for real-time temperature monitoring. This work will set forth, characterizing the intensity profile, assuming an isotropically scattering medium. The conjugate gradient method is one of several standard algorithms that uses a regularization method to minimize the objective function [110]. The basic premise of this procedure is to measure the general direction of descent by measuring the negative directional gradient at successive iterations. This procedure would solve the DA, i.e. the approximation of the RTE in this case, as a direct forward problem for intensity [temperature]. Next, the inverse problem would be solved form the same general problem with the unknowns being the source and intensity values from actual measurements to be the known independent variables. The difference between the measured intensity and that estimated from the solution of the forward problem is then minimized iteratively by differentiating the objective function, (8), with an appropriate stopping criterion. Where, $Z(\mu)$ is the measured intensity and $I(\tau_0, \mu; P)$ is the estimated intensity value.

$$\int_0^1 [I(\tau_0, \mu; P) - Z(\mu)]^2 \, d\mu \qquad (8)$$

CHAPTER 7

CONCLUSION

Minimally invasive thermal therapy destroys malignant tumors in situ by creating a localized thermal lesion. Its overall efficacy is compromised by the possibility of incomplete tumor destruction near the tumor periphery, which could pose a risk for the disease to reoccur. To address this issue intraoperative monitoring of the tissue lesion is essential to ensure complete tumor destruction. Since the thermal destruction of tissue is affected by local tissue temperature and heating duration, the temperature distribution around the targeted tumor should be provided in real-time.

Several techniques are currently being used to monitoring tissue temperature during thermal surgery. Point measurements use invasive devices such as fiber optic probes or thermocouples. Dagnostic ultrasound, computerized tomography, or magnetic resonance thermography are noninvasive methods which measure tissue temperature secondarily. Noninvasive methods require intensive image processing, employ high doses of radiation, or magnetization, or have poor image quality and are thus are not conducive for real-time application for surgery.

In this context, temperature-dependent QD semiconductor nanoparticles enable a new imaging modality for monitoring tissue temperature during thermal therapy. A QD thermometry system is envisioned, whose emission wavelength is optimized to fluoresce in the red to NIR spectrum, where the scattering by the surrounding tissue is a minimum. This would allow tissue temperature to be spatiotemporally visualized. The primary objective of this study was to develop a new thermometry system using QDs as temperature probes and to demonstrate its feasibility for the intraoperative monitoring of the thermal lesion.

A prototype thermal imaging system was developed to research the fluorescence characteristics of two types of CdSe/ZnS core/shell QDs within the temperature range relevant to hyperthermic therapy (5 to 70°C). It was found that there was a nearly linear relationship of fluorescence intensity with temperature. The changes in QD fluorescence emission were quantified by measuring the average fluorescence intensity with an 8-bit commercial NIR imaging system. The QDs were found to fluoresce the strongest, i.e., have greatest quantum yield, at the lowest experimental temperature. The fluorescence intensity decreased linearly with increased temperature in the hyperthermic temperature regime. These results imply that the thermal features of specific tissue could be detected non-invasively using QDs optimally tuned to the NIR regime.

Within the hyperthermic temperature regime, normalized QD fluorescence intensity was plotted versus temperature and linearly curve-fitted showing no noticeable hysteresis. These results imply the potential as a non-invasive imaging technique for minimally invasive surgeries including both hyperthermic and cryogenic temperatures. It is hypothesized that this thermometry system could also be used to measure nanoscale temperature features in a wide variety of other scientific and engineering applications.

The commercial core/shell type QDs studied were capable of illuminating through a few millimeters when used as fluorescent probes in turbid media such as tissue. A stronger fluorescence probe would enable deeper tissue imaging, improving the efficacy of the proposed thermometry system. In this context, a new nano-composite material was developed in collaboration with Dr. Kim in the Materials Science Department at UT-Arlington. This new nano-composite material is a quantum dot embedded nanoparticle assembly (QDeNP) where CdTe crystals were diffusively aggregated to an average 6 nm in diameter in a host CdS matrix 100 nm in diameter. This process yielded QD density approximately 10^5 particles/μm^3, which is significantly higher than any currently available conventional QDs. In contrast to conventional QD assemblies QDeNPs did not incur a wavelength shift with increased diameter. The QDeNPs fluorescence intensity also decreased linearly with temperature relevant to thermal therapy similar to the commercial QDs studied. The magnitude and temperature sensitivity of the QDeNPs was less than that of the core/shell QDs studied.

As part of this dissertation research the feasibility of QD-mediate thermometry was demonstrated to quantify in vitro cellular destruction by measuring QD fluorescence spatiotemporally during heating. In collaborative research with Dr. Cadeddu in the Department of Urology at UT Southwestern Medical Center, human prostate cancer cells (PC-3) were heated using gold nanoshell (GNS) mediated laser therapy. The cellular destruction was estimated by measuring the fluorescence of preadministrated CdSe/ZnS core/shell QDs in the growth media. Fluorescence imaging revealed two distinct heating regions. The first region, near the laser focus, showed the intensity to decrease rapidly reaching a minimum where it remained relatively constant throughout the remainder of the experiment. This implied direct GNS-mediated heating by the laser with a maximum local temperature with a steep temperature gradient at the laser focus. The secondary region was annular region that grew in size while its intensity slowly decreased. This implied that heat transfer induced by the GNS was being transported in the radial direction. Fluorescent micrographs of human prostate cancer cells (PC-3) cells after the GNS-mediated thermal treatment show a sharp delineation of cell viability at 650 ± 42 μm diameter (n = 9) in the treatment group when a Calcien-AM staining was performed. This was approximately one third the laser spot width of 1.6 mm. This result was thought to be caused by the low thermal dose near the periphery of the treatment zone where the local temperature profile was Gaussian, similar to the laser intensity profile. Heat transport was predominantly in the radial direction, but the cellular injury associated with this energy transport was found to be negligible, i.e., no cell death was observed outside of the laser focused spot.

In last part of this work, tissue-light interaction for QD thermometry was studied experimentally and theoretically. For the experimental part, QD fluorescence through a gelatin tissue phantom was measured by varying both temperature and tissue phantom thickness. The spatial QD fluorescence intensity distribution at room temperature showed the intensity distribution with thickness caused by scattering and confirmed by a theoretical model of tissue-light interaction. This model employed the diffusion approximation of the radiative transfer equation. The effects of tissue-light interaction with intensity-temperature correlation show a linear intensity-temperature relationship with the slope inversely proportional to tissue phantom thickness. This would imply that an in vivo QD-mediated thermometry may be feasible, even in turbid media. Thus, if tumor depth and geometry are known beforehand, the spatiotemporal change of QD fluorescnece will provide spatiotemporal information on the extent of thermal destruction during the treatment. Tumors typically applicable for thermal therapy are 1-2 cm in diameter, with a surgical margin of 5 mm at a minimum. Thus, a reliable thermometry should be capable of a spatial resolution of a few millimeters, minimally. These findings show a QD thermometry scheme with a spatial resolution capable of monitoring the thermal lesion intraoperatively.

In summary, this dissertation work researched the use of QDs as new temperature transducer to monitor tissue temperature during thermal therapy. The expected significance of this work is that, by integrating thermal engineering with imaging, real-time volumetric temperature information will provide a more robust tool for use in thermal surgery, thus contributing to the field of thermal engineering. Knowledge gained by this line of research will address one of the most significant challenges in thermal therapy. This thermometry platform will have offer the capacity for three dimensional monitoring of the thermal surgical procedure when used in conjunction with other volumetric imaging systems.

Before this application can be of practical use, other considerations need to be addressed. A major concern is that QDs currently with enough quantum yield to be practical are heavy metals and by nature toxic to biological tissue. Other issues concerning the use of QDs as temperature transducers include effectiveness of delivery, limited penetration depth, and the eventual clearance from the body. Further investigation is required to address QD attenuation caused by tissue scattering, ice-ball formation during cryosurgery, and the uniformity of transport from/to the treatment lesion. Future work should include integration of a numerical solution to the inverse boundary problem and its integration into an imaging system to provide a more robust real-time fluorescence monitoring modality.

APPENDIX A

ILLUSTRATIONS

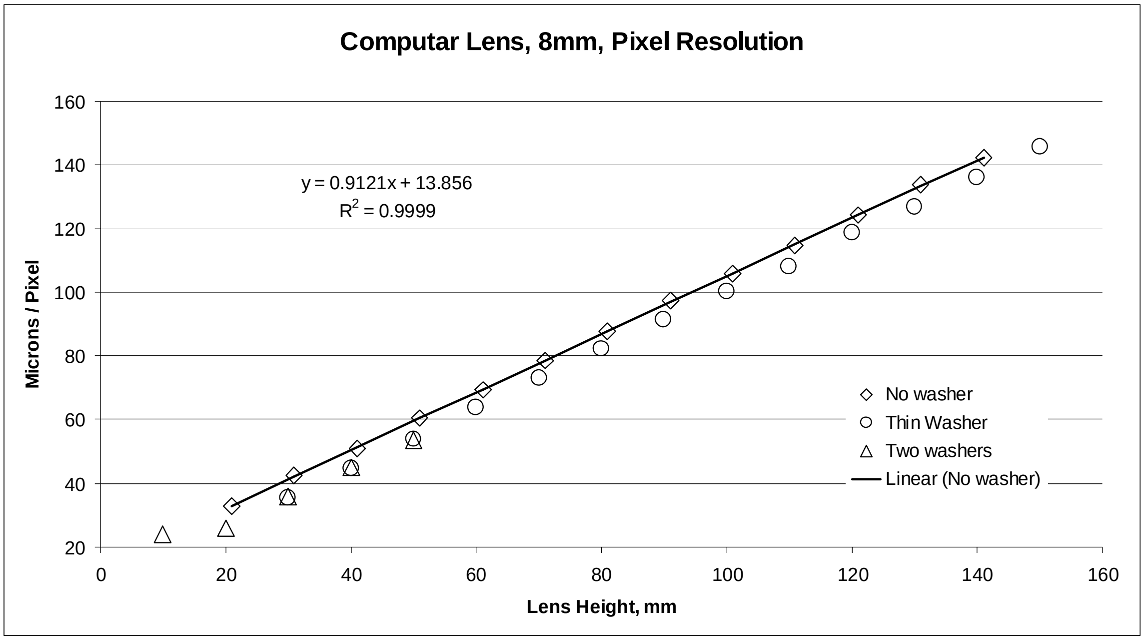

Figure A.1. Interpolation figure for lens height with pixel count

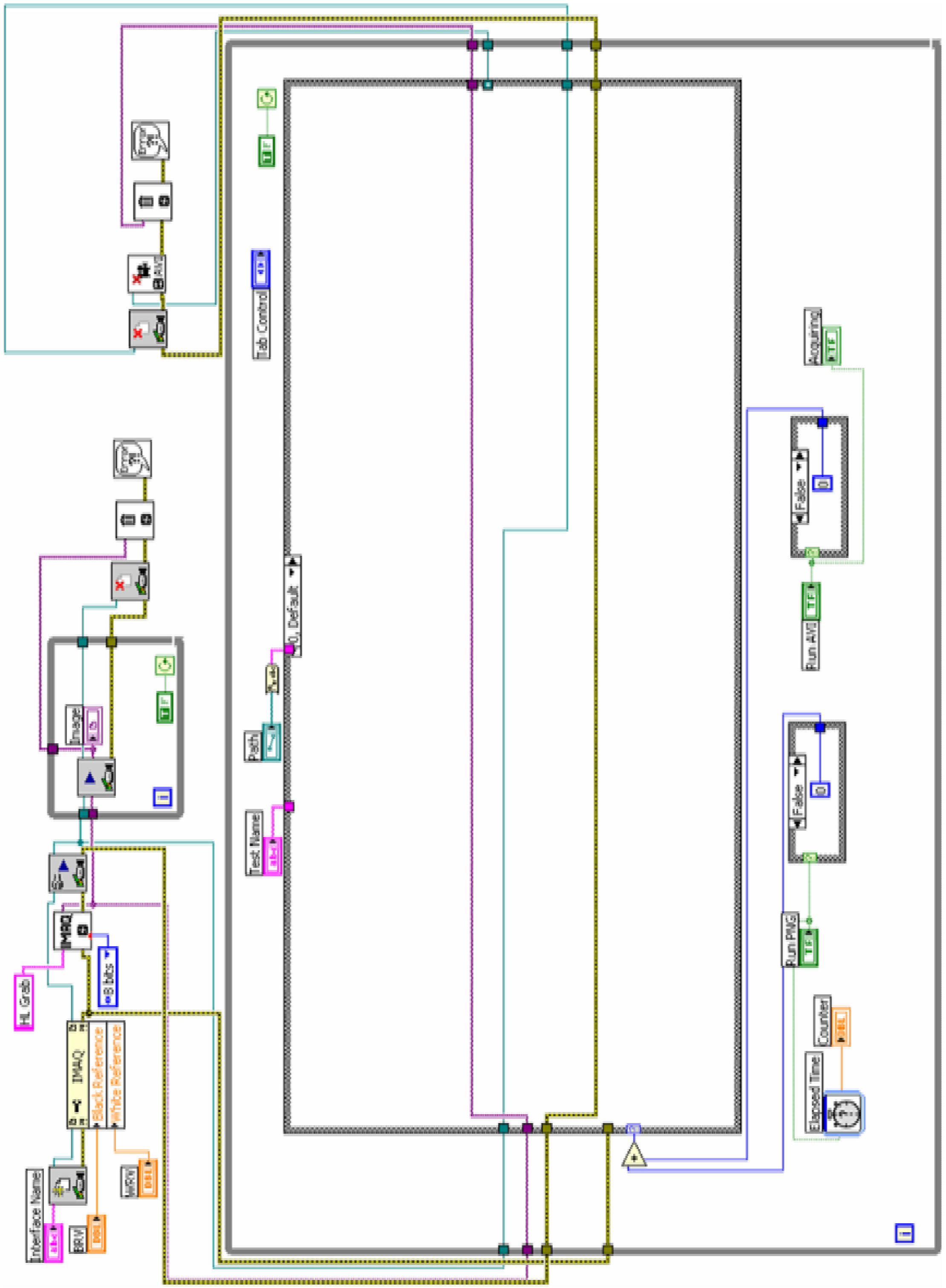

Figure A.2. LabVIEW data acquisition program showing the dwell function

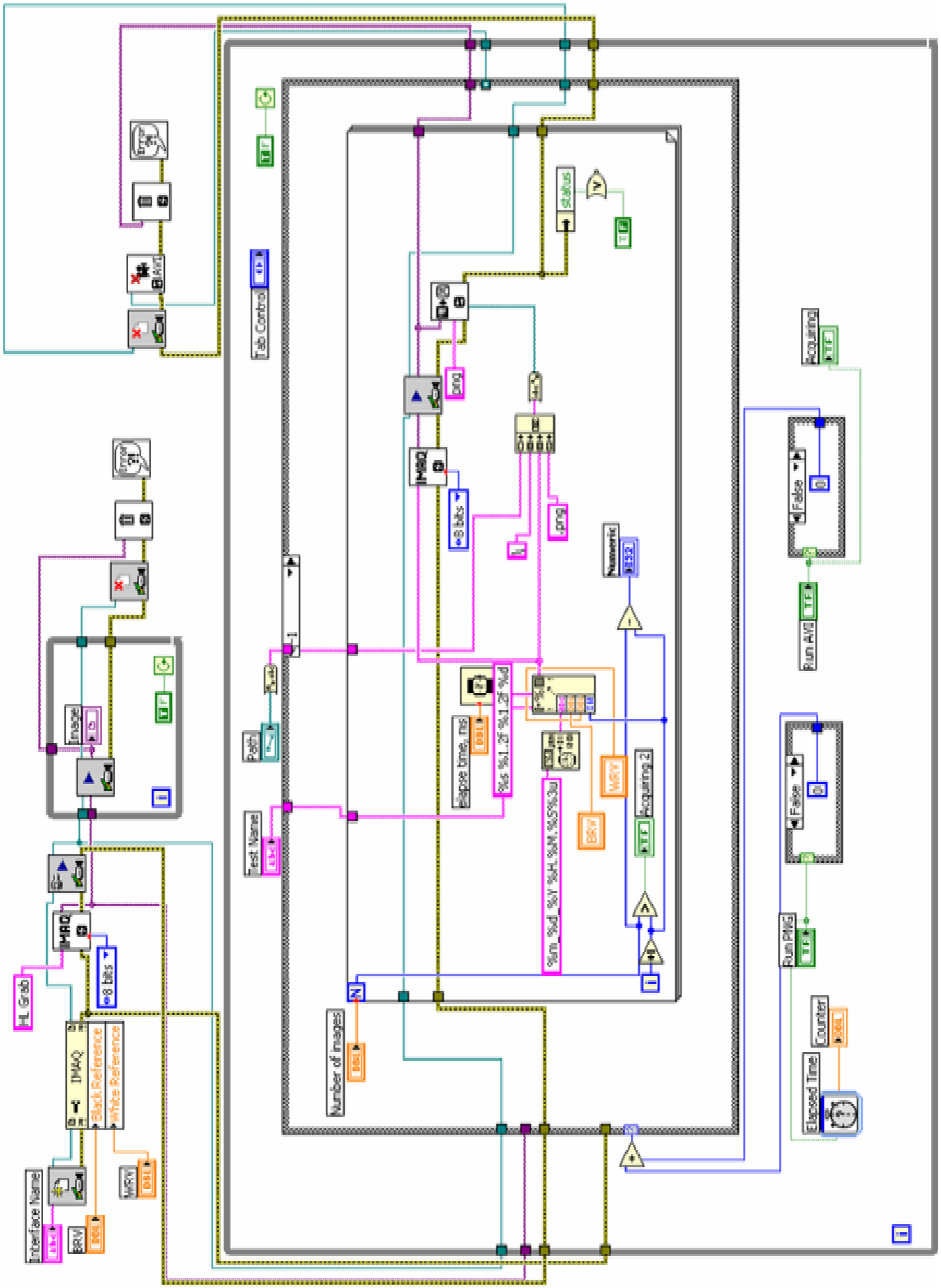

Figure A.3. LabVIEW data acquisition program showing the PNG image capture routine

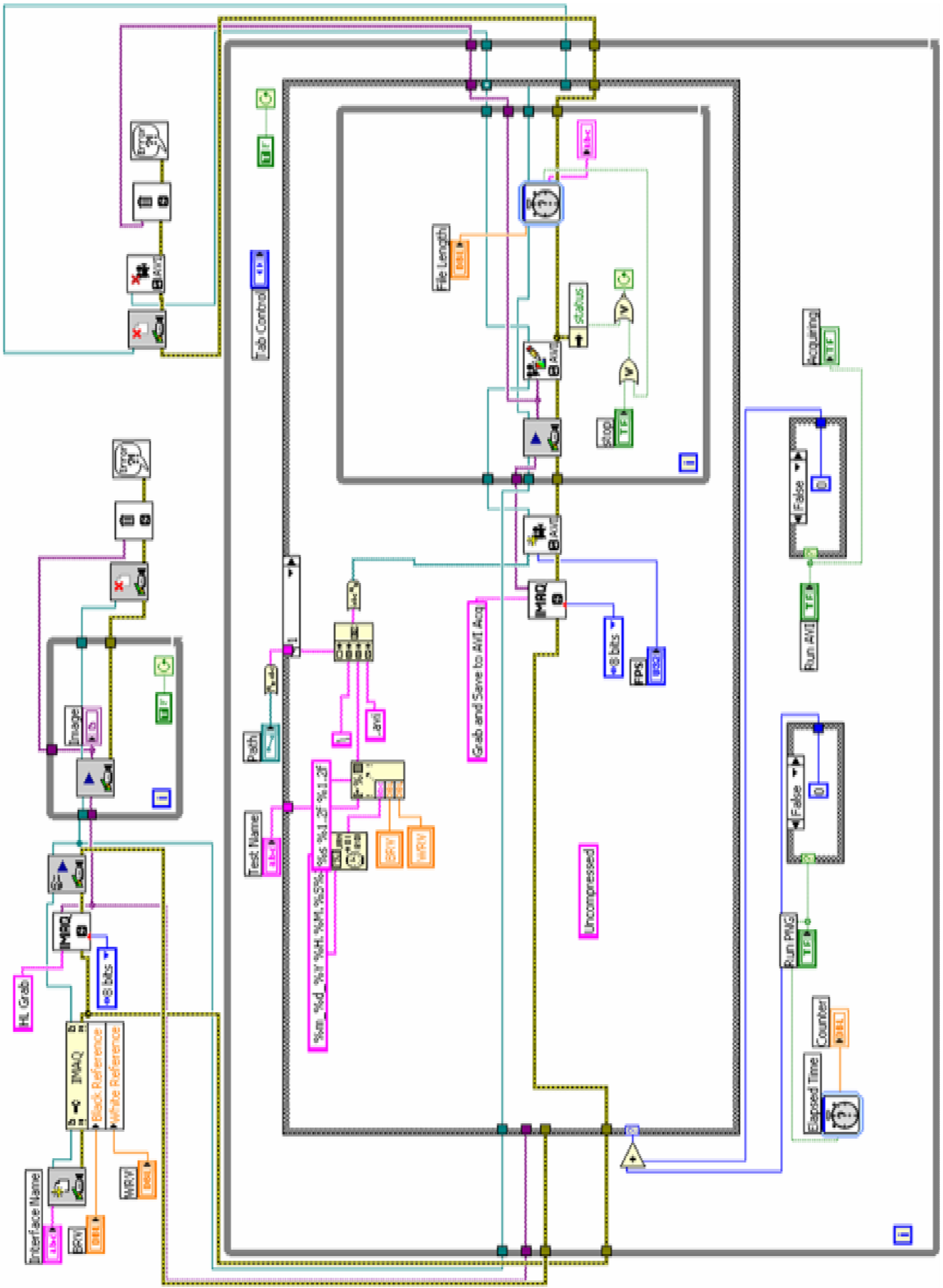

Figure A.4. LabVIEW data acquisition program showing the AVI image sequence capture routine

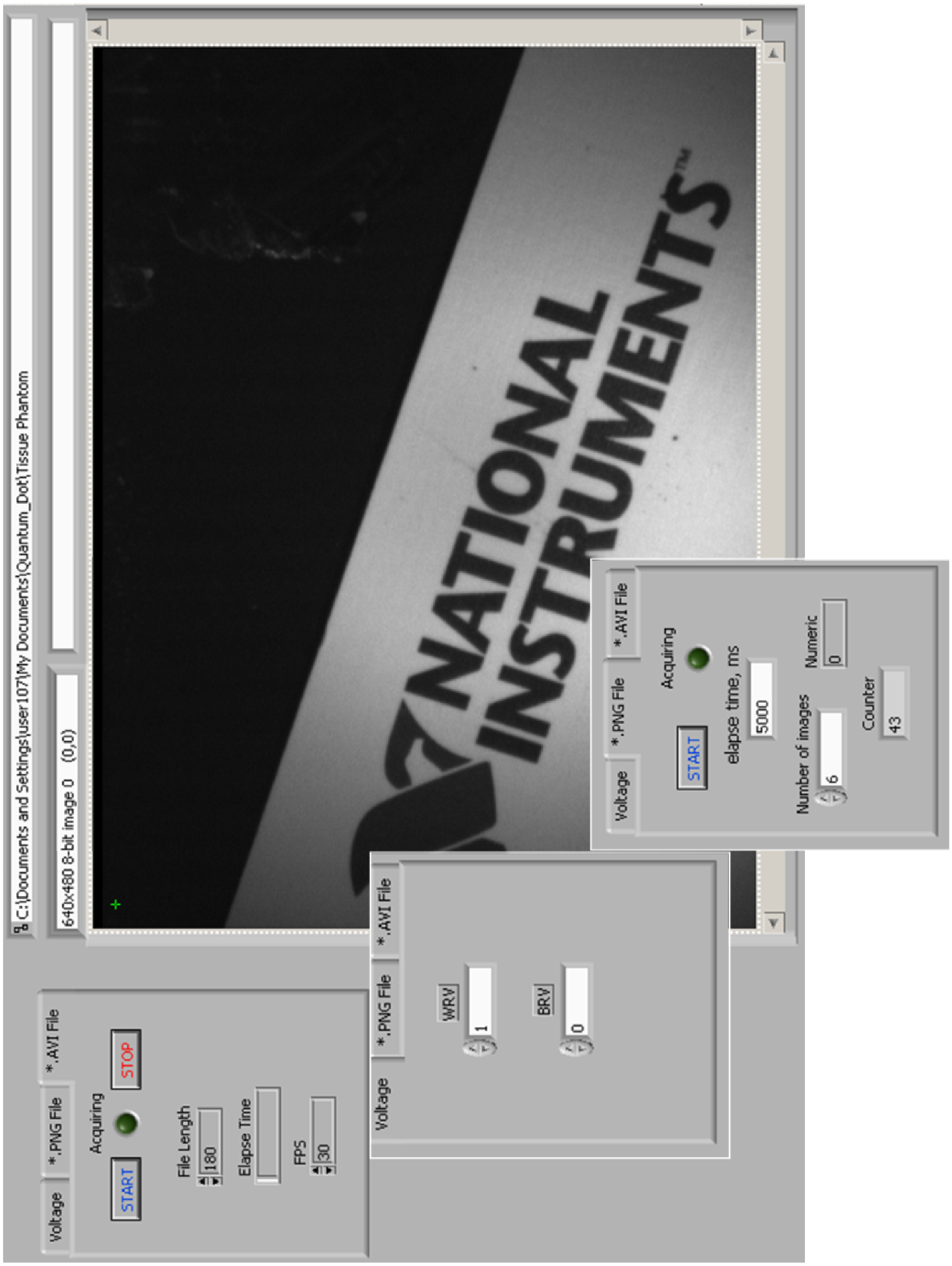

C:\Documents and Settings\user107\My Documents\Quantum_Dot\Tissue Phantom

640x480 8-bit image 0 (0,0)

File Length 180

Elapse Time

FPS 30

WRV 1

BRV 0

elapse time, ms 5000

Number of images 6

Numeric 0

Counter 43

Figure A.5. LabVIEW data acquisition user interface with tabs expanded to show user input

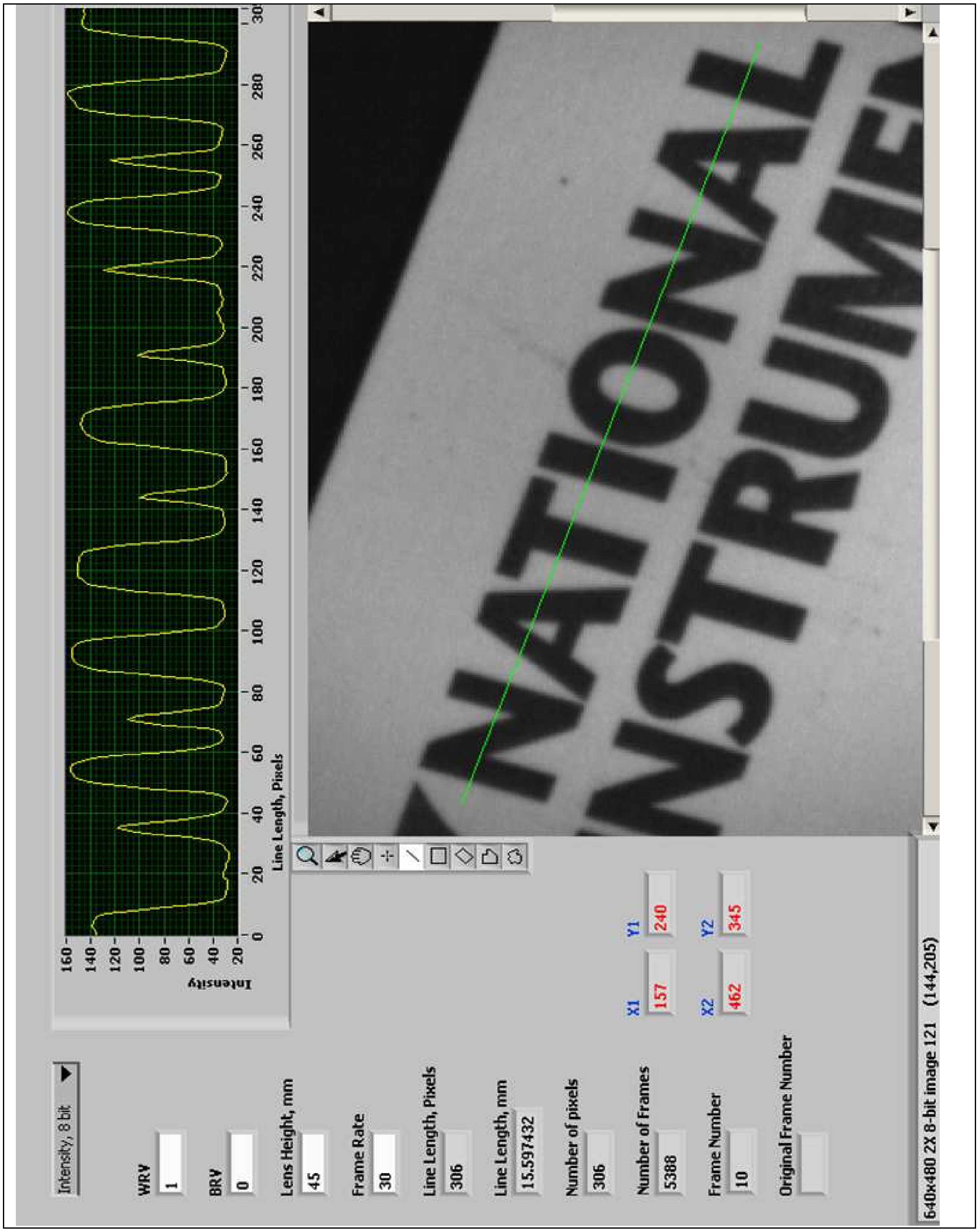

WRV 1
BRV 0
Lens Height, mm 45
Frame Rate 30
Line Length, Pixels 306
Line Length, mm 15.597432
Number of pixels 306
Number of Frames 5388
Frame Number 10
Original Frame Number
X1 157
Y1 240
X2 462
Y2 345
640x480 2X 8-bit image 121 (144,205)

Figure A.6. LabVIEW data reduction user interface showing voltage scaling, camera information, image with query line drawn and corresponding intensity versus relative pixel position

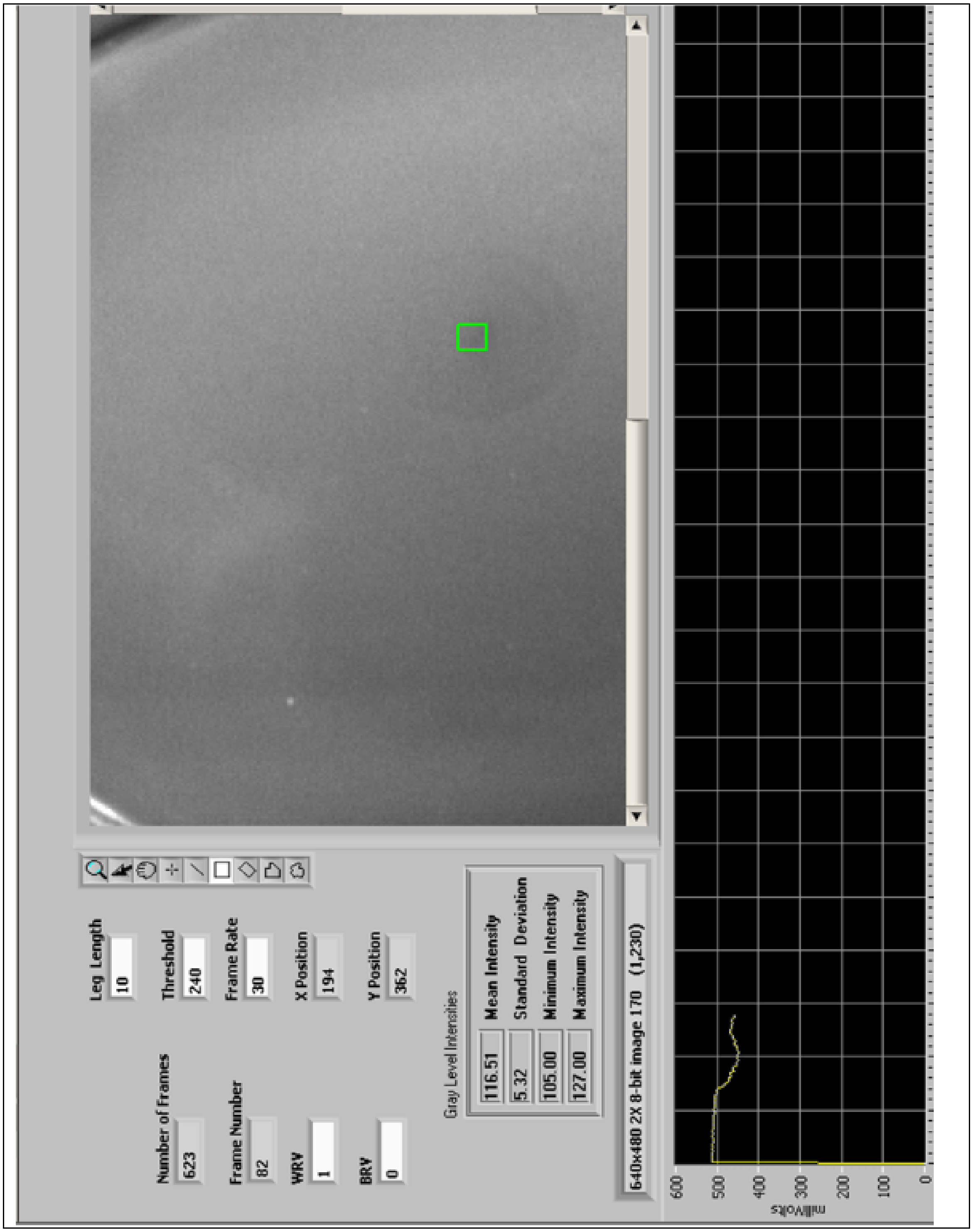

Number of Frames: 623

Frame Number: 82

WRV: 1

BRV: 0

Leq Length: 10

Threshold: 240

Frame Rate: 30

X Position: 194

Y Position: 362

Gray Level Intensities

Mean Intensity	116.51
Standard Deviation	5.32
Minimum Intensity	105.00
Maximum Intensity	127.00

640x480 2X 8-bit image 170 (1,230)

Figure A.7. LabVIEW data reduction user interface showing query information, image with query area drawn and corresponding intensity versus average intensity value versus time

Diomed25 technical specifications

Laser type	GaAlAs laser diode
Wavelength	805 nm (+/- 25 nm)
Power output	0.5 – 25W (+/-10%)
Treatment modes	Continuous, pulsed and repeat pulse
Pulse duration	0.1 - 9.9 seconds
Repeat mode 0.1 – 1.0 second interval	0.1 – 1.0 second pulse duration
Countdown	10 – 3200 seconds
Calibration	Automatic fiber calibration
Power meter	Thermopile or power measurement
Aiming beam	Visible laser diode 650 nm, nominally 5mW at port continuous or intermittent
Cooling	Forced air
Power supply	100 – 140VAC 220VA
Dimensions (HxWxD)	6”x15”x15”
Weight	24lb
Fibers	600 and 1000 µm contact fibers
Fiber connector	Standard SMA 905
Safety standards	IEC 601-1, IEC 601-2-22, IEC 825 21 CFR 1040.10, 21 CFR 1040.11 ETL listed (tested to UL 544 standard)

Figure A.8. Diomend 25 laser technical specifications

Figure A.9. Photo showing a typical setup for Laser QNS experiment

APPENDIX B

TABLES

Table B.1. Required volumetric quantity of three constituents to form appropriate amount of tissue phantom

Tissue phantom(ml)	**Gelatin (g)**	**Water(ml)**	**Milk(ml)**
1	0.109	0.565977	0.323415
2	0.219	1.131953	0.646831
3	0.329	1.69793	0.970246
4	0.439	2.263907	1.293661
5	0.549	2.829884	1.617076
10	1.099	5.659767	3.234153
15	1.649	8.489651	4.851229
30	3.298	16.9793	9.702458
45	4.947	25.46895	14.55369
50	5.497	28.29884	16.17076
100	10.994	56.59767	32.34153

APPENDIX C

CALCULATIONS

C.1 Diffusion Approximation Calculation

Derivation of the diffusion approximation (DA) from the radiative transfer equation (RTE) [105].

$$\frac{1}{c_m}\frac{dI(r(t),\hat{s},t)}{dt} = -(\mu_a + \mu_s)I(r(t),\hat{s},t) + \frac{(\mu_a + \mu_s)}{4\pi}\int_{4\pi} p(\hat{s},\hat{s}')I(r(t'),\hat{s}',t)d\Omega' + Q(r(t),\hat{s},t)$$

Where:

- $I(r(t),\hat{s},t)$, the intensity as a function of location, $r(t)$, direction, $\hat{s}$, and time, t
- μ_a and μ_s are the absorbance and scattering coefficients respectively
- c_m, the speed of light in the medium
- $p(\hat{s},\hat{s}')$, the scattering phase function
- Ω', the measure of solid angle, in steradians

Let the radiance be measured with respect to the surrounding media. The variation of intensity along a path in this frame of reference is, $\frac{d}{dt} = \frac{\partial}{\partial t} + c\hat{s}\cdot\nabla$

Now, for steady state conditions and without sources the RTE yields,

$$\hat{s}\cdot\nabla I(r,\hat{s}) = -(\mu_a + \mu_s)I(r,\hat{s}) + \frac{(\mu_a + \mu_s)}{4\pi}\int_{4\pi} p(\hat{s},\hat{s}')I(r,\hat{s}')d\Omega'$$

Recognizing spontaneous emission, isotropic scattering and notation from [111],

$$\frac{\mathrm{di}}{\mathrm{dS}} = -(\mu_a + \mu_s)\mathrm{i} + \mu_a \mathrm{i}_b + \frac{(\mu_a + \mu_s)}{4\pi}\int_{4\pi} \mathrm{i}(\mathrm{r}, \omega')\mathrm{d}\omega' \tag{C.1.1}$$

Let S be a distance element. The change in radiance along this element becomes,

$$\frac{\mathrm{di}}{\mathrm{dS}} = \frac{\mathrm{di}}{\mathrm{dx_i}}\frac{\mathrm{dx_i}}{\mathrm{dS}} \quad \mathrm{i} = 1, 2, 3$$

For θ, and φ, the polar and azimuthal angles respectively, the directional cosines are,

$$\frac{\mathrm{d}\overline{\mathrm{x}}}{\mathrm{dS}} = \sum_{\mathrm{i}=1}^{3}\frac{\mathrm{dx_i}}{\mathrm{dS}} = \hat{\mathrm{i}}\cos\delta + \hat{\mathrm{j}}\cos\gamma + \hat{\mathrm{k}}\cos\theta = \hat{\mathrm{i}}\sin\theta\cos\varphi + \hat{\mathrm{j}}\sin\theta\sin\varphi + \hat{\mathrm{k}}\cos\theta = \sum_{\mathrm{i}=1}^{3}\mathrm{l_i}$$

(C.1.2)

Using optical coordinates,

$$\mathrm{d}\,\kappa_i = (\mu_a + \mu_s)\mathrm{d}\,x_i \tag{C.1.3}$$

Substituting (C.1.2) and (C.1.3) into (C.1.1)

$$\frac{\mathrm{d}i}{\mathrm{d}S}=\sum_{i=1}^{3} l_i \frac{\mathrm{d}i}{\mathrm{d}\kappa_i}(\mu_a+\mu_s)=-(\mu_a+\mu_s)i+\mu_a i_b+\frac{(\mu_a+\mu_s)}{4\pi}\int_{4\pi} i(r,\omega')\mathrm{d}\omega'$$

(C.1.4)

The albedo, Ω, is a measure of reflectivity,

$$\Omega=\frac{\mu_s}{\mu_a+\mu_s} \quad \text{or} \quad 1-\Omega=\frac{\mu_a}{\mu_a+\mu_s} \tag{C.1.5}$$

Now substituting (C.1.5) into (C.1.4),

$$\sum_{i=1}^{3} l_i \frac{\mathrm{d}i}{\mathrm{d}\kappa_i}+i=(1-\Omega)i_b+\frac{\Omega}{4\pi}\int_{4\pi} i(r,\omega')\mathrm{d}\omega' \tag{C.1.5}$$

In spherical harmonics the directional cosines (C.1.2) are represented by [106],

$$\sum_{i=1}^{3} l_i=\sqrt{\frac{2\pi}{3}}\left\{Y_1^{-1}(S)-Y_1^{1}(S),\quad j\left[Y_1^{-1}(S)+Y_1^{1}(S)\right],\quad \sqrt{2}Y_1^{0}(S)\right\} \tag{C.1.5}$$

Where, $Y_1^{-1}=\sqrt{\frac{3}{8\pi}}\sin\theta\, e^{-j\varphi}, \quad Y_1^{0}=\sqrt{\frac{3}{4\pi}}\cos\theta, \quad Y_1^{1}=-\sqrt{\frac{3}{8\pi}}\sin\theta\, e^{j\varphi}$

The RTE may be approximated as a set of differential equations using spherical harmonics as a change of basis. Thus, for a P_1 approximation,

$$\mathrm{I}(\mathrm{S},\hat{\mathrm{s}}) = \mathrm{I}(\mathrm{S},\theta,\varphi) = \sum_{l=0}^{1}\sum_{m=-l}^{l} \mathrm{A}_l^m(\mathrm{S})\mathrm{Y}_l^m(\theta,\varphi) = \mathrm{A}_0^0\mathrm{Y}_0^0 + \mathrm{A}_1^{-1}\mathrm{Y}_1^{-1} + \mathrm{A}_1^0\mathrm{Y}_1^0 + \mathrm{A}_1^1\mathrm{Y}_1^1$$

$$I(S,\theta,\varphi) = A_0^0\frac{1}{\sqrt{4\pi}} + A_1^{-1}\sqrt{\frac{3}{8\pi}}\sin\theta e^{-j\varphi} + A_1^0\sqrt{\frac{3}{4\pi}}\cos\theta - A_1^1\sqrt{\frac{3}{8\pi}}\sin\theta e^{j\varphi}$$

For the zeroth moment, l = 0, m = 0, represents the isotropic component and when divided by c_m determines the radiative energy density [106],

$$I^0(S) = \int_{\omega=0}^{4\pi} I(S,\omega)d\omega = \int_{\varphi=0}^{2\pi}\int_{\theta=0}^{\pi} I(S,\theta,\varphi)\sin\theta d\theta d\varphi$$

$$\begin{aligned} I^0(S) = {} & A_0^0\frac{1}{\sqrt{4\pi}}\int_{\theta=0}^{\pi}\sin\theta d\theta\int_{\varphi=0}^{2\pi}d\varphi + A_1^{-1}\sqrt{\frac{3}{8\pi}}\int_{\theta=0}^{\pi}\sin^2\theta d\theta\int_{\varphi=0}^{2\pi}e^{-j\varphi}d\varphi \\ & + A_1^0\sqrt{\frac{3}{4\pi}}\int_{\theta=0}^{\pi}\cos\theta\sin\theta d\theta\int_{\varphi=0}^{2\pi}d\varphi - A_1^1\sqrt{\frac{3}{8\pi}}\int_{\theta=0}^{\pi}\sin^2\theta d\theta\int_{\varphi=0}^{2\pi}e^{j\varphi}d\varphi \end{aligned}$$

$$\begin{aligned} I^0(S) &= \sqrt{4\pi}\cdot A_0^0 + A_1^{-1}\sqrt{\frac{3}{8\pi}}\cdot\frac{\pi}{2}\cdot 0 + A_1^0\sqrt{\frac{3}{4\pi}}\cdot 2\pi\cdot 0 - A_1^1\sqrt{\frac{3}{8\pi}}\cdot\frac{\pi}{2}\cdot 0 \\ &= \sqrt{4\pi}\cdot A_0^0 \end{aligned}$$

The fluence rate or photon density is [112], $\Phi(\bar{r},t) = 4\pi A_0^0 Y_0^0(S)$

$$\Phi(\bar{r},t) = \sqrt{4\pi}I^0(S)Y_0^0(S) = \sqrt{4\pi}I^0(S)\frac{1}{\sqrt{4\pi}} = I^0(S)$$

The first moment, l = 1, m = -l, 0, 1, represents the anisotropic component and determines the radiative energy flux [106],

$$I^i(S) = \int_{\omega=0}^{4\pi} l_i I(S,\omega) d\omega = \int_{\varphi=0}^{2\pi}\int_{\theta=0}^{\pi} l_i I(S,\theta,\varphi) \sin\theta d\theta d\varphi \quad (i = 1, 2, 3)$$

$$I^1(S) = \sqrt{\frac{2\pi}{3}}\left[\int_{4\pi}\left(Y_1^{-1}(\hat{s}) - Y_1^1(\hat{s})\right)\left(A_1^{-1}Y_1^{-1} + A_1^0 Y_1^o + A_1^1 Y_1^1\right) d\Omega\right]$$

$$= \sqrt{\frac{3}{32\pi}}\begin{bmatrix} A_1^{-1}\int_{\varphi=0}^{2\pi}\int_{\theta=0}^{\pi}\left(e^{-j\varphi} + e^{j\varphi}\right)\sin^3\theta\, e^{-j\varphi}\, d\theta\, d\varphi \\ +\sqrt{2}A_1^0\int_{\varphi=0}^{2\pi}\int_{\theta=0}^{\pi}\left(e^{-j\varphi} + e^{j\varphi}\right)\sin^2\theta\cos\theta\, d\theta\, d\varphi \\ -A_1^1\int_{\varphi=0}^{2\pi}\int_{\theta=0}^{\pi}\left(e^{-j\varphi} + e^{j\varphi}\right)\sin^3\theta\, e^{j\varphi}\, d\theta\, d\varphi \end{bmatrix} = \sqrt{\frac{2\pi}{3}}\left(A_1^{-1} - A_1^1\right)$$

$$I^2(S) = -j\sqrt{\frac{2\pi}{3}}\left(A_1^{-1} + A_1^1\right)$$

$$I^3(S) = \sqrt{\frac{4\pi}{3}} A_1^0$$

Where the following identities have been implemented,

$$Y_{l,-m}(\hat{s}) = (-1)^m Y^*{}_{l,m}(\hat{s}) \text{ and } \int_{4\pi} Y_{l,m}(\hat{s}) Y^*{}_{l',m'}(\hat{s}) d\Omega = \delta_{ll',mm'}$$

$$I^{m+2}(S) = \sum_{m=-1}^{1}\int_{4\pi} l_{m+2} Y_{1,m}(\hat{s}) d\Omega$$

Thus the energy flux yields [112],

$$\bar{J}(\bar{r},t)=\sqrt{\frac{2\pi}{3}}\left\{A_1^{-1}-A_1^{1}, \quad -j\left[A_1^{-1}+A_1^{1}\right], \quad \sqrt{2}A_1^{0}\right\}$$

The total spectral radiance for a P_1 approximation is now,

$$\begin{aligned}I(S,\theta,\varphi)&=\frac{1}{4\pi}I^{0}(S)+\frac{3}{4\pi}\sum_{m=1}^{3}I^{m}(S)\\&=\frac{1}{4\pi}A_0^{0}+\sqrt{\frac{3}{8\pi}}\left\{A_1^{-1}-A_1^{1}, \quad j\left[A_1^{-1}+A_1^{1}\right], \quad \sqrt{2}A_1^{0}\right\}\\&=\frac{1}{4\pi}\Phi(S,t)+\frac{3}{4\pi}J(S,t)\cdot\hat{s}\end{aligned}$$

$$I(\bar{r},\hat{s})=\frac{1}{4\pi}\Phi(\bar{r},t)+\frac{3}{4\pi}J(\bar{r},t)\cdot\hat{s}$$

Inserting $I(\bar{r},\hat{s})$ into the steady state RTE, without sources and integrating over the entire solid angle yields,

$$\hat{s}\cdot\nabla I(r,\hat{s})=-(\mu_a+\mu_s)I(r,\hat{s})+\frac{(\mu_a+\mu_s)}{4\pi}\int_{4\pi}p(\hat{s},\hat{s}')I(r,\hat{s}')d\Omega'$$

$$\int_{4\pi}\hat{s}\cdot\nabla I(r,\hat{s}')d\Omega'=-(\mu_a+\mu_s)\int_{4\pi}\nabla I(r,\hat{s}')d\Omega'+\frac{(\mu_a+\mu_s)}{4\pi}\int_{4\pi}\left[\int_{4\pi}p(\hat{s},\hat{s}')I(r,\hat{s}')d\Omega'\right]d\Omega$$

For the left hand side term we employ the identity,

$\hat{s}\cdot\nabla I(r,\hat{s})=\nabla\cdot(\hat{s}I(r,\hat{s}))-I(r,\hat{s})\nabla\cdot\hat{s}$, and recognize that, $\nabla\cdot\hat{s}=0$ because the scaling factor for a constant radius is zero.

Now,

$$\begin{aligned}\int_{4\pi}\hat{s}\cdot\nabla I(r,\hat{s}')d\Omega' &= \int_{4\pi}\nabla\cdot\left[\hat{s}I(r,\hat{s}')\right]d\Omega' \\ &= \nabla\cdot\int_{4\pi}\hat{s}I(r,\hat{s}')d\Omega' \\ &= \nabla\cdot J(\bar{r})\end{aligned}$$

The first term on the right is by definition the fluence rate,

$$(\mu_a+\mu_s)\int_{4\pi}\nabla I(r,\hat{s}')d\Omega' = (\mu_a+\mu_s)\Phi(\bar{r})$$

The second term on the right is an integral composed of two terms

$$\begin{aligned}\frac{(\mu_a+\mu_s)}{4\pi}\int_{4\pi}\left[\int_{4\pi}p(\hat{s},\hat{s}')I(r,\hat{s}')d\Omega'\right]d\Omega &= \frac{(\mu_a+\mu_s)}{4\pi}\int_{4\pi}\left[\int_{4\pi}p(\hat{s},\hat{s}')(\Phi(\bar{r})+3J(\bar{r})\cdot\hat{s})d\Omega'\right]d\Omega \\ &= \frac{(\mu_a+\mu_s)}{4\pi}\int_{4\pi}\left[\int_{4\pi}p(\hat{s},\hat{s}')\Phi(\bar{r})d\Omega'\right]d\Omega \\ &\quad+\frac{3(\mu_a+\mu_s)}{4\pi}\int_{4\pi}\left[\int_{4\pi}p(\hat{s},\hat{s}')J(\bar{r})\cdot\hat{s}d\Omega'\right]d\Omega\end{aligned}$$

The first integral is composed of the fluence rate term, $\Phi(\bar{r})$, which is not a function of spherical angle, and the probability density function (PDF).

The integral of the PDF is one, $\int_{4\pi}p(\hat{s},\hat{s}')d\Omega' = 1$ this leaves,

$$\frac{(\mu_a+\mu_s)\Phi(\bar{r})}{4\pi}\int_{4\pi}d\Omega = (\mu_a+\mu_s)\Phi(\bar{r})$$

The second integral is zero, due to $J(\bar{r})$ being aligned with the z axis.

Collecting terms,

$$\begin{aligned}\hat{s}\cdot\nabla I(r,\hat{s}) &= -(\mu_a+\mu_s)I(r,\hat{s})+\frac{(\mu_a+\mu_s)}{4\pi}\int_{4\pi}p(\hat{s},\hat{s}')I(r,\hat{s}')d\Omega' \\ \nabla\cdot\bar{J}(\bar{r}) &= -(\mu_a+\mu_s)\Phi(\bar{r})+\mu_s\Phi(\bar{r}) \\ &= -\mu_a\Phi(\bar{r})\end{aligned}$$

Finally the diffusion equation may be approximated by assuming that the change in current flux over a distance traveled during the "transport mean free time" is minimal [106]. This allows us to approximate, the current flux as Fick's law,

$$\bar{J}(\bar{r}) = -D\nabla\Phi(\bar{r})$$

Where,

$$D = \frac{1}{3(\mu_a+(1-g)\mu_s)} = \frac{1}{3(\mu_a+\mu_s')}$$

$$\nabla\cdot\bar{J}(\bar{r}) = -D\nabla^2\Phi(\bar{r}) = -\mu_a\Phi(\bar{r})$$

$$D\nabla^2\Phi(\bar{r}) - u_a\Phi(\bar{r}) = 0$$

This final equation is a function of four terms when including time, and six terms when including the spherical angles, θ and φ.

Also note, u_s and g are not independent, but show up as the "similarity relation" u_s' valid for the diffusion approximation equation [106].

Two approximations were made when deriving the diffusion approximation equation. The first was expansion of radiance, RTE, limited to the first-order spherical harmonics, P_1. The second was assuming the fractional change in current density along the "transport mean free path" would be much less than one. Both assumptions there being multiple scattering events [106]

C.2 Strong to Weak Function Calculation

This section shows the transformation of a second order operator, $\int \nabla^2$, from a strong to weak form for use in a numerical formulation. By reducing the order of the operator the resulting term requires only a single derivative for a linear interpolation method, i.e., Galerkin's method, [113]. The following equation is a 2-D strong form representation of our governing equation.

$$\int_{z1}^{z2}\int_{x1}^{x2}\psi\left(D\left(\frac{\partial^2\varphi}{\partial x^2}+\frac{\partial^2\varphi}{\partial z^2}\right)-\mu_a\varphi\right)dx\,dz=0 \tag{C.2.1}$$

To illustrate the reduction of order we manipulate the first term of (C.2.1) through integration by parts,

$$\int_{z1}^{z2}\int_{x1}^{x2}\psi\frac{\partial^2\varphi}{\partial x^2}dx\,dz=\int_{z1}^{z2}\psi\frac{\partial\varphi}{\partial x}\bigg|_{x1}^{x2}dz-\int_{z1}^{z2}\int_{x1}^{x2}\frac{\partial\psi}{\partial x}\frac{\partial\varphi}{\partial x}dx\,dz \tag{C.2.2}$$

From Green's theorem over a surface, S, and around a boundary, C,

$$\int_S\left(\frac{\partial N}{\partial x}-\frac{\partial M}{\partial z}\right)dA=\oint_C M dx+N dz,\quad \text{Let, } M=0 \text{ and } N=\psi\frac{\partial\varphi}{\partial x} \tag{C.2.3}$$

Substitute and evaluate the LHS of (C.2.3),

$$\int_S \left(\frac{\partial N}{\partial x}\right) dA = \int_S \frac{\partial}{\partial x}\left(\psi \frac{\partial \varphi}{\partial x}\right) dA = \int_{z1}^{z2}\int_{x1}^{x2} \frac{\partial}{\partial x}\left(\psi \frac{\partial \varphi}{\partial x}\right) dx\, dz = \int_{z1}^{z2} \psi \frac{\partial \varphi}{\partial x}\bigg|_{x1}^{x2} dz$$

(C.2.4)

Now, along the boundary,

$$\cos\theta = \frac{dz}{d\Gamma} = \frac{\overline{n}_x}{\overline{n}} = \overline{n}_x \rightarrow dz = \overline{n}_x d\Gamma \qquad \text{(C.2.5)}$$

Substituting (C.2.5) into the RHS of (C.2.3),

$$\oint_C N dz = \oint_C \psi \frac{\partial \varphi}{\partial x} dz = \oint_\Gamma \psi \frac{\partial \varphi}{\partial x} n_x d\Gamma \qquad \text{(C.2.6)}$$

Equating (C.2.4) and (C.2.6),

$$\int_{z1}^{z2} \psi \frac{\partial \varphi}{\partial x}\bigg|_{x1}^{x2} dz = \oint_\Gamma \psi \frac{\partial \varphi}{\partial x} n_x d\Gamma \qquad \text{(C.2.7)}$$

Substituting the RHS of (C.2.7) into the first term on the RHS of (C.2.2)

$$\int_{z1}^{z2}\int_{x1}^{x2} \psi \frac{\partial^2 \varphi}{\partial x^2} dx\, dz = \oint_\Gamma \psi \frac{\partial \varphi}{\partial x} n_x d\Gamma - \int_{z1}^{z2}\int_{x1}^{x2} \frac{\partial \psi}{\partial x}\frac{\partial \varphi}{\partial x} dx\, dz$$

Solving for both x and z in (C.2.1),

$$D\left[\left(\oint_{\Gamma}\psi\frac{\partial\varphi}{\partial x}n_x d\Gamma-\int_{z1}^{z2}\int_{x1}^{x2}\frac{\partial\psi}{\partial x}\frac{\partial\varphi}{\partial x}dx\,dz\right)+\left(\oint_{\Gamma}\psi\frac{\partial\varphi}{\partial z}n_z d\Gamma-\int_{z1}^{z2}\int_{x1}^{x2}\frac{\partial\psi}{\partial z}\frac{\partial\varphi}{\partial z}dx\,dz\right)\right]$$
$$-\int_{z1}^{z2}\int_{x1}^{x2}\mu_a\psi\varphi dx\,dz=0$$

Finally, we arrive at the weak form representation of (C.2.1)

$$\int_{\Omega}\left[D\left(\frac{\partial\psi}{\partial x}\frac{\partial\varphi}{\partial x}+\frac{\partial\psi}{\partial z}\frac{\partial\varphi}{\partial z}\right)+\mu_a\psi\varphi\right]d\Omega-D\left(\oint_{\Gamma}\psi\frac{\partial\varphi}{\partial x}n_x d\Gamma+\oint_{\Gamma}\psi\frac{\partial\varphi}{\partial z}n_z d\Gamma\right)=0$$

(C.2.8)

Further reduction leads to the weak form to be used as a shape function for further modification for numerical work

$$\int_{\Omega}\left(D\nabla\psi\cdot\nabla\varphi+\mu_a\psi\varphi\right)d\Omega=D\oint_{\Gamma}\psi\frac{\partial\varphi}{\partial\bar{n}}d\Gamma \qquad \text{(C.2.9)}$$

where, $\frac{\partial\varphi}{\partial\bar{n}}=\frac{\partial\varphi}{\partial x}\frac{\partial x}{\partial n}+\frac{\partial\varphi}{\partial z}\frac{\partial z}{\partial n}=\frac{\partial\varphi}{\partial x}\bar{n}_x+\frac{\partial\varphi}{\partial z}\bar{n}_z$

C.3 Diffusion Approximation Numerical Calculation

The radiative transfer equation (RTE) may be approximated by the diffusion approximation (DA) in highly scattering media, $\mu_s >> \mu_a$. This is accomplished by expanding the radiance and source terms in spherical harmonics and truncating to the first approximation, **Appendix C.1**.

We generate a numerical approximation to the DA solution by forcing values at specific locations. For instance, a 1-D expression may be expanded as,

$$f(x) = a_0 + a_1 x + a_2 x^2 + a_3 x^3 + ... + a_n x^n \qquad \text{(C.3.1)}$$

A 2-D expansion of a simple triangular element is comprised of end points only. We truncate to a linear system and adopt a set of equations for each node of the element. Thus,

$$f_i(x,z) = (a_0 + a_1 x_i + a_2 z_i) \rightarrow \begin{vmatrix} f_1 \\ f_2 \\ f_3 \end{vmatrix} = \begin{vmatrix} 1 & x_1 & z_1 \\ 1 & x_2 & z_2 \\ 1 & x_3 & z_3 \end{vmatrix} \begin{vmatrix} a_0 \\ a_1 \\ a_2 \end{vmatrix} \qquad \text{(C.3.2)}$$

Generally, $f(x,z)$ will not solve the GE exactly, e.g., the solution will involve a non zero residual, R, with some error, ε.

$$R(\varphi, x, z) = f(x,z) - \varepsilon \qquad \text{(C.3.3)}$$

Shape functions, $\Psi(x,z)$, are imposed as a multiplier to force solutions to $f(x,z)$ at specific locations. Thus, as a linear approximation,

$$f(x,z)=\sum_{i}^{n}\varphi_i(x,z)\Psi_i(x,z) \qquad \text{(C.3.4)}$$

where, $f(x,z)$ is the analytical solution and $\varphi_i(x,z)$ is the approximation. $\varphi_i(x,z)$ solves for $f(x,z)$ at the endpoints when a linear shape function is used. For a three node interpolation we would employ a quadratic shape function.

The Galerkin method of weighted residuals will be used in this calculation to implement a finite element model for a 2-D steady-state DA. This method utilizes a two point shape function as the weighting function. The Galerkin method is simple, applicable for any geometry and guaranteed to solve the governing equation (GE) through integration. For our problem, the inner product is now composed of the residual, $R(\varphi,x,z)$, and the weighting function, W_i. The residual is orthogonal to each of the weighting functions,

$$\int_0^L W_i\, R(\varphi,x,z)dx=0\rightarrow\int_\Omega \Psi\left\{D\,\nabla^2-\mu_a\right\}\varphi\, d\Omega=0$$

$$=\int_{z1}^{z2}\int_{x1}^{x2}\psi\left(D\left(\frac{\partial^2\varphi}{\partial x^2}+\frac{\partial^2\varphi}{\partial z^2}\right)-\mu_a\varphi\right)dx\,dz=0 \qquad \text{(C.3.5)}$$

There must be as many weighting functions as there are independent parameters. They also must be independent of one another, meaning the inner product between any two weight functions must be orthogonal.

$$(W_1, W_2) = \int_0^L W_1(x)\, W_2(z)\, dy = 0 \tag{C.3.6}$$

Our GE, the DA, includes second order terms in ϕ. In this form a linear solution cannot implement simple shape functions. Thus, we manipulate the integrand to obtain a weak solution, **Appendix C.2**.

$$\int_\Omega (D\nabla\psi \cdot \nabla\varphi + \mu_a\psi\varphi)\, d\Omega = D\oint_\Gamma \psi \frac{\partial\varphi}{\partial\bar{n}}\, d\Gamma \tag{C.2.9}$$

$$= \int_\Omega \left[D\left(\frac{\partial\psi}{\partial x}\frac{\partial\varphi}{\partial x} + \frac{\partial\psi}{\partial z}\frac{\partial\varphi}{\partial z} \right) + \mu_a\psi\varphi \right] d\Omega = D\oint_\Gamma \psi \frac{\partial\varphi}{\partial n}\, d\Gamma \tag{C.3.7}$$

The stiffness matrix is comprised of diffusion and absorption terms.

The diffusion term, K,

$$K = D\sum_{i,j=1}^{3}\int_\Omega \left(\frac{\partial\psi_i}{\partial x}\frac{\partial\varphi_j}{\partial x} + \frac{\partial\psi_i}{\partial z}\frac{\partial\varphi_j}{\partial z} \right) d\Omega \to K_{ij}^e = D\int_{\Omega^e} \left(\frac{\partial N_i^e}{\partial x}\frac{\partial N_j^e}{\partial x} + \frac{\partial N_i^e}{\partial z}\frac{\partial N_j^e}{\partial z} \right) \varphi_j\, d\Omega$$

$$= D\left\{\begin{bmatrix}\frac{\partial N_1}{\partial x}\\ \frac{\partial N_2}{\partial x}\\ \frac{\partial N_3}{\partial x}\end{bmatrix}\begin{bmatrix}\frac{\partial N_1}{\partial x} & \frac{\partial N_2}{\partial x} & \frac{\partial N_3}{\partial x}\end{bmatrix}+\begin{bmatrix}\frac{\partial N_1}{\partial z}\\ \frac{\partial N_2}{\partial z}\\ \frac{\partial N_3}{\partial z}\end{bmatrix}\begin{bmatrix}\frac{\partial N_1}{\partial z} & \frac{\partial N_2}{\partial z} & \frac{\partial N_3}{\partial z}\end{bmatrix}\right\}\begin{bmatrix}\varphi_1\\ \varphi_2\\ \varphi_3\end{bmatrix}\int_{z1}^{z2}\int_{x1}^{x2}dxdz$$

$$= \frac{D}{4\,A}\left\{\begin{bmatrix}k_{x,11} & k_{x,12} & k_{x,13}\\ k_{x,21} & k_{x,22} & k_{x,23}\\ k_{x,31} & k_{x,32} & k_{x,33}\end{bmatrix}+\begin{bmatrix}k_{z,11} & k_{z,12} & k_{z,13}\\ k_{z,21} & k_{z,22} & k_{z,23}\\ k_{z,31} & k_{z,32} & k_{z,33}\end{bmatrix}\right\}\begin{bmatrix}\varphi_1\\ \varphi_2\\ \varphi_3\end{bmatrix}=\frac{D}{4A}\begin{bmatrix}k_{11} & k_{12} & k_{13}\\ k_{21} & k_{22} & k_{23}\\ k_{31} & k_{32} & k_{33}\end{bmatrix}\begin{bmatrix}\varphi_1\\ \varphi_2\\ \varphi_3\end{bmatrix}$$

(C.3.8)

Where, from [113], the shape functions for simple triangular elements are,

$$N_1^{(e)}(x,y)=\frac{1}{2A^{(e)}}\left[(x_2y_3-x_3y_2)+(y_2-y_3)x+(x_3-x_2)y\right]$$
$$N_2^{(e)}(x,y)=\frac{1}{2A^{(e)}}\left[(x_3y_1-x_1y_3)+(y_3-y_1)x+(x_1-x_3)y\right]$$
$$N_3^{(e)}(x,y)=\frac{1}{2A^{(e)}}\left[(x_1y_2-x_2y_1)+(y_1-y_2)x+(x_2-x_1)y\right]$$

and where, $2A^{(e)}=(x_1y_2-x_2y_1)+(x_3y_1-x_1y_3)+(x_2y_3-x_3y_2)$ (C.3.9)

The absorption term is,

$$C=\mu_a\sum_{i,j=1}^{3}\int_{\Omega}\psi_i\ \varphi_j\ d\Omega=\mu_a\sum_{i,j=1}^{3}\int_{\Omega}N_iN_j\varphi_j d\Omega=\mu_a\int_{\Omega}\left\{\begin{bmatrix}N_1\\ N_2\\ N_3\end{bmatrix}\begin{bmatrix}N_1 & N_2 & N_3\end{bmatrix}\right\}\begin{bmatrix}\varphi_1\\ \varphi_2\\ \varphi_3\end{bmatrix}d\Omega$$

(C.3.10)

The numerical integration can be simplified when using triangular elements by using area coordinates,

$$N_i = L_i = \frac{A_i}{A} \text{ for } i = 1,2,3$$

$$N_i N_j N_k = \int_A L_1^a L_2^b L_3^c dA = \frac{a!b!c!}{(2+a+b+c)!} 2A$$

$$N_i N_j = \int_A L_i^1 L_j^1 L_k^0 dA = \frac{1!1!0!}{(2+1+1+0)!} 2A = \frac{A}{12}$$

$$= \frac{\mu_a A}{12} \begin{bmatrix} 2 & 1 & 1 \\ 1 & 2 & 1 \\ 1 & 1 & 2 \end{bmatrix} \begin{bmatrix} \varphi_1 \\ \varphi_2 \\ \varphi_3 \end{bmatrix}$$

Now the overall stiffness matrix is,

$$K + C = \frac{D}{4A} \begin{bmatrix} k_{11} & k_{12} & k_{13} \\ k_{21} & k_{22} & k_{23} \\ k_{31} & k_{32} & k_{33} \end{bmatrix} + \frac{\mu_a A}{12} \begin{bmatrix} 2 & 1 & 1 \\ 1 & 2 & 1 \\ 1 & 1 & 2 \end{bmatrix}$$

$$K + C = \frac{D}{4A} \begin{bmatrix} 2 & -1 & 0 \\ -1 & 1 & 0 \\ 0 & 0 & 1 \end{bmatrix} + \frac{\mu_a A}{12} \begin{bmatrix} 2 & 1 & 1 \\ 1 & 2 & 1 \\ 1 & 1 & 2 \end{bmatrix} \text{ LHT, lower half triangle}$$

$$K + C = \frac{D}{4A} \begin{bmatrix} 1 & -1 & 0 \\ -1 & 2 & -1 \\ 0 & -1 & 1 \end{bmatrix} + \frac{\mu_a A}{12} \begin{bmatrix} 2 & 1 & 1 \\ 1 & 2 & 1 \\ 1 & 1 & 2 \end{bmatrix} \text{ UHT, upper half triangle} \quad (C.3.11)$$

The load vector in this case is the convective boundary condition,

$$\beta = D\oint_{\Gamma} \psi \frac{\partial \varphi}{\partial n} d\Gamma = D\int_{x_1}^{x_2} \psi \frac{\partial \varphi}{\partial z} dx \qquad \text{(C.3.12)}$$

Transforming into natural coordinates

$$-D\frac{\partial \varphi}{\partial z} = \frac{\varphi(x,H)}{2\Lambda} \qquad \text{(C.3.13)}$$

$\beta - \frac{1}{2\Lambda}\int_{x_1}^{x_2} \psi\varphi(x,H)dx = \frac{-1^{e_i}}{4\Lambda}\begin{bmatrix}1\\1\end{bmatrix}$, where $\varphi(x,H)$ is a constant

Finally, in matrix form,

$$\int_{\Omega}\left[D\left(\frac{\partial \psi}{\partial x}\frac{\partial \varphi}{\partial x} + \frac{\partial \psi}{\partial z}\frac{\partial \varphi}{\partial z}\right) + \mu_a \psi\varphi\right]d\Omega = D\oint_{\Gamma} \psi \frac{\partial \varphi}{\partial n} d\Gamma \quad \Rightarrow \quad \left[\bar{\bar{K}} + \bar{\bar{C}}\right]\varphi = \bar{\beta}$$

$$\varphi = \frac{\frac{-1^{e_i}}{\Lambda}\begin{bmatrix}1\\1\end{bmatrix}}{\frac{D}{A}\begin{bmatrix}2 & -1 & 0\\ -1 & 1 & 0\\ 0 & 0 & 1\end{bmatrix} + \frac{\mu_a A}{3}\begin{bmatrix}2 & 1 & 1\\ 1 & 2 & 1\\ 1 & 1 & 2\end{bmatrix}} \quad \text{LHT}$$

$$\varphi = \frac{\frac{-1^{e_i}}{\Lambda}\begin{bmatrix}1\\1\end{bmatrix}}{\frac{D}{A}\begin{bmatrix}2 & -1 & 0\\ -1 & 1 & 0\\ 0 & 0 & 1\end{bmatrix} + \frac{\mu_a A}{3}\begin{bmatrix}2 & 1 & 1\\ 1 & 2 & 1\\ 1 & 1 & 2\end{bmatrix}} \quad \text{UHT} \qquad \text{(C.3.14)}$$

REFERENCES

[1] American Cancer Society. Cancer Facts and Figures 2007. Atlanta: American Cancer Society, 2007.

[2] C. K. Charny and R. L. Levin. Bioheat transfer in a branching countercurrent network during hyperthermia. J. Biomech. Eng., 111:263–270, 1989.

[3] He, X., and Bischof, J. C., 2003, "Quantification of Temperature and Injury Response in Thermal Therapy and Cryosurgery," Crit.Rev.Biomed.Eng., 31pp. 355-421.

[4] Parrish, J. A., 1984, "Laser Photomedicine," IEEE JOURNAL OF QUANTUM ELECTRONICS, QE-20(12) pp. 1386.

[5] Bischof, J. C., and He, X., 2005, "Thermal Stability of Proteins," Ann NY Acad Sci, 1066pp. 12-23.

[6] Sherar, M., 2003, "Interstitial Microwave Thermal Therapy for Prostate Cancer," J. Endourology, 17(8) pp. 617.

[7] Baek, S., 2005, "Heat-Induced Changes in the Finite Strain Viscoelastic Behavior of a Collaagenous Tissue," 127pp. 580.

[8] Goldberg, S. N., 2001, "Radiofrequency Tumor Ablation: Principles and Techniques," European Journal of Ultrasound, 13pp. 129.

[9] Niemz, M.H., 2007, "Laser-Tissue Interactions," Springer, .

[10] Vij, D.R., 2002, "Medical Applications of Lasers," Kluwer Academic, .

[11] Dai, T., 2004, "Comparison of Human Skin Opto-Thermal Response to Near-Infrared and Visible Laser Irradiations: A Theoretical Investigation," PHYSICS IN MEDICINE AND BIOLOGY, 49pp. 4861.

[12] Bhowmick, S., 2004, "In Vitro Thermal Therapy of AT-1 Dunning Prostate Tumours," Journal of Biomechanical Engineering, 122pp. 51.

[13] Dewhirst, M. W., Viglianti, B. L., Lora-Michiels, M., 2003, "Basic Principles of Thermal Dosimetry and Thermal Thresholds for Tissue Damage from Hyperthermia," Int.J.Hyperthermia, 19pp. 267-294.

[14] Moritz, A., 1947, "Studies of Thermal Injury II. the Relative Importance of Time and Surface Temperature in the Causation of Thermal Burns," American Journal of Pathology, 23pp. 695.

[15] Rylander, M. N., 2006, "Optimizing Heat Shock Protein Expression Induced by Prostate Cancer Laser Therapy through Predictive Computational Model," Journal of Biomedical Optics, 11(4) pp. 041113-1.

[16] Gage, A. A., and Baust, J., 1998, "Review: Mechanisms of Tissue Injury in Cryosurgery," Cryobiology, 37pp. 171-186.

[17] Kerr, J. F. R., 1972, "A Basic Biological Phenomenon with Wideranging Implications in Tissue Kinetics," British Journal of Cancer, 26pp. 239.

[18] Baust, J. G., 1997, "Gene-Regulated Cell Death Follows Cryosurgery." Cryobiology, 35pp. 322.

[19] Kluiwstra, J. A., 1999, "High Intensity Focused Ultrasound Phased Array for Myocardial Ablation," Dissertation, .

[20] Akduman, B., 2005, "Minimally Invasive Surgery in Prostate Cancer: Current and Future Perspectives," The Cancer Journal, 11(5) pp. 355.

[21] Madersbacher, S., 1995, "Effect of High-Intensity Focused Ultrasound on Human Prostate Cancer in Vivo," CANCER RESEARCH, 55pp. 3346.

[22] Haar, G., 1989, "High Intensity Focused Ultrasound-a Surgical Technique for the Treatment of Discrete Liver Tumours," PHYSICS IN MEDICINE AND BIOLOGY, 34(11) pp. 1743.

[23] Botros, Y. Y., 1998, "Optimal Phased Array Pattern Synthesis for Non-Invasive Cancer Ablation of Liver Tumors using High Intensity Focused Ultrasound," Dissertation, .

[24] Liu, H., 2003, "Thermal Lesion Formation and Determination for External Ultrasound Thermal Therapy," Biomedical Engineering Applications, Basis & Communications, 15(3) pp. 124.

[25] Deng, C. X., 2005, "Fluorescence Imaging for Real-Time Monitoring of High-Intensity Focused Ultrasound Cardiac Ablation," Annals of Biomedical Engineering, 33(10) pp. 1352.

[26] Prahl, S. A., 1988, "Light Transport in Tissue," .

[27] Dvorak, H. F., 1988, "Identification and Characterization of the Blood Vessels of Solid Tumors that are Leaky to Circulating Macromolecules," Am. J. Pathol., pp. 98-105.

[28] Boucher, Y., Baxter, L. T., and Jain, R. K., 1990, "Interstitial Pressure Gradients in Tissue-Isolated and Subcutaneous Tumors: Implications for Therapy," Cancer Res., 50pp. 4478-4484.

[29] Welch, A. J., 1984, "The Thermal Response of Laser Irradiated,Tissue," IEEE JOURNAL OF QUANTUM ELECTRONICS, QE-20(12) pp. 1472.

[30] Halldorsson, T., 1981, "Theoretical and Experimental Investigations Prove Nd :YAG Laser Treatment to be Safe," Lasers, Surg. Med., 1pp. 253.

[31] Ishimaru, A., 1978, "Wave Propagation and Scattering in Random Media," .

[33] Cain, C. P., 2006, "Porcine Skin Visible Lesion Thresholds for Near-Infrared Lasers Including Modeling at Two Pulse Durations and Spot Sizes," Journal of Biomedical Optics, 11(4) pp. 041109-1.

[32] Kang, H. W., 2006, "ENHANCEMENT OF HIGH POWER PULSED LASER ABLATION AND BIOLOGICAL HARD TISSUE APPLICATIONS," .

[34] Henriques, F. C., 1947, "Studies of Thermal Injury," Arch. Pathol., 43pp. 489.

[35] Brace, C. L., 2005, "Microwave Ablation of Soft Tissues using a Triaxial Antenna," .

[36] Chaplin, M., 2008, "Water and Microwaves," .

[37] Gao, X., Gui, Y., Levenson, R. M., 2004, "In Vivo Cancer Targeting and Imaging with Semiconductor Quantum Dots," Nat.Biotechnol., 22pp. 969-976.

[38] Keane, D., 2002, "New Catheter Ablation Techniques for the Treatment of Cardiac Arrhythmias," Cardiac Electrophysiology Review, 6pp. 341-348.

[39] Bae, S., 2006, "Applications of NiFe2O4 Nanoparticles for a Hyperthermia Agent in Biomedicine," APPLIED PHYSICS LETTERS, 89.

[40] Keblinskia, P., 2006, "Limits of Localized Heating by Electromagnetically Excited Nanoparticles," J. APPLIED PHYSICS, 100.

[41]Lazebnik,M.,2007," A Large-Scale Study of the Ultrawideband Microwave Dielectric Properties of Normal, Benign and Malignant Breast Tissues obtained from Cancer Surgeries," PHYSICS IN MEDICINE AND BIOLOGY, (52) pp. 6093.

[42] Simon, C. J., 2006, "Intraoperative Triple Antenna Hepatic Microwave Ablation," AJR, 187pp. W333-W340.

[43] Gazelle, S. G., 2000, "Tumor Ablation with Radio-Frequency Energy," Radiology, 217pp. 633.

[44] Moroz, P., 2001, "Status of Hyperthermia in the Treatment of Advanced Liver Cancer," Journal of Surgical Oncology, 77pp. 259-269.

[45] Goldberg, S. N., 1995, "Tissue Ablation with Radiofrequency: Effect of Probe Size, Gauge, Duration, and Temperature on Lesion Volume." Acad.Radiol., 2pp. 399-404.

[46] Goldberg, S. N., 1995, "Radiofrequency Tissue Ablation in the Rabbit Lung: Efficacy and Complications." Acad.Radiol., 2pp. 776-784.

[47] Goldberg, S. N., 1996, "Radiofrequency Tissue Ablation: Importance of Local Temperature Along the Electrode Tip Exposure in Determining Lesion Size and Shape." Acad.Radiol., 3(776) pp. 784.

[48] Rossi, S., 1998, "Percutaneous Treatment of Small Hepatic Tumors by an Expandable RF Needle Electrode," American Journal of Roentgenology, 170pp. 1015-1022.

[49] McGahan, J. P., 1996, "Hepatic Ablation using Bipolar Radiofrequency Electrocautery." Acad.Radiol., 3pp. 428-422.

[50] Miao, Y., 1997, "Ex Vivo Experiment on Radiofrequency Liver Ablation with Saline Infusion through a Screw-Tip Cannulated Electrode." J. Surg. Res., 71pp. 19-24.

[51] Scudamore, C. H., 1999, "Radiofrequency Ablation Followed by Resection of Malignant Liver Tumors," Am J Surg, 177pp. 411-417.

[52] Lorentzen, T., 1997, "Radiofrequency Tissue Ablation with a Cooled Needle in Vitro: Ultrasonography, Dose Response, and Lesion Temperature." Acad.Radiol., 4pp. 292-297.

[53] de Baere, T., 2000, "Radiofrequency Liver Ablation: Experimental Comparative Study of Water-Cooled Versus Expandable Systems," American Journal of Radiology, 176pp. 187.

[54] Goldberg, S. N., 1998, "Radio-Frequency Tumor Ablation using a Clustered Electrode Technique: Results in Animals and Patients with Liver Metastases." Radiology, 209(371) pp. 379.

[55] Goldberg, S. N., 1999, "Percutaneous Radiofrequency Tissue Ablation: Optimization of Pulsed-RF Technique to Increase Coagulation Necrosis." J Vasc Interv Radiol, 10pp. 907-916.

[56] Dodd, G., 2000, "Minimally Invasive Treatment of Malignant Hepatic Tumors: At the Threshold of a Major Breakthrough." RadioGraphics, 20pp. 9-27.

[57] Peng, X., Schlamp, M. C., Kadavanich, A. V., 1997, "Epitaxial Growth of Highly Luminescent CdSe/CdS core/shell Nanocrystals with Photostability and Electronic Accessibility," J Am Chem Soc, 119pp. 7019-7029.

[58] Bailey, R. E., and Nie, S., 2003, "Alloyed Semiconductor Quantum Dots: Tuning the Optical Properties without Changing the Particle Size," J.Am.Chem.Soc., 125pp. 7100-7106.

[59] Kim, S., Fisher, B., Eisler, H. -., 2003, "Type II Quantum Dots: CdTe/CdSe(core/shell) and CdSe/ZnTe(core/shell) Heterostructures," J.Am.Chem.Soc., 125pp. 11466-11467.

[60] Nakayama, A., 2002, "Functional Near-Infrared Imaging for Cardiac Surgery and Targeted Gene Therapy, Molecular Imaging," Molecular Imaging, 1(4) .

[61] Alivisatos, A. P., 1996, "Semiconductor Clusters, Nanocrystals, and Quantum Dots," Science, 271pp. 933-937.

[62] Xu, Y., 2005, " Synthesis and Characterization of Silica Coated CdSe/CdS Core/Shell Quantum Dots," Dissertation, .

[63] Nie, S., Xing, Y., Kim, G. J., 2007, "Nanotechnology Applications in Cancer," Annu.Rev.Biomed.Eng., 9pp. 257-288.

[64] Muller, A., 2007, "Resonance Fluorescence and Cavity Quantum Electrodynamics with Quantum Dots," Dissertation, .

[65] Chermont, Q. M., 2007, "Nanoprobes with Near-Infrared Persistent Luminescence for in Vivo Imaging," PNAS, 104(22) pp. 9266-9271.

[66] Truskey, G.A., Yuan, F., and Katz, D.F., 2004, "Transport Phenomena in Biological System," Pearson Prentice Hall, Upper Saddle River, New Jersey, .

[67] Jain, R. K., 1987, "Transport of Molecules Across Tumor Vasculature," Cancer and Metastasis Review, 6pp. 559-593.

[68] Jain, R. K., and Baxter, L. T., 1988, "Mechanisms of Heterogeneous Distribution of Monoclonal Antibodies and Other Macromolecules in Tumors: Significance of Elevated Interstitial Pressure," Cancer Res., 48pp. 7022-7032.

[69] Kim, S., Lim, Y. T., Soltesz, E. G., 2004, "Near-Infrared Fluorescent Type II Quantum Dots for Sentinel Lymph Node Mapping," Nat.Biotechnol., 22pp. 93-97.

[70] Kim, J. G., 2005, "INVESTIGATION OF BREAST TUMOR HEMODYNAMICS BY NEAR INFRARED SPECTROSCOPY: APPLICATIONS TO CANCER THERAPY MONITORING," .

[71] Pogue, B. W., 1998, "High-Resolution Near-Infrared Tomographic Imaging Simulations of the Rat Cranium by use of a Priori Magnetic Resonance Imaging Structural Information," OPTICS LETTERS, 23(21) pp. 1716-1718.

[72] Wilson, B. C., 1990, "Optical Reflectance and Transmittance of Tissues: Principles and Applications," IEEE JOURNAL OF QUANTUM ELECTRONICS, 26(12) pp. 2186-2199.

[73] Tuchin, V.V., 2003, CRC Press, .

[74] Lim, Y. T., Kim, S., Nakayama, A., 2003, "Selection Ofquantum Dot Wavelengths for Biomedical Assays and Imaging," Molecular Imaging, 2pp. 50-64.

[75] Grand, A. M. D., and Frangioni, J. V., 2003, "An Operational Near-Infrared Fluorescence Imaging System Prototype for Large Animal Surgery," Technology in Cancer Research & Treatment, 2pp. 1-10.

[76] Pogue, B. W., 2006, "Review of Tissue Simulating Phantoms for Optical Spectroscopy, Imaging and Dosimetry," Journal of Biomedical Optics, 11(4) .

[77] Alaniz, A., 2000, "Study of Blended Agar and Gelatin Gel Phantoms for Elastography by Application of Statistical Mechanics and Thermodynamics to Dynamic Stress-Strain, X-Ray and NMR Data," .

[78] Choi, Y. S., 1999, "Study on Gelatin-Containing Artificial Skin: I. Preparation and Characteristics of Novel Gelatin-Alginate Sponge," Biomaterials, 20pp. 409.

[79] Cubeddu, R., 1997, "A Solid Tissue Phantom for Photon Migration Studies," Phys. Med. Biol., 42pp. 1971-1979.

[80] Viator., J. A., 2003, "Spectra from 2.5–15 Mm of Tissue Phantom Materials, Optical Clearing Agents and Ex Vivo Human Skin: Implications for Depth Profiling of Human Skin," Phys. Med. Biol., 48.

[81] Qu, J. Y., 2000, "Excitation-and-Collection Geometry Insensitive Fluorescence Imaging of Tissue-Simulating Turbid Media," APPLIED OPTICS, 39(19) .

[82] Passos, D., 2005, "Tissue Phantom for Optical Diagnostics Based on a Suspension of Microspheres with a Fractal Size Distribution," Journal of Biomedical Optics, 10(6) .

[83] Hebden, J. C., 2006, "A Soft Deformable Tissue-Equivalent Phantom for Diffuse Optical Tomography," Phys. Med. Biol., 51pp. 5581-5590.

[84] Howard, S., 2003, "Characterization and FEA Simulation for a HIFU Phantom Material," IEEE ULTRASONICS, pp. 1270.

[85] Walker, G. W., Sundar, V. C., Rudzinski, C. M., 2003, "Quantum-Dot Optical Temperature Probes," Applied Physics Letters, 83pp. 3555-3557.

[86] Zhang, X. B., Ryou, J. H., Dupuis, R. D., 2005, "Temperature-Dependent Luminescence of InP Quantum Dots Coupled with an InGaP Quantum Well and of InP Quantum Dots in a Qunatum Well," Appl.Phys.Lett., 87pp. 201110.

[87] Wang, S., Westcott, S., and Chen, W., 2002, "Nanoparticle Luminescene Thermometry," J Phys Chem B, 106pp. 11203-11209.

[88] Franceschetti, A., 2000, "Optical Transitions in Charged CdSe Quantum Dots." Phys. Rev. B, 62pp. 16287-16290.

[89] Valerini, D., 2005, "Temperature Dependence of the PL Properties of Colloidal CdSe/ZnS core/shell Quantum Dots Embedded in a Polystyrene Matrix," PHYSICAL REVIEW B, 71.

[90] Hanson, W. L., Wang, M. -., and Han, B., 2006, "Development of Quantum Dot Mediated Thermometry for Intraoperative Monitoring of Minimally Invasive Thermal Surgery," Proceedings of ASME 2006 Summer Bioengineering Conference, BIO2006-157706.

[91] Weissleder, R., 2001, "A Clearer Vision for in Vivo Imaging," Nat.Biotechnol., 19pp. 316-317.

[92] Knight, A., Gaunt, J., Davidson, T., 2004, "Evaluation of the suitability of quantum dots as fluorescence standards," Teddington, Middlesex, UK.

[93] Alivisatos, P., 2004, "The use of Nanocrystals in Biological Detection," Nat.Biotechnol., 22pp. 47-52.

[94] Michalet, X., Pinaud, F. F., Bentolila, L. A., 2005, "Quantum Dots for Live Cells, in Vivo Imaging, and Diagnostics," Science, 307pp. 538-544.

[95] Morgan, N. Y., English, S., Chen, W., 2005, "Real Time in Vivo Non-Invasive Optical Imaging using Near-Infrared Fluorescent Quantum Dots," Acad.Radiol., 12pp. 313-323.

[96] Lee, M. -., and Kim, C. -., 2003, "Formation of HgTe Nanodisks Embedded in PbTe Matrix by Precipitation Phenomena," Nano Letters, 3pp. 1607-1610.

[97] Hirsch, L. R., Stafford, R. J., Bankson, J. A., 2003, "Nanoshell-Mediated Near-Infrared Thermal Therapy of Tumors Under Magnetic Resonance Guidance," PNAS, 100pp. 13549-13554.

[98] Stern, J. M., Stanfield, J. L., Lotan, Y., 2006, "The Efficacy of Laser Activated Gold Nanoshells to Ablate Prostate Cancer Cell in Vitro," Urology (in Review), .

[99] O’Neal, D., 2004, "Photo-Thermal Tumor Ablation in Mice using Near Infrared-Absorbing Nanoparticles," Cancer Letters, 209pp. 171-176.

[100] Hanson, W. L., Michael, N. L., Kim, C. -., 2007, "Development of Quantum Dot Embedded Nanoparticles for Biothermal Imaging," Proceedings of ASME 2007 Summer Bioengineering Conference, SBC2007-176185.

[101] Oldenberg, S., Averitt, R., Westcott, S., 1998, "Nanoengineering of Optical Resonances," Chem Phys Lett, 28pp. 243-247.

[102] Hines, M. A., and Guyot-Sionnest, P., 1996, "Synthesis and Characterization of Strongly Luminescing ZnS-Capped CdSe Nanocrystals," J.Phys.Chem., 100pp. 468-471.

[103] Stern, J. M., Stanfield, J. L., Kabbani, W., 2007, "Selective Prostate Cancer Thermal Ablation with Laser Activated Gold Nanoshells," Journal of Urology (in Press), .

[104] Han, B., 2008, "Spatiotemporal Temperature Measurement using Quantum Dot Thermometry during Gold Nanoshell Mediated Thermal Therapy," ASME Summer Bioengineering Conference, SBC2008-192658.

[105] Mobley, J., 2003, "Optical Properties of Tissue, Ch.2," CRC Press, .

[106] Wang, L.V., 2007, "Biomedical Optics, Principles and Imaging," .

[107] Cong, W., 2005, "Practical Reconstruction Method for Bioluminescence Tomography," Optics Express, 13(18) pp. 6756.

[108] Martelli, F., 2000, "Accuracy of the Diffusion Equation to Describe Photon Migration through an Infinite Medium: Numerical and Experimental Investigation," Phys.Med. Biol., 45pp. 1359-1373.

[109] Martı-Lopez, L., 2003, "Validity Conditions for the Radiative Transfer Equation," J. Opt. Soc. Am. A., 20(11) pp. 2046-2056.

[110] Ozisik, M.N., 2000, "Inverse Heat Transfer," .

[111] Siegel, R., 2001, "Thermal Radiation Heat Transfer," .

[112] Schweiger, M., 1995, "The Finite Element Method for the Propagation of Light in Scattering Media: Boundary and Source Conditions," Medial Physics, 22(11) pp. 1779.

[113] Pepper, D. W., 1992, "The Finite Element Method: Basic Concepts and Applications," .

[114] Abdollahzadeh, N., 2008, "NON INVASIVE TEMPERATURE MEASUREMENT USING QUANTUM DOT FLURESCENCE FOR BIOMEDICAL APPLICATION," .

[115] Qiu, X., 2008, "NANOSTRUCTURED MATERIALS FOR ENERGY CONVERSION," .

[116] Shen, Q., 2000, "Photoluminescence and Photoacoustic Investigations of the Photodarkening Effect in CdSxSe1-x Nanocrystal-Doped Glasses," Journal of Luminescence, 87pp. 444-446.

[117] Ntziachristos, V., Bremer, C., and Weissleder, R., 2003, "Fluorescence Imaging with Near-Infrared Light: New Technological Advances that Enable in Vivo Molecular Imaging," Eur.Radiol., 13pp. 195-203.

[118] Fu, A., 2005, "Semiconductor Nanocrystals for Biological Imaging," Current Opinion in Neurobiology, 15pp. 568-575.

[119] Nour, S., 2005, "Radiofrequency Thermal Ablation: The Role of MR Imaging in Guiding and Monitoring Tumor Therapy," Magn Reson Imaging Clin N Am, 13(3) pp. 561-581.

[120] Kaczkowski, P. J., 2004, "Temperature Rise Measured Noninvasively during Thermal Therapy using Backscattered Ultrasound," IEEE Ultrasonics Symposium, pp. 720.

[121] Kim, J. G., 2009, "Post Doctoral Researcher, Beckman Laser Institute and Medical Clinic, University of California Irvine," .

[122] Tromberg, B. J., 1997, "Non-Invasive Measurements of Breast Tissue Optical Properties using Frequency-Domain Photon Migration," Phil. Trans. R. Soc. Lond. B, 352pp. 661-668.

[123] Rinzema, K., 1998, "Direct Experimental Verification of Light Transport Theory in an Optical Phantom," J.Opt.Soc.Am.A, 15pp. 2078-2088.

BIOGRAPHICAL INFORMATION

Willard Hanson was born in Moorhead, MN, on January 29, 1954, the son of William and Birdie Hanson. He graduated from Detroit Lakes High School, Detroit Lakes, MN in 1972. He then spent four years in the US Navy as an Aviation Electronics Technician. He received an Associates Degree in Engineering Science at Greenfield Community College, Greenfield Massachusetts in 1987 and a Bachelor of Science Degree in Mechanical Engineering from the University of Massachusetts, Amherst Massachusetts in 1990. He worked as a contract engineer in machine design and manufacturing until 2000. He earned a Master of Science Degree in Mechanical Engineering at the University of Minnesota, Minneapolis Minnesota in 2005.